CWP-675
August 2010

Wave-mode separation for elastic imaging in transversely isotropic media

Jia Yan

— Doctoral Thesis —
Geophysics

Defended on August 25, 2010

Committee Chair:	Prof. Luis Tenorio
Advisor:	Prof. Paul Sava
Co-advisor:	Prof. Ilya Tsvankin
Committee members:	Prof. Tom Davis
	Prof. Stephen Hill
	Prof. Eileen Poeter
	Dr. Joseph Dellinger

Center for Wave Phenomena
Colorado School of Mines
Golden, Colorado 80401
(1) 303 273-3557

Abstract

Multicomponent data are increasingly acquired on land and at the ocean bottom in an attempt to better understand the subsurface structure and characterize oil and gas reservoirs.

Seismic imaging in areas with complex geology requires accurate reconstruction of seismic wavefields. Since in reality, seismic waves propagate through the earth as a superposition of compressional and shear waves, an elastic wave equation is usually more appropriate and more accurate for wavefield reconstruction compared to an acoustic wave equation. Conventional acoustic migration techniques image a scalar wavefield representing P-waves; in contrast, elastic migration techniques image a vector wavefield including both the P- and S-waves. A crucial component of wave-equation migration is the imaging condition which extracts information about the discontinuities of physical properties from the reconstructed wavefields at every location in space. For elastic imaging, it is desirable to decompose the reconstructed vector fields into pure wave modes, such that the imaging condition produces interpretable images which characterize reflectivity of different reflection types. This requires a wave mode separation before application of an imaging condition.

In a homogeneous VTI (transversely isotropic with a vertical symmetry axis) medium, wave-mode separation can be achieved in the wavenumber domain by projecting the reconstructed vector fields onto the polarization vectors of various wave modes. The polarization vectors of P- and SV-waves in the wavenumber domain are determined by the medium parameters, i.e. Thomsen parameters ϵ and δ and the V_{P0}/V_{S0} ratio. For a heterogeneous medium, the polarization vectors at all grids of the model are transformed to the space domain to become spatially varying filters. Then the wave modes are separated by non-stationary filtering of the vector wavefields with the space-domain operators.

For a 3D TTI (transversely isotropic with a tilted symmetry axis) medium, the polarization vectors depend on the tilt and azimuth of the symmetry axis, as well as the parameters, V_{P0}, V_{S0}, ϵ, and δ. Using these parameters, one can separate the wave-modes by constructing nine filters corresponding to the nine Cartesian components of the three modes at every grid point. Since the polarization vectors of two shear modes in the symmetry axis direction of a TI medium are not defined by the medium parameters, I construct their vectors by exploiting the polarization orthogonality of the three modes. This procedure allows one to separate two shear modes from each other kinematically.

Wave-mode separation by spatial filtering is computationally intensive and is usually not affordable for 3D models. A wavenumber-domain projection is much cheaper than the space-domain filtering, but it is only effective for a homogeneous model. A more efficient separation technique, which combines the benefit of both methods, is a mixed-domain separation. A mixed-domain separation is applicable for heterogeneous anisotropic models. The method first separates the wave modes at several homogeneous reference models in the wavenumber domain. Then these modes are interpolated in the space domain using the spatially variable medium parameters. This mixed-domain separation offers the same high computational efficiency as the wavenumber-domain separation and approximately the same accuracy as the space-domain separation.

The wave-mode separation for TI media developed in this thesis can be applied to reverse time migration (RTM) and subsequent angle decomposition for anisotropic media with complex subsurface structure.

Table of Contents

Acknowledgments

Pursuing a Ph.D. degree is undoubtedly an endeavor, which is by no means an easy task even for the smartest people in the world. Seven years ago, I left my home country and started my graduate studies. Thanks to my family's encouragement, I began my PhD study at the Colorado School of Mines. At that time, I did not consider seriously whether doing a PhD was a correct thing for me. And now, as my PhD study is drawing to an end, I would say that the five years of study has taught me so much and I have grown with the accompaniment of happiness and tears, excitement and frustrations. I guess the graduate study will forever remain the most special period in my life.

A PhD degree is not the end of learning, but the beginning of a new journey, which requires many technical and life skills. I believe that the years of PhD study should teach us these skills. Here, I would like to thank many people who have helped to acquire those skills. My advisors Paul Sava and Ilya Tsvankin are the first ones that I want to express my gratitude to. They have helped me countless of times when I have encountered technical difficulties. Dr. Tsvankin got me interested in anisotropy and I appreciate his deep thinking and great knowledge in the field of anisotropy. Dr. Sava introduced me to wavefield-based imaging that is certainly the hottest topic in exploration geophysics. Thanks to Dr. Sava for spending a lot of time with me every week to discuss my projects. I also thank other CWP professors Roel Snieder and Dave Hale. Dr. Snieder's insight into science and his enthusiasm for education have always touched me. Dr. Hale's sharpness in the computational aspect of geophysics also made me aware of the importance of geophysical computation.

I had a good time with my fellow students. The senior students Jyoti Behura, Xiaoxia Xu, Yaping Zhu, Rodrigo Fuck, Kurang Metha, Carlos Pecheco, and Ivan Vasconcelos have all offered me valuable advice which made my PhD time much easier. I thank the members

of A-team (Xiaoxiang Wang, Steve Smith, Bharath Shekar, Mamorou Takanashi, Jyoti Behura, Xiaoxia Xu, Yaping Zhu, and Rodrigo Fuck) and the members of I-team (Yong Ma, Ran Xuan, Toning Yang, Francesco Perrone, Jeff Godwin, and Tom Culison) for intriguing discussions. I enjoy chatting with other students as well: Flippo Broggini, Simon Luo, Chris Engelsma, Farnoush Forghani-Arani, Gabi Melo, Clement Fleury, Myoung Jae Kwon, Yuanzhong Fan... The Chinese dinner every Friday evening with Luming Liang and Hui Liu, Xiaoxiang Wang, Yongxia Liu, Yong Ma, Tongning Yang is always the happiest time in the week. I enjoyed mingling with diverse culture: Cindy Arjoon, Laxmidhar Behera, Masatoshi Miyazawa all became good friends and we could chat about something outside geophysics.

Special thanks go to my mentors Ray Abma and Joe Dellinger in BP, who made my internship smoother and guided me through the project. Their scientific insights and kindness have shown me what great mentors are like. I also thank Rongrong Lu, John Anderson, Peter Traynin, and Xiaojun Huang in ExxonMobil who helped me a lot in my ExxonMobil internship.

The staff at CWP are all great people. Pam and Michelle helped in all occasions of administration; John Stockwell helped in fixing my Linux computer all the time; Barbara is a great publication specialist and also a great yoga buddy; Diane Witters is of tremendous help for showing me how to improve my writing so that I can be more confident when I give the manuscript to my advisor.

Finally, I want to thank my family members who support me unconditionally. I cannot say enough how much I thank my boyfriend Liangzhe, without whom, I could not have persevered with this PhD study. Not only does he provide emotional encouragement but also technical and scientific suggestions, which have all helped me get through difficult times.

Chapter 1

Introduction

Multicomponent data are often acquired because multicomponent waves have been recognized to have a number of advantages. Converted waves can produce better images of the Earth structure where P-waves have small reflectivity and S-waves have larger reflectivity. Converted waves also complement P-waves in imaging through zones where P-waves are highly attenuated and S-waves are less affected, e.g., in gas-concentrated areas. Converted waves also provide valuable information for lithology discrimination, anisotropic parameter estimation, and reservoir characterization.

Imaging with multicomponent data is usually carried out by separating P- and S-wave data and using them for acoustic-like imaging. The separation of P- and S-wave data is usually achieved under the assumption that the near surface S-wave velocity is small and that S-waves propagate in near-vertical directions around the receivers. In areas with complicated near-surface structures, this assumption is violated, and P- and S-wave data separation is difficult. On the other hand, one can use the recorded multicomponent data to reconstruct vector wavefields using elastic wave equation. If vector wavefields are reconstructed, one has two options for imaging condition: imaging with Cartesian components or with pure modes. The former images with mixed wave modes, and images obtained this way lack clear physical meaning and are not suitable for interpretation. To obtain images with clear physical meaning, I propose to image with vector potentials instead of vector displacements, velocities, or accelerations. This proposed imaging condition yields images that resemble acoustic-type imaging in physical meaning, i.e., the images represent reflection coefficients of different reflection types.

To obtain the vector potential equivalents in anisotropic media, one needs to separate P and S modes. This thesis develops mode separation for heterogeneous models and extends the work to symmetry planes of TI media. The thesis also generalizes the algorithm to TTI media in 3D and enables separation of P, SV, and SH modes to obtain three scalar wavefields. The general idea of mode separation is to project the vector wavefields onto the polarization direction of each mode. The polarization vectors are obtained by solving the Christoffel equation using local medium parameters. These vectors in the space domain correspond to localized filters, and each mode can be separated from the others by non-stationary filtering of the vector wavefields with the spatially varying operators. To separate wave modes more efficiently in 3D, I develop a mixed-domain algorithm for mode separation, which makes the processing feasible for 3D models with complex geology.

Chapters 2-5 of this thesis have been written as individual papers. In particular, Chapters 2 and 3 have already been published (Yan & Sava, 2008, 2009). Chapters 4 and 5 have been submitted for publication.

In Chapter 2, I propose a method for reverse time migration with angle-domain imaging formulated for multicomponent data from isotropic media. The method is based on the separation of the reconstructed elastic wavefields into pure wave modes using conventional Helmholtz decomposition for isotropic media. Elastic wavefields from the source and receivers are separated into pure compressional and transverse wave-modes which are then used for angle-domain imaging. The images formed using this procedure are interpretable in terms of the subsurface physical properties, for example, by analyzing the PP or PS angle-dependent reflectivity.

In Chapter 3, I present a method for obtaining spatially-varying "pseudo-derivative" operators with application to wave-mode separation in symmetry planes of VTI media. The main idea is to utilize polarization vectors constructed in the wavenumber domain using local medium parameters and then transform these vectors back to the space domain. The main advantage of applying the pseudo-derivative operators in the space domain constructed

in this way is that they are suitable for heterogeneous media. The wave-mode separators obtained using this method represent spatially-variable filters and can be used to separate wave modes in VTI media with arbitrary strength of anisotropy. This methodology is applicable for elastic RTM in heterogeneous VTI media.

In Chapter 4, I show a method for obtaining spatially-varying wave-mode separators, which can be used to separate elastic wave-modes in TTI models. In order for the operators to work in TI models with a tilted symmetry axis, I incorporate one more parameter — the local tilt angle — in addition to the parameters needed for the VTI operators. As in VTI media, the spatial filters can be used to separate complicated wavefields in models with substantial heterogeneity and strong anisotropy. This chapter also extends the wave-mode separation to 3D TI models. The P-mode separators can be constructed by solving the Christoffel equation for the P-wave eigenvectors with local medium parameters. The SV and SH separators are constructed using the mutual orthogonality among P, SV, and SH modes for a fixed plane-wave phase vector. For the three modes, there are nine filters, with three filters for each mode. The separators vary according to the medium parameters V_{P0}, V_{S0}, ϵ, δ, and tilt ν and azimuth α of the symmetry axis. In anisotropic media, P-waves usually polarize linearly in most directions, and S-waves polarize non-linearly in singular directions and velocity extrema directions. Therefore, the separation based on projecting wavefields onto the linear-polarization directions of each mode preserves P-wave amplitudes better than S-wave amplitudes. Spatially-varying 3D separators have potential benefits for complex models and can be used to separate wave-modes in elastic RTM for TTI models.

In Chapter 5, I suggest an efficient method for elastic wave mode separation applicable for complex media. Wave mode separation can be carried out in a mixed wavenumber and space domain. First, I separate wave modes in the wavenumber domain for a number of reference models. This is followed by interpolation in the space domain. The mixed-domain separation has the advantage of being much more computationally efficient than the more accurate space-domain separation. The mixed-domain separation is especially beneficial

for 3D heterogeneous models where the space-domain separation becomes prohibitively expensive. The efficient method is effective for mode separation in media with spatially varying ϵ, δ, tilt angle ν and azimuth angle α.

Finally, I draw general conclusions and suggest future work directions in Chapter 6.

Chapter 2

Isotropic angle-domain elastic reverse time migration

2.1 Summary

Multicomponent data are not usually processed with specifically designed procedures, but with procedures analogous to the ones used for single-component data. In isotropic media, the vertical and horizontal components of the data are commonly taken as proxies for the P- and S-wave modes which are imaged independently with acoustic wave equations. This procedure works only if the vertical and horizontal component accurately represent P- and S-wave modes, which is not true in general. Therefore, multicomponent images constructed with this procedure exhibit artifacts caused by the incorrect wave mode separation at the surface.

An alternative procedure for elastic imaging uses the full vector fields for wavefield reconstruction and imaging. The wavefields are reconstructed using the multicomponent data as a boundary condition for a numerical solution to the elastic wave equation. The key component for wavefield migration is the imaging condition that evaluates the match between wavefields reconstructed from sources and receivers. For vector wavefields, a simple component-by-component crosscorrelation between two wavefields leads to artifacts caused by crosstalk between the unseparated wave modes. An alternative method is to separate elastic wavefields after reconstruction in the subsurface and implement the imaging condition as crosscorrelation of pure wave modes instead of the Cartesian components of the displacement wavefield. This approach leads to images that are easier to interpret, since they describe reflectivity of specified wave modes at interfaces of physical properties.

As for imaging with acoustic wavefields, the elastic imaging condition can be formulated conventionally (crosscorrelation with zero lag in space and time), as well as extended to non-zero space and time lags. The elastic images produced by an extended imaging condition can be used for angle decomposition of primary (PP or SS) and converted (PS or SP) reflectivity. Angle gathers constructed with this procedure have applications for migration velocity analysis and amplitude versus angle analysis.

2.2 Introduction

Seismic processing is usually based on acoustic wave equations, which assume that the Earth represents a liquid that propagates only compressional waves. Although useful in practice, this assumption is not theoretically valid. Earth materials allow for both compressional and shear wave propagation in the subsurface. Shear waves, either generated at the source or converted from compressional waves at various interfaces in the subsurface, are detected by multicomponent receivers. Shear waves are usually stronger at large incidence and reflection angles, often corresponding to large offsets. However, for complex geological structures near the surface, shear waves can be quite significant even at small offsets. Conventional single-component imaging ignores shear wave modes, which often leads to incorrect characterization of wave propagation, incomplete illumination of the subsurface and poor amplitude characterization.

Even when multicomponent data are used for imaging, they are usually not processed with specifically designed procedures. Instead, those data are processed with ad-hoc procedures borrowed from acoustic wave equation imaging algorithms. For isotropic media, a typical assumption is that the recorded vertical and in plane horizontal components are good approximations for the P- and S-wave modes, respectively, which can be imaged independently. This assumption is not always correct, leading to errors and noise in the images, since P- and S-wave modes are normally mixed on all recorded components. Also, since P and S modes are mixed on all components, true-amplitude imaging is questionable no

matter how accurate the wavefield reconstruction and imaging condition are.

Multicomponent imaging has long been an active research area for exploration geophysicists. Techniques proposed in the literature perform imaging by using time extrapolation, e.g. by Kirchhoff migration (Kuo & Dai, 1984; Hokstad, 2000) and reverse time migration (Whitmore, 1995; Chang & McMechan, 1986, 1994) adapted for multicomponent data. The reason for working in the time domain, as opposed to the depth domain, is that the coupling of displacements in different directions in elastic wave equations makes it difficult to derive a dispersion relation that can be used to extrapolate wavefields in depth (Clayton & Brown, 1979; Clayton, 1981).

Early attempts at multicomponent imaging used the Kirchhoff framework and involve wave-mode separation on the surface prior to wave-equation imaging (Wapenaar *et al.*, 1987; Wapenaar & Haimé, 1990). Kuo & Dai (1984) perform shot-profile elastic Kirchhoff migration, and Hokstad (2000) performs survey-sinking elastic Kirchhoff migration. Although these techniques represent different migration procedures, they compute traveltimes for both PP and PS reflections and sum data along these travel time trajectories. This approach is equivalent to distinguishing between PP and PS reflections and applying acoustic Kirchhoff migration for each mode separately. When geology is complex, the elastic Kirchhoff migration technique suffers from drawbacks similar to those of acoustic Kirchhoff migration because ray theory breaks down (Gray *et al.*, 2001).

There are two main difficulties with independently imaging P and S wave modes separated on the surface. The first is that conventional elastic migration techniques either consider vertical and horizontal components of recorded data as P and S modes, which is not always accurate, or separate these wave modes on the recording surface using approximations, e.g. polarization (Pestana *et al.*, 1989) or elastic potentials (Etgen, 1988; Zhe & Greenhalgh, 1997) or wavefield extrapolation in the vicinity of the acquisition surface (Wapenaar *et al.*, 1990; Admundsen & Reitan, 1995). Other elastic reverse time migration techniques do not separate wave modes on the surface and reconstruct vector fields, but

use imaging conditions based on ray tracing (Chang & McMechan, 1986, 1994) that are not always robust in complex geology. The second difficulty is that images produced independently from P and S modes are hard to interpret together, since often they do not line-up consistently, thus requiring image post processing, e.g. by manual or automatic registration of the images (Gaiser, 1996; Fomel & Backus, 2003; Nickel & Sonneland, 2004).

I advocate an alternative procedure for imaging elastic wavefield data. Instead of separating wavefields into scalar wave modes on the acquisition surface followed by scalar imaging of each mode independently, I use the entire vector wavefields for wavefield reconstruction and imaging. The vector wavefields are reconstructed using the multicomponent vector data as boundary conditions for a numerical solution to the elastic wave equation. The key component of such a migration procedure is the imaging condition which evaluates the match between wavefields reconstructed from the source and receiver. For vector wavefields, a simple component-by-component crosscorrelation between the two wavefields leads to artifacts caused by crosstalk between the unseparated wave modes, i.e. all P and S modes from the source wavefield correlate with all P and S modes from the receiver wavefield. This problem can be alleviated by using separated elastic wavefields, with the imaging condition implemented as crosscorrelation of wave modes instead of crosscorrelation of the Cartesian components of the wavefield. This approach leads to images that are cleaner and easier to interpret since they represent reflections of single wave modes at interfaces of physical properties.

As for imaging with acoustic wavefields, the elastic imaging condition can be formulated conventionally (crosscorrelation with zero lag in space and time), as well as extended to non-zero space lags. The elastic images produced by extended imaging condition can be used for angle decomposition of PP and PS reflectivity. Angle gathers have many applications, including migration velocity analysis (MVA) and amplitude versus angle (AVA) analysis.

The advantage of imaging with multicomponent seismic data is that the physics of

wave propagation is better represented, and resulting seismic images more accurately characterize the subsurface. Multicomponent images have many applications. For example they can be used to provide reflection images where the P-wave reflectivity is small, image through gas clouds where the P-wave signal is attenuated, validate bright spot reflections and provide parameter estimation for this media, Poisson's ratio estimates, and detect fractures through shear-wave splitting for anisotropic media (Li, 1998; Zhu *et al.*, 1999; Knapp *et al.*, 2001; Gaiser *et al.*, 2001; Stewart *et al.*, 2003a; Simmons & Backus, 2003). Assuming no attenuation in the subsurface, converted wave images also have higher resolution than pure-mode images in the shallow part of sections because S-waves have shorter wavelengths than P-waves. Modeling and migrating multicomponent data with elastic migration algorithms enables one to make full use of information provided by elastic data and correctly position geologic structures.

This chapter presents a method for angle-domain imaging of elastic wavefield data using reverse time migration (RTM). In order to limit the scope of this chapter, I ignore several practical issues related to data acquisition and pre-processing for wave-equation migration. For example, my methodology ignores the presence of surface waves, e.g. Rayleigh and Love waves, the relatively poor spatial sampling when imaging with multicomponent elastic data, e.g. for OBC acquisition, the presence of anisotropy in the subsurface and all amplitude considerations related to the directionality of the seismic source. All these issues are important for elastic imaging and need to be part of a practical data processing application. I restrict in this chapter my attention to the problem of wave-mode separation after wavefield extrapolation and angle-decomposition after the imaging condition. These issues are addressed in more detail in a later section of the chapter.

I begin by summarizing wavefield imaging methodology, focusing on reverse time migration for wavefield multicomponent migration. Then, I describe different options for wavefield multicomponent imaging conditions, e.g. based on vector displacements and vector potentials. Finally, I describe the application of extended imaging conditions to multi-

component data and corresponding angle decomposition. I illustrate the wavefield imaging techniques using data simulated from the Marmousi II model (Martin *et al.*, 2002).

2.3 Wavefield imaging

Seismic imaging is based on numerical solutions to wave equations, which can be classified into ray-based (integral) solutions and wavefield-based (differential) solutions. Kirchhoff migration is a typical ray-based imaging procedure which is computationally efficient but often fails in areas of complex geology, such as sub-salt, because the wavefield is severely distorted by lateral velocity variations leading to complex multipathing. Wavefield imaging works better for complex geology, but is more expensive than Kirchhoff migration. Depending on computational time constraints and available resources, one can apply different levels of approximation to accelerate imaging, i.e. one-way vs. two-way, acoustic vs. elastic, isotropic vs. anisotropic, etc.

Despite the complexity of various types of wavefield migration algorithms, any wavefield imaging method can be separated into two parts: wavefield reconstruction followed by the application of an imaging condition. For prestack depth migration, source and receiver wavefields have to be reconstructed at all locations in the subsurface. The wavefield reconstruction can be carried out using extrapolation in either depth or time, and with different modeling approaches, such as finite-differences (Dablain, 1986; Alford *et al.*, 1974), finite-elements (Bolt & Smith, 1976), or spectral methods (Seriani & Priolo, 1991; Seriani *et al.*, 1992; Dai & Cheadle, 1996). After reconstructing wavefields with the recorded data as boundary conditions into the subsurface, an imaging condition must be applied at all locations in the subsurface in order to obtain a seismic image. The simplest types of imaging conditions are based on crosscorrelation or deconvolution of the reconstructed wavefields (Claerbout, 1971). These imaging conditions can be implemented in the time or frequency domain depending on the domain in which wavefields have been reconstructed. Here, I concentrate on reverse time migration with wavefield reconstruction and imaging condition

implemented in the time domain.

2.3.1 Reverse time migration

Reverse time migration reconstructs the source wavefield forward in time and the receiver wavefield backward in time. It then applies an imaging condition to extract reflectivity information out of the reconstructed wavefields. The advantages of reverse time migration over other depth migration techniques are that the extrapolation in time does not involve evanescent energy, and no dip limitations exist for the imaged structures (McMechan, 1982, 1983; Whitmore, 1983; Baysal *et al.*, 1983). Although conceptually simple, reverse time migration has not been used extensively in practice due to its high computational cost. However, the algorithm is becoming more and more attractive to the industry because of its robustness in imaging complex geology, e.g. sub-salt (Jones *et al.*, 2007; boe, n.d.).

McMechan (1982, 1983), Whitmore (1983), and Baysal *et al.* (1983) first used reverse time migration for poststack or zero-offset data. The procedure underlying poststack reverse time migration is the following: first, reverse the recorded data in time; second, use these reversed data as sources along the recording surface to propagate the wavefields in the subsurface; third, extract the image at zero time, e.g. apply an imaging condition. The principle of poststack reverse time migration is that the subsurface reflectors work as exploding reflectors and that the wave equation used to propagate data can be applied either forward or backward in time by simply reversing the time axis (Levin, 1984).

Chang & McMechan (1986) apply reverse time migration to prestack data. Prestack reverse time migration reconstructs both source and receiver wavefields. The source wavefield is reconstructed forward in time, and the receiver wavefield is reconstructed backward in time. Chang & McMechan (1986, 1994) use a so-called excitation-time imaging condition, where images are formed by extracting the receiver wavefield at the time taken by a wave to travel from the source to the image point. This imaging condition is a special case of the crosscorrelation imaging condition of Claerbout (1971).

2.3.2 Elastic imaging vs. acoustic imaging

Multicomponent elastic data are often recorded in land or marine (ocean-bottom) seismic experiments. However, as mentioned earlier, elastic vector wavefields are not usually processed by specifically designed imaging procedures, but rather by extensions of techniques used for scalar wavefields. Thus, seismic data processing does not take full advantage of the information contained by elastic wavefields. In other words, it does not fully unravel reflections from complex geology or correctly preserve imaging amplitudes and estimate model parameters, etc.

Elastic wave propagation in an infinite homogeneous isotropic medium is characterized by the wave equation (Aki & Richards, 2002)

$$\rho\frac{\partial^2\mathbf{u}}{\partial t^2} = \mathbf{f} + (\lambda+2\mu)\,\nabla\,(\nabla\cdot\mathbf{u}) - \mu\nabla\times\nabla\times\mathbf{u}\,, \tag{2.1}$$

where $\mathbf{u}$ is the vector displacement wavefield, t is time, ρ is the density, $\mathbf{f}$ is the body source force, and λ and μ are the Lamé moduli. This wave equation assumes a slowly varying stiffness tensor over the imaging space. For isotropic media, one can process the elastic data either by separating wave-modes and migrating each mode using methods based on acoustic wave theory, or by migrating the whole elastic data set based on the elastic wave equation 2.1. The elastic wavefield extrapolation using equation 2.1 is usually performed in time by Kirchhoff migration or reverse time migration.

Acoustic Kirchhoff migration is based on diffraction summation, which accumulates the data along diffraction curves in the data space and maps them onto the image space. For multicomponent elastic data, Kuo & Dai (1984) discuss Kirchhoff migration for shot-record data. Here, identified PP and PS reflections can be migrated by computing source and receiver traveltimes using P-wave velocity for the source rays, and P- and S-wave velocities for the receiver rays. Hokstad (2000) performs multicomponent anisotropic Kirchhoff migration for multi-shot, multi-receiver experiments, where pure-mode and converted-mode images are obtained by visco-elastic vector wavefields and application of a survey-sinking

imaging condition to the reconstructed vector wavefields. The wavefield separation is effectively done by the Kirchhoff integral which handles both P- and S-waves, although this technique fails in areas of complex geology where ray theory breaks down.

Elastic reverse time migration has the same two components as acoustic reverse time migration: reconstruction of source and receiver wavefield and application of an imaging condition. The source and receiver wavefields are reconstructed by forward and backward propagation in time with various modeling approaches. For acoustic reverse time migration, wavefield reconstruction is done with the acoustic wave equation using the recorded scalar data as a boundary condition. In contrast, for elastic reverse time migration, wavefield reconstruction is done with the elastic wave equation using the recorded vector data as boundary conditions.

Since pure-mode and converted-mode reflections are mixed on all components of recorded data, images produced with reconstructed elastic wavefields are characterized by crosstalk due to the interference of various wave modes. In order to obtain images with clear physical meaning, most imaging conditions separate wave modes. There are two potential approaches to separate wavefields and image elastic seismic wavefields. The first option is to separate P and S modes on the acquisition surface from the recorded elastic wavefields. This procedure involves either approximations for the propagation path and polarization direction of the recorded data, or reconstruction of the seismic wavefields in the vicinity of the acquisition surface by a numerical solution of the elastic wave equation, followed by wavefield separation of scalar and vector potentials using Helmholtz decomposition (Etgen, 1988; Zhe & Greenhalgh, 1997). An alternative data decomposition using P and S potentials reconstructs wavefields in the subsurface using the elastic wave equation, then decomposes the wavefields into P- and S-wave modes. This is followed by forward extrapolation of the separated wavefields back to the surface using the acoustic wave equation with the appropriate propagation velocity for the various wave modes (Sun *et al.*, 2006) by conventional procedures used for scalar wavefields.

The second option is to extrapolate wavefields in the subsurface using a numerical solution to the elastic wave equation and then apply an imaging condition that extracts reflectivity information from the source and receiver wavefields. In the case where extrapolation is implemented by finite-difference methods (Chang & McMechan, 1986, 1994), this procedure is known as elastic reverse time migration, and is conceptually similar to acoustic reverse time migration (Baysal *et al.*, 1983), which is more frequently used in seismic imaging.

Many imaging conditions can be used for reverse time migration. Elastic imaging conditions are more complex than acoustic imaging conditions because both source and receiver wavefields are vector fields. Different elastic imaging conditions have been proposed for extracting reflectivity information from reconstructed elastic wavefields. Hokstad *et al.* (1998) use elastic reverse time migration with Lamé potential methods. Chang & McMechan (1986) use the excitation-time imaging condition which extracts reflectivity information from extrapolated wavefields at traveltimes from the source to image positions computed by ray tracing, etc. Ultimately, these imaging conditions represent special cases of a more general type of imaging condition that involves time crosscorrelation or deconvolution of source and receiver wavefields at every location in the subsurface.

2.4 Conventional elastic imaging conditions

For vector elastic wavefields, the crosscorrelation imaging condition needs to be implemented on all components of the displacement field. The problem with this type of imaging condition is that the source and receiver wavefields contain a mix of P- and S-wave modes which crosscorrelate independently, thus hampering interpretation of migrated images. An alternative to this type of imaging performs wavefield separation of scalar and vector potentials after wavefield reconstruction in the imaging volume, but prior to the imaging condition and then crosscorrelate pure modes from the source and receiver wavefields, as suggested by Dellinger & Etgen (1990) and illustrated by Cunha Filho (1992).

2.4.1 Imaging with scalar wavefields

As mentioned earlier, under the assumption of single scattering in the Earth (Born approximation), a conventional imaging procedure consists of two components: wavefield extrapolation and imaging. Wavefield extrapolation is used to reconstruct the seismic wavefield in the imaging volume using the recorded data on the acquisition surface as a boundary condition, and imaging is used to extract reflectivity information from the extrapolated source and receiver wavefields.

Assuming scalar recorded data, wavefield extrapolation using a scalar wave equation reconstructs scalar source and receiver wavefields, $u_s(\mathbf{x},t)$ and $u_r(\mathbf{x},t)$, at every location $\mathbf{x}$ in the subsurface. Using the extrapolated scalar wavefields, one can implement a conventional imaging condition (Claerbout, 1985) as crosscorrelation at zero-lag time:

$$I(\mathbf{x}) = \int u_s(\mathbf{x},t)\, u_r(\mathbf{x},t)\, dt\,. \tag{2.2}$$

Here, $I(\mathbf{x})$ denotes a scalar image obtained from scalar wavefields $u_s(\mathbf{x},t)$ and $u_r(\mathbf{x},t)$, $\mathbf{x}=\{x,y,z\}$ represent Cartesian space coordinates, and t represents time.

2.4.2 Imaging with vector displacements

Assuming vector recorded data, wavefield extrapolation using a vector wave equation reconstructs source and receiver wavefields, $\mathbf{u}_s(\mathbf{x},t)$ and $\mathbf{u}_r(\mathbf{x},t)$, at every location $\mathbf{x}$ in the subsurface. Here, $\mathbf{u}_s$ and $\mathbf{u}_r$ represent displacement fields reconstructed from source wavelet and from data recorded by multicomponent geophones at the surface boundary, respectively. Using the vector extrapolated wavefields $\mathbf{u}_s=\{u_{sx},u_{sy},u_{sz}\}$ and $\mathbf{u}_r=\{u_{rx},u_{ry},u_{rz}\}$, an imaging condition can be formulated as a straightforward extension of equation 2.2 by crosscorrelating all combinations of components of the source and receiver wavefields. Such an imaging condition for vector displacements can be formulated mathematically as

$$I_{ij}(\mathbf{x}) = \int u_{si}(\mathbf{x},t)\, u_{rj}(\mathbf{x},t)\, dt\,, \tag{2.3}$$

where the quantities u_i and u_j stand for the Cartesian components x, y, z of the vector source and receiver wavefields $\mathbf{u}(\mathbf{x}, t)$. For example, $I_{zz}(\mathbf{x})$ represents the image component produced by crosscorrelating of the z components of the source and receiver wavefields, and $I_{zx}(\mathbf{x})$ represents the image component produced by crosscorrelating of the z component of the source wavefield with the x component of the receiver wavefield, etc. In general, an image produced with this procedure has nine components at every location in space.

The main drawback of applying this type of imaging condition is that the wavefield used for imaging contains a combination of P- and S-wave modes. Those wavefield vectors interfere with one another in the imaging condition, since the P and S components are not separated in the extrapolated wavefields. The crosstalk between various components of the wavefield creates artifacts and makes it difficult to interpret the images in terms of pure wave modes, e.g. PP or PS reflections. This situation is similar to the case of imaging with acoustic data contaminated by multiples or other types of coherent noise which are mapped in the subsurface using an incorrect velocity.

2.4.3 Imaging with scalar and vector potentials

An alternative to the elastic imaging condition from equation 2.3 is to separate the extrapolated wavefield into P and S potentials after extrapolation and image using crosscorrelations of the vector and scalar potentials (Dellinger & Etgen, 1990). Separation of scalar and vector potentials can be achieved by Helmholtz decomposition, which is applicable to any vector field $\mathbf{u}(\mathbf{x}, t)$:

$$\mathbf{u} = \nabla\Phi + \nabla \times \mathbf{\Psi}\,, \tag{2.4}$$

where $\Phi(\mathbf{x}, t)$ represents the scalar potential of the wavefield $\mathbf{u}(\mathbf{x}, t)$ and $\mathbf{\Psi}(\mathbf{x}, t)$ represents the vector potential of the wavefield $\mathbf{u}(\mathbf{x}, t)$, and $\nabla \cdot \mathbf{\Psi} = 0$. For isotropic elastic wavefields, equation 2.4 is not used directly in practice, but the scalar and vector components are obtained indirectly by the application of the divergence $(\nabla \cdot)$ and curl $(\nabla \times)$ operators to

the extrapolated elastic wavefield $\mathbf{u}(\mathbf{x},t)$:

$$P = \nabla\cdot\mathbf{u} = \nabla^2\Phi\,, \tag{2.5}$$

$$\mathbf{S} = \nabla\times\mathbf{u} = -\nabla^2\Psi\,. \tag{2.6}$$

For isotropic elastic fields far from the source, quantities P and $\mathbf{S}$ describe compressional and transverse components of the wavefield, respectively (Aki & Richards, 2002). In 2D, the quantity $\mathbf{S}$ corresponds to SV waves that are polarized in the propagation plane.

Using the separated scalar and vector components, I can formulate an imaging condition that combines various incident and reflected wave modes. The imaging condition for vector potentials can be formulated mathematically as

$$I_{ij}(\mathbf{x}) = \int \alpha_{si}(\mathbf{x},t)\,\alpha_{rj}(\mathbf{x},t)\,dt\,, \tag{2.7}$$

where the quantities α_i and α_j stand for the various wave modes $\alpha = \{P,S\}$ of the vector source and receiver wavefields $\mathbf{u}(\mathbf{x},t)$. For example, $I_{PP}(\mathbf{x})$ represents the image component produced by crosscorrelating of the P wave mode of the source and receiver wavefields, and $I_{PS}(\mathbf{x})$ represents the image component produced by crosscorrelating of the P wave mode of the source wavefield with the S wave-mode of the receiver wavefield, etc. In isotropic media, an image produced with this procedure has four independent components at every location in space, similar to the image produced by the crosscorrelation of the various Cartesian components of the vector displacements. However, in this case, the images correspond to various combinations of incident P or S and reflected P- or S-waves, thus having clear physical meaning and being easier to interpret for physical properties.

2.5 Extended elastic imaging conditions

The conventional imaging condition from equation 2.2 discussed in the preceding section uses zero space- and time-lags of the crosscorrelation between the source and receiver wavefields. This imaging condition represents a special case of a more general form of an

extended imaging condition (Sava & Fomel, 2006b)

$$I(\mathbf{x},\boldsymbol{\lambda},\tau) = \int u_s(\mathbf{x}-\boldsymbol{\lambda},t-\tau)\, u_r(\mathbf{x}+\boldsymbol{\lambda},t+\tau)\, dt\,, \tag{2.8}$$

where $\boldsymbol{\lambda} = \{\lambda_x, \lambda_y, \lambda_z\}$ and τ stand for crosscorrelation lags in space and time, respectively. The imaging condition from equation 2.2 is equivalent to the extended imaging condition from equation 2.8 for $\boldsymbol{\lambda} = \mathbf{0}$ and $\tau = 0$.

The extended imaging condition has two main uses. First, it characterizes wavefield reconstruction errors, since for incorrectly reconstructed wavefields, the crosscorrelation energy does not focus completely at zero lags in space and time. Sources of wavefield reconstruction errors include inaccurate numeric solutions to the wave equation, inaccurate models used for wavefield reconstruction, inadequate wavefield sampling on the acquisition surface, and uneven illumination of the subsurface. Typically, all these causes of inaccurate wavefield reconstruction occur simultaneously and it is difficult to separate them after imaging. Second, assuming accurate wavefield reconstruction, the extended imaging condition can be used for angle decomposition. This leads to representations of reflectivity as a function of angles of incidence and reflection at all points in the imaged volume (Sava & Fomel, 2003). Here, I assume that wavefield reconstruction is accurate and concentrate on further extensions of the imaging condition, such as angle decomposition.

2.5.1 Imaging with vector displacements

For imaging with vector wavefields, the extended imaging condition from equation 2.8 can be applied directly to the various components of the reconstructed source and receiver wavefields, similar to the conventional imaging procedure described in the preceding section. Therefore, an extended image constructed from vector displacement wavefields is

$$I_{ij}(\mathbf{x},\boldsymbol{\lambda},\tau) = \int u_{si}(\mathbf{x}-\boldsymbol{\lambda},t-\tau)\, u_{rj}(\mathbf{x}+\boldsymbol{\lambda},t+\tau)\, dt\,, \tag{2.9}$$

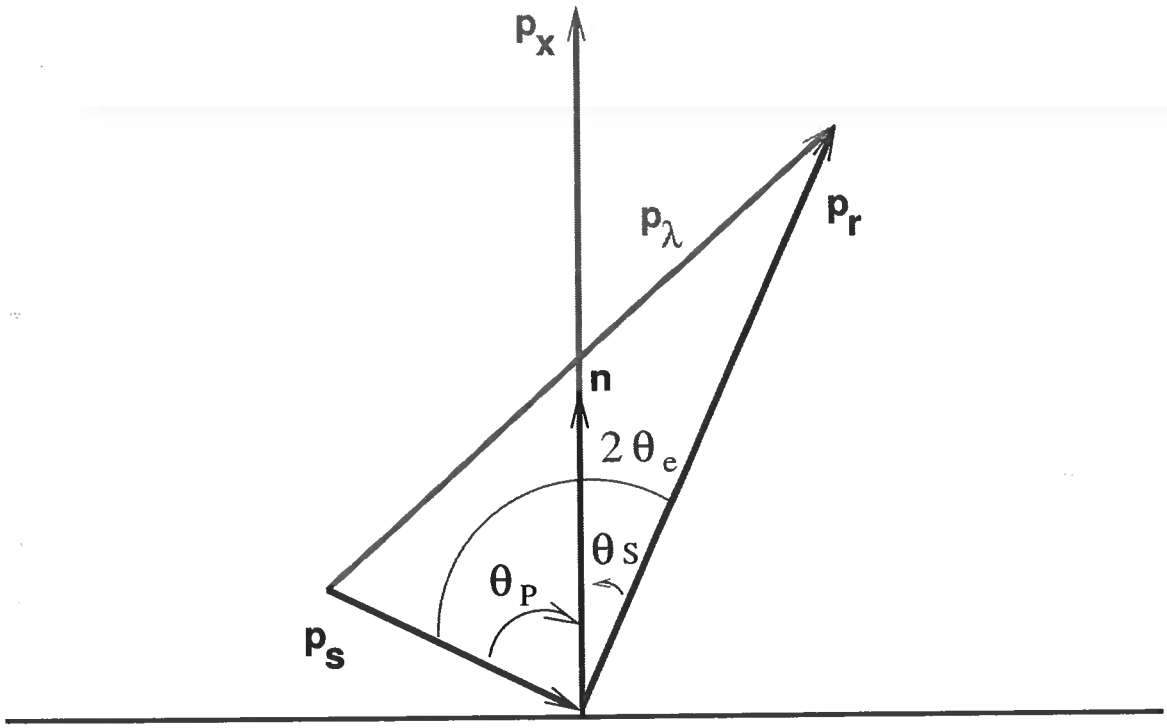

Figure 2.1. Local wave vectors of the converted wave at a common-image point location in 3D. The plot shows the conversion in the reflection plane in 2D. $\mathbf{p_s}$, $\mathbf{p_r}$, $\mathbf{p_x}$ and $\mathbf{p_\lambda}$ are ray parameter vectors for the source ray, receiver ray, and combinations of the two. The length of the incidence and reflection wave vectors are inversely proportional to the incidence and reflection wave velocity, respectively. Vector $\mathbf{n}$ is the normal of the reflector. By definition, $\mathbf{p_x} = \mathbf{p_r} - \mathbf{p_s}$ and $\mathbf{p_\lambda} = \mathbf{p_r} + \mathbf{p_s}$.

where the quantities u_{si} and u_{rj} stand for the Cartesian components x, y, z of the vector source and receiver wavefields, and $\boldsymbol{\lambda}$ and τ stand for cross-correlation lags in space and time, respectively. This imaging condition suffers from the same drawbacks described for the similar conventional imaging condition applied to the Cartesian components of the reconstructed wavefields, i.e. crosstalk between the unseparated wave modes.

2.5.2 Imaging with scalar and vector potentials

An extended imaging condition can also be designed for elastic wavefields decomposed in scalar and vector potentials, similar to the conventional imaging procedure described in the preceding section. Therefore, an extended image constructed from scalar and vector potentials is

$$I_{ij}\left(\mathbf{x},\boldsymbol{\lambda},\tau\right)=\int\alpha_{si}\left(\mathbf{x}-\boldsymbol{\lambda},t-\tau\right)\alpha_{rj}\left(\mathbf{x}+\boldsymbol{\lambda},t+\tau\right)dt\,, \tag{2.10}$$

where the quantities α_{si} and α_{rj} stand for the various wave modes $\alpha=\{P,S\}$ of the source and receiver wavefields, and $\boldsymbol{\lambda}$ and τ stand for cross-correlation lags in space and time, respectively.

2.6 Angle decomposition

As indicated earlier, the main uses of images constructed using extended imaging conditions are migration velocity analysis (MVA) and amplitude versus angle analysis (AVA). Such analyses, however, require that the images be decomposed in components corresponding to various angles of incidence. Angle decomposition takes different forms corresponding to the type of wavefields involved in imaging. Thus, I can distinguish angle decomposition for scalar (acoustic) wavefields and angle decomposition for vector (elastic) wavefields.

2.6.1 Scalar wavefields

For the case of imaging with the acoustic wave equation, the reflection angle corresponding to incidence and reflection of P-wave mode can be constructed after imaging, using

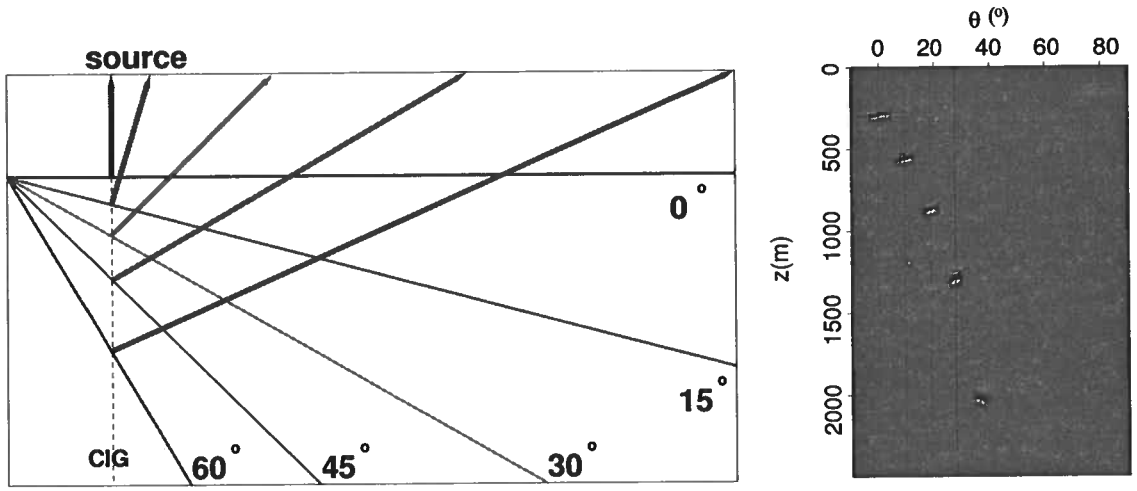

(a) (b)

Figure 2.2. (a) A model showing one shot over multiple reflectors dipping at 0°, 15°, 30°, 45°, and 60°. The vertical dashed line shows a CIG location. The incidence ray is vertically down and P to S conversions are marked by arrowed lines pointing away from reflectors. (b) Converted wave angle gather obtained from algorithm described by Sava & Fomel (2006a). Notice that converted wave angles are always smaller than incidence angles (in this case, the dips of the reflectors) except for normal incidence.

mapping based on the relation (Sava & Fomel, 2005)

$$\tan\theta_a = \frac{|\mathbf{k_\lambda}|}{|\mathbf{k_x}|}\,, \tag{2.11}$$

where θ_a is the incidence angle, and $\mathbf{k_x} = \mathbf{k_r} - \mathbf{k_s}$ and $\mathbf{k_\lambda} = \mathbf{k_r} + \mathbf{k_s}$ are defined using the source and receiver wavenumbers, $\mathbf{k_s}$ and $\mathbf{k_r}$. The information required for decomposition of the reconstructed wavefields as a function of wavenumbers $\mathbf{k_x}$ and $\mathbf{k_\lambda}$ is readily available in the images $I(\mathbf{x}, \boldsymbol{\lambda}, \tau)$ constructed by extended imaging conditions equations 2.9 or 2.10. After angle decomposition, the image $I(\mathbf{x}, \theta, \phi)$ represents a mapping of the image $I(\mathbf{x}, \boldsymbol{\lambda}, \tau)$ from offsets to angles. In other words, all information for characterizing angle-dependent reflectivity is already available in the image obtained by the extended imaging conditions.

2.6.2 Vector wavefields

A similar approach can be used for decomposition of the reflectivity as a function of incidence and reflection angles for elastic wavefields imaged with extended imaging conditions equations 2.9 or 2.10. The angle θ_e characterizing the average angle between incidence and reflected rays can be computed using the expression (Sava & Fomel, 2005)

$$\tan^2\theta_e = \frac{(1+\gamma)^2\,|\mathbf{k_\lambda}|^2 - (1-\gamma)^2\,|\mathbf{k_x}|^2}{(1+\gamma)^2\,|\mathbf{k_x}|^2 - (1-\gamma)^2\,|\mathbf{k_\lambda}|^2}\,, \tag{2.12}$$

where γ is the velocity ratio of the incident and reflected waves, e.g. V_P/V_S ratio for incident P mode and reflected S mode. Figure 2.1 shows the schematic and the notations used in equation 2.12, where $|\mathbf{p_x}| = |\mathbf{k_x}|/\omega$, $|\mathbf{p_\lambda}| = |\mathbf{k_\lambda}|/\omega$, and ω is the angular frequency at the imaging location $\mathbf{x}$. The angle decomposition equation 2.12 is designed for PS reflections and reduces to equation 2.11 for PP reflections when $\gamma = 1$.

Angle decomposition using equation 2.12 requires computation of an extended imaging condition with 3D space lags $(\lambda_x, \lambda_y, \lambda_z)$, which is computationally costly. Faster computation can be done if one avoids computing the vertical lag λ_z, in which case the angle

decomposition can be done using the expression (Sava & Fomel, 2005):

$$\tan\theta_e = \frac{(1+\gamma)\,(a_{\lambda_x}+b_x)}{2\gamma\,k_z + \sqrt{4\gamma^2 k_z^2 + (\gamma^2-1)\,(a_{\lambda_x}+b_x)\,(a_x+b_{\lambda_x})}}\,, \tag{2.13}$$

where $a_{\lambda_x} = (1+\gamma)\,k_{\lambda_x}$, $a_x = (1+\gamma)\,k_x$, $b_{\lambda_x} = (1-\gamma)\,k_{\lambda_x}$, and $b_x = (1-\gamma)\,k_x$. Figure 2.2 shows a model of five reflectors and the extracted angle gathers for these reflectors at the location of the source. For PP reflections, they would occur in the angle gather at angles equal with the reflector slopes. However, for PS reflections, as illustrated in Figure 2.2, the reflection angles are smaller than the reflector slopes, as expected.

2.7 Examples

I test the different imaging conditions discussed in the preceding sections with data simulated on a modified subset of the Marmousi II model (Martin *et al.*, 2002). The section is chosen to be at the left side of the entire model which is relatively simple, and therefore it is easier to examine the quality of the images.

2.7.1 Imaging with vector displacements

Consider the images obtained for the model depicted in Figures 2.3(a) and (b). Figure 2.3(a) depicts the P-wave velocity (smooth function between $1.6 - 3.2$ km/s), and Figure 2.3(b) shows the density (variable between $1.0 - 2.0$ g/cm^3). The S-wave velocity is a scaled version of the P-wave velocity with $V_P/V_S = 2$. I use a smooth velocity background for both modeling and migration. I use density discontinuities to generate reflections in modeling but use a constant density in migration. The smooth velocity background for both modeling and migration is used to avoid back-scattering during wavefield reconstruction. The elastic data, shown in Figures 2.4(a) and (b), are simulated using a space-time staggered-grid finite-difference solution to the isotropic elastic wave equation (Virieux, 1984, n.d.; Mora, 1987, 1988). I simulate data for a source located at position $x = 6.75$ km and $z = 0.5$ km. Since I am using an explosive source and the background velocity is smooth, the simulated wavefield is represented mainly by P-wave incident energy and the receiver

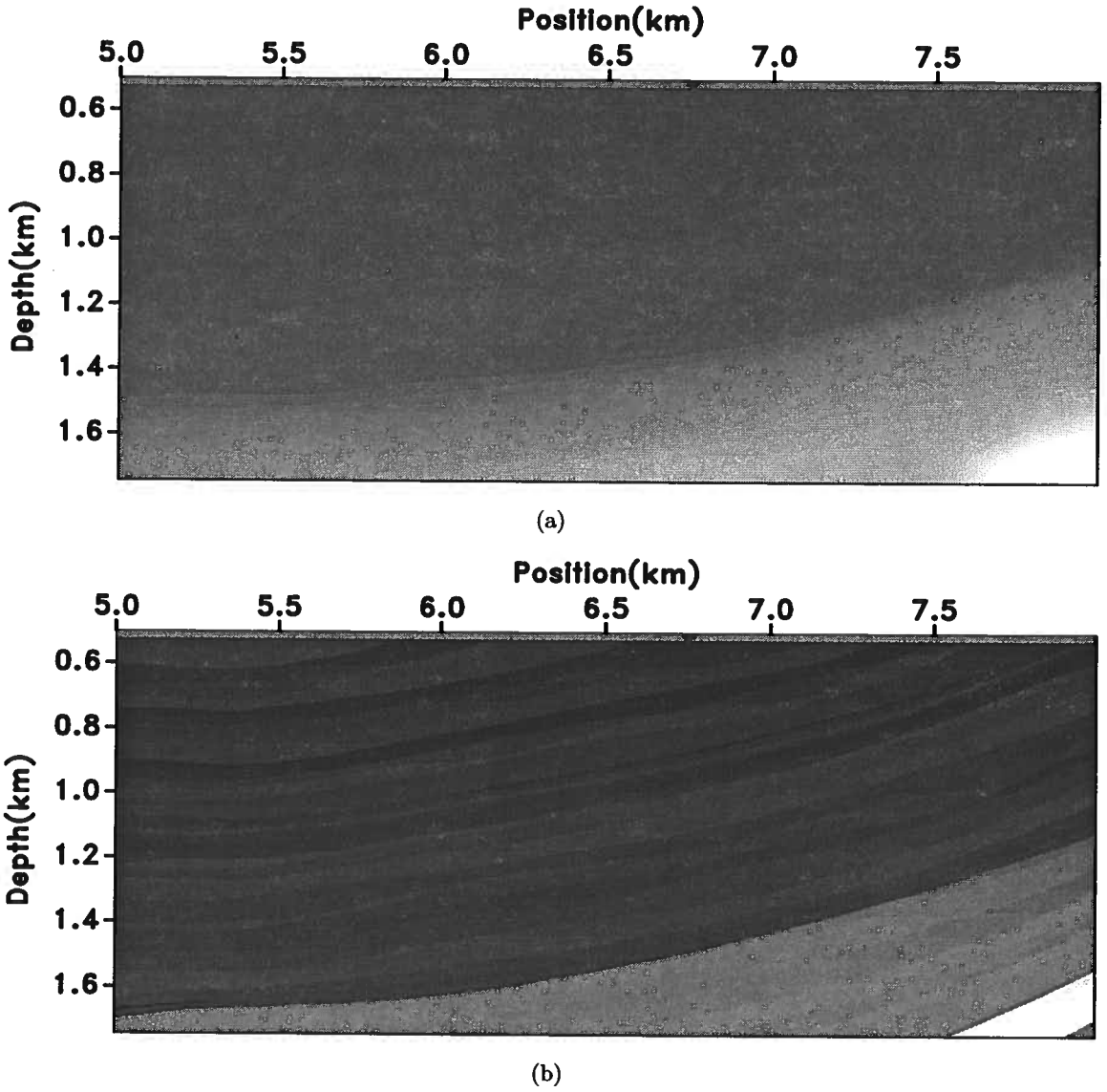

Figure 2.3. (a) P- and S-wave velocity models and (b) density model used for isotropic elastic wavefield modeling, where V_P ranges from 1.6 to 3.2 km/s from top to bottom and $V_P/V_S = 2$, and density ranges from 1.0 to 2.0 g/cm^3 .

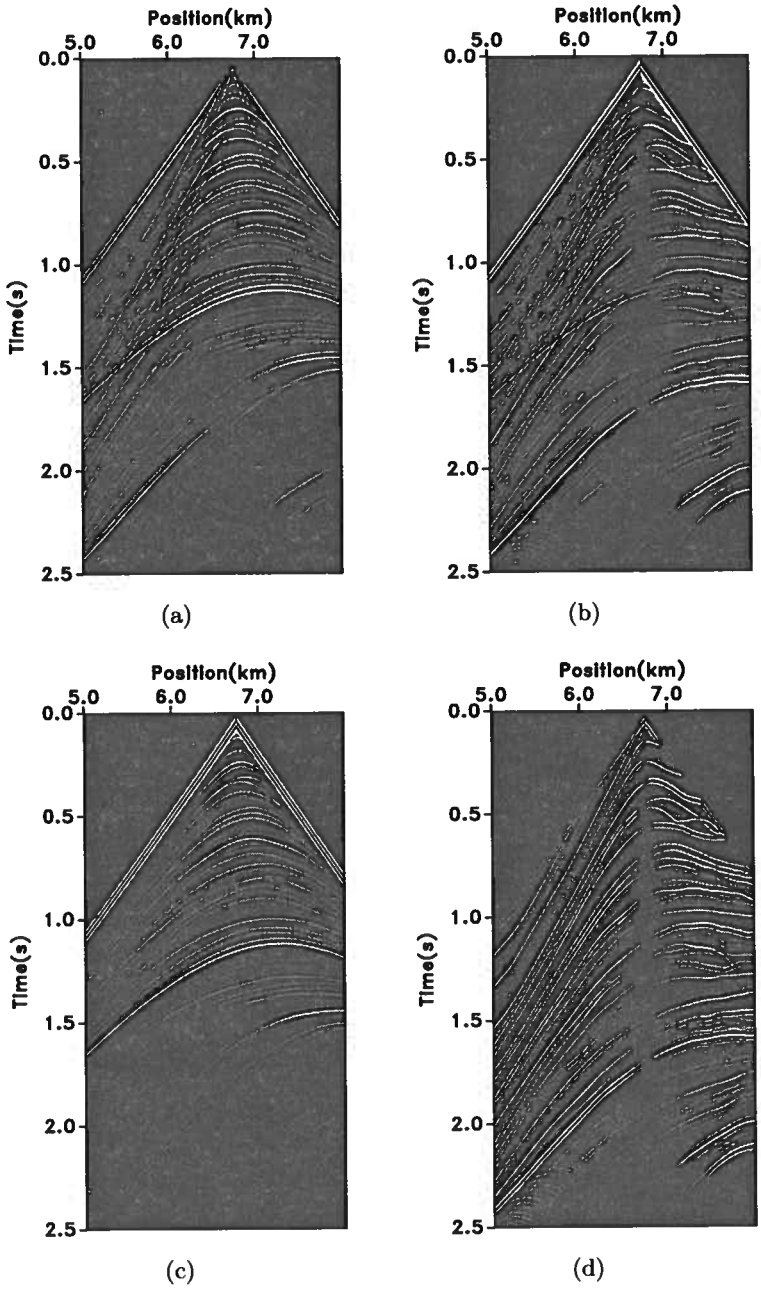

Figure 2.4. Elastic data simulated in model 2.3(a) and 2.3(b) with a source at $x = 6.75$ km and $z = 0.5$ km, and receivers along $z = 0.5$ km: (a) vertical component, (b) horizontal component, (c) scalar potential and (d) vector potential of the elastic wavefield. Both vertical and horizontal components, panels (a) and (b), contain a mix of P and S modes, as seen by comparison with panels (c) and (d).

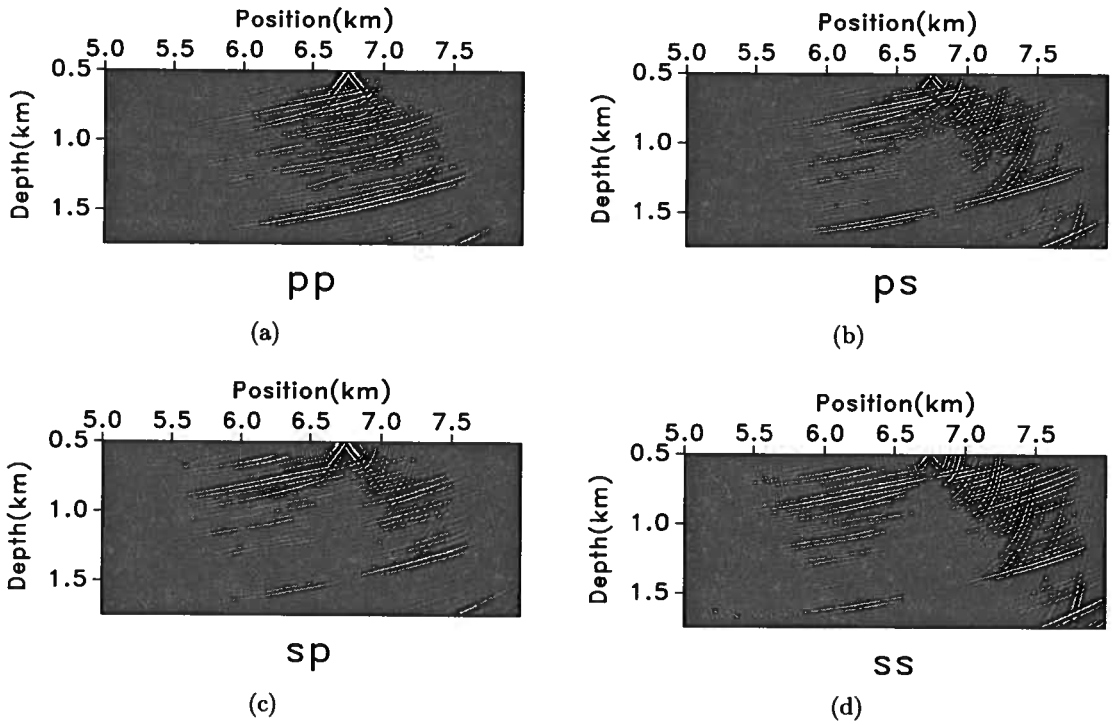

Figure 2.5. Images produced with the displacement components imaging condition from equation 2.3. Panels (a), (b), (c), and (d) correspond to the crosscorrelation of the vertical and horizontal components of the source wavefield with the vertical and horizontal components of the receiver wavefield, respectively. Images (a) to (d) are the zz, zx, xz, and xx components, respectively. The image corresponds to one shot at position $x = 6.75$ km and $z = 0.5$ km. Receivers are located at all locations at $z = 0.5$ km.

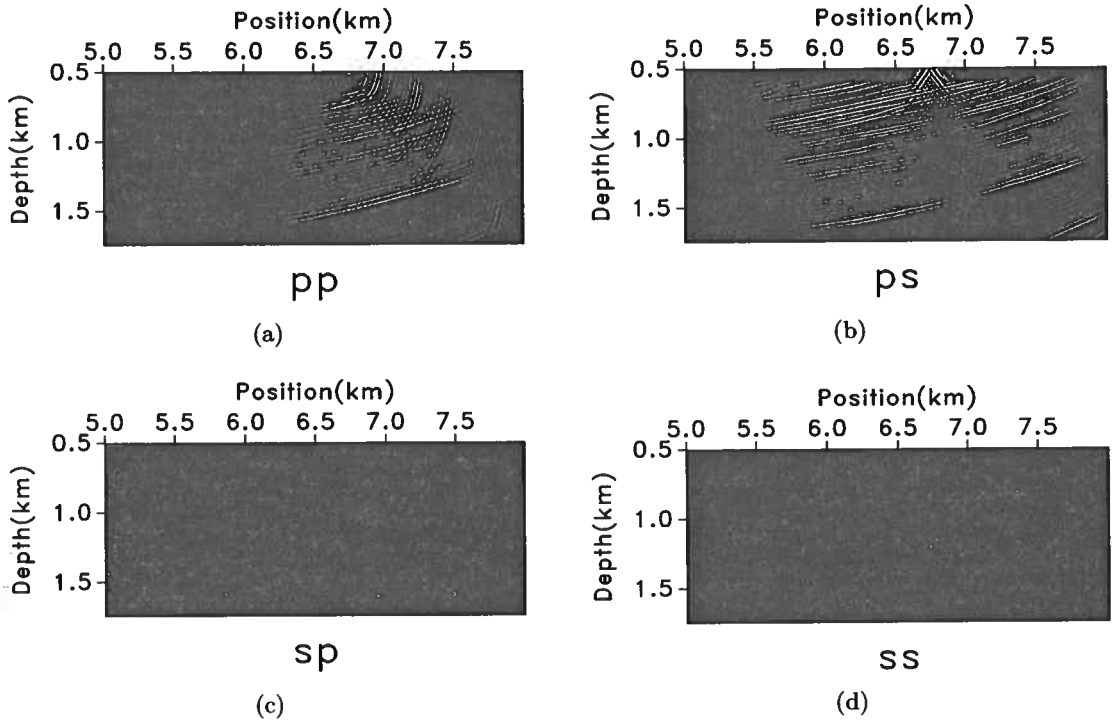

Figure 2.6. Images produced with the scalar and vector potentials imaging condition from equation 2.7. Panels (a), (b), (c), and (d) correspond to the crosscorrelation of the P and S components of the source wavefield with the P and S components of the receiver wavefield, respectively. Images (a) to (d) are the PP, PS, SP, and SS components, respectively. The image corresponds to one shot at position $x = 6.75$ km and $z = 0.5$ km. Receivers are located at all locations at $z = 0.5$ km. Panels (c) and (d) are blank because an explosive source was used to generate synthetic data.

wavefield is represented by a combination of P- and S-wave reflected energy. The data contain a mix of P and S modes, as can be seen by comparing the vertical and horizontal displacement components, shown in Figures 2.4(a) and (b), with the separated P and S wave modes, shown in Figures 2.4(c) and (d).

Imaging the data shown in Figures 2.4(a) and (b) using the imaging condition from equation 2.3, I obtain the images depicted in Figures 2.5(a) to (d). Figures 2.5(a) to (d) correspond to the crosscorrelation of the z and x components of the source wavefield with the z and x components of the receiver wavefield, respectively. Since the input data do not represent separated wave modes, the images produced with the imaging condition based on vector displacements do not separate PP and PS reflectivity. Thus, the images are hard to interpret, since it is not clear what incident and reflected wave modes the reflections represent. In reality, reflections corresponding to all wave modes are present in all panels.

2.7.2 Imaging with scalar and vector potentials

Consider the images (Figures 2.6(a) to (d)) obtained imaging condition from equation 2.7 applied to the data (Figures 2.4(a) and (b)) from the preceding example. Because I used an explosive source for the simulation, the source wavefield contains mostly P-wave energy, while the receiver wavefield contains P- and S-wave mode energy. Helmholtz decomposition after extrapolation but prior to imaging isolates P and S wavefield components. Therefore, migration produces images of reflectivity corresponding to PP and PS reflections, Figures 2.6(a) and (b), but not reflectivity corresponding to SP or SS reflections, Figures 2.6(c) and (d). The illumination regions are different between PP and PS images, due to different illumination angles of the two propagation modes for the given acquisition geometry. The PS image, Figure 2.6(b), also shows the usual polarity reversal for positive and negative angles of incidence measured relative to the reflector normal. By comparing Figures 2.6(a) and (b) with Figures 2.5(a) and (b), it is apparent that the crosstalk in the images obtained from displacement-based imaging condition is more prominent than the one

obtained from potential-based imaging conditions, especially in Figure 2.5(a). Furthermore, the polarity in Figure 2.5(b), normally taken as the PS image, does not reverse polarity at normal incidence, which is not correct either.

2.7.3 Angle decomposition

The images shown in the preceding subsection correspond to the conventional imaging conditions from equations 2.3 and 2.7. I construct other images using the extended imaging conditions from equations 2.9 and 2.10, which can be used for angle decomposition after imaging. Then, I can use equation 2.13 to compute angle gathers from horizontal space cross-correlation lags.

Figures 2.7(a) and (c) together with Figures 2.7(b) and (d) show, respectively, the PP and PS horizontal lag- and angle-gathers for the common-image gather (CIG) location in the middle of the reflectivity model, given a single source at $x = 6.75$ km and $z = 0.5$ km. PP and PS horizontal lag gathers present lines dipping at angles that are equal to the incidence angles (real incidence angles for PP reflection and average of incidence and reflection angles for PS reflection) at the CIG location. PP angles are larger than PS angles at all reflectors, as illustrated on the simple synthetic example shown in Figure 2.2.

Figures 2.8(a) and (c) together with Figures 2.8(b) and (d) show, respectively, the PP and PS horizontal lag- and angle-gathers for the same CIG location, given many sources from $x = 5.5$ to 7.5 km and $z = 0.5$ km. The horizontal space cross-correlation lags are focused around $\boldsymbol{\lambda} = \mathbf{0}$, which justifies the use of conventional imaging condition extracting the crosscorrelation of the source and receiver wavefields at zero lag in space and time. Thus, the zero lag of the images obtained by extended imaging condition represent the image at the particular CIG location. The PP and PS gathers for many sources are flat, since the migration was done with correct migration velocity. The PS angle gather, depicted in Figure 2.8(d), shows a polarity reversal at $\theta = 0$ as expected.

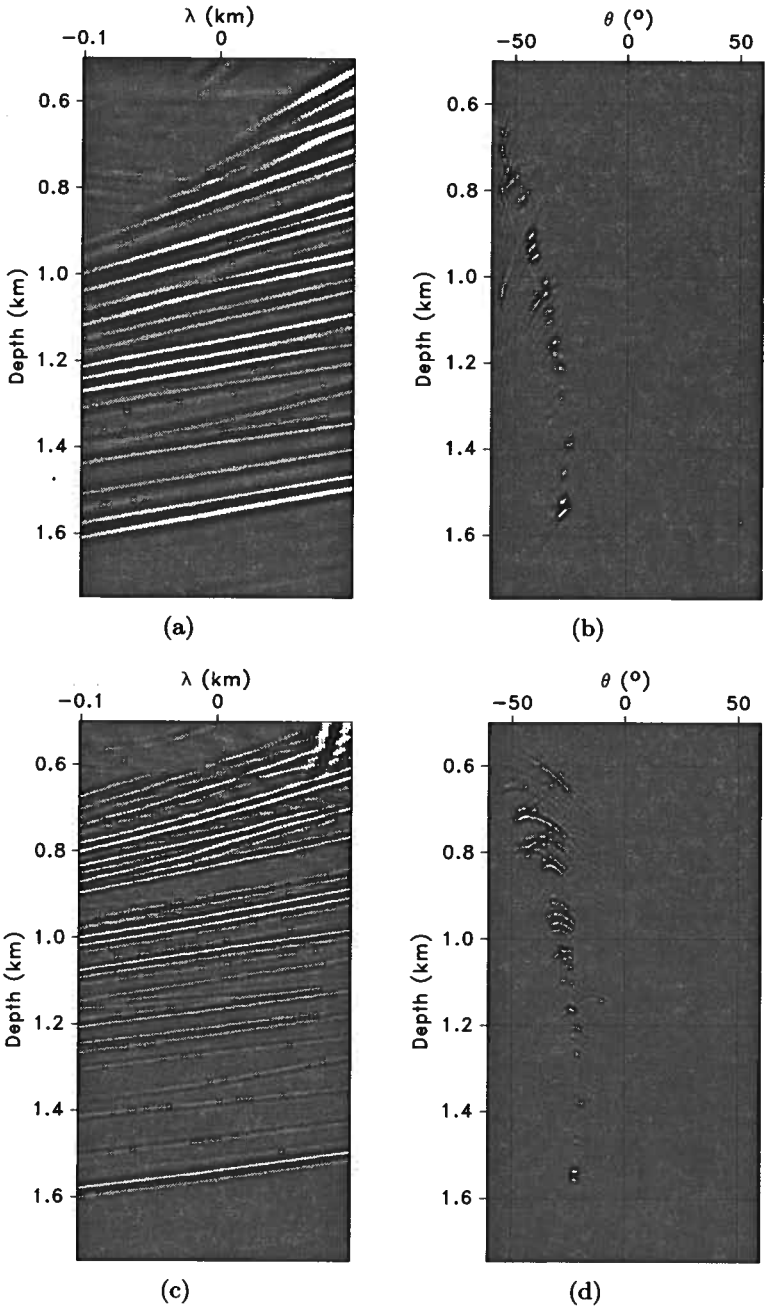

Figure 2.7. Horizontal cross-correlation lags for (a) PP and (c) PS reflections for the model in Figures 2.3(a) and (b). The source is at $x = 6.75$ km and the CIG is located at $x = 6.5$ km. Panels (b) and (d) depict PP and PS angle gathers decomposed from the horizontal lag gathers in panels (a) and (c), respectively. As expected, PS angles are smaller than PP angles for a particular reflector due to smaller reflection angles.

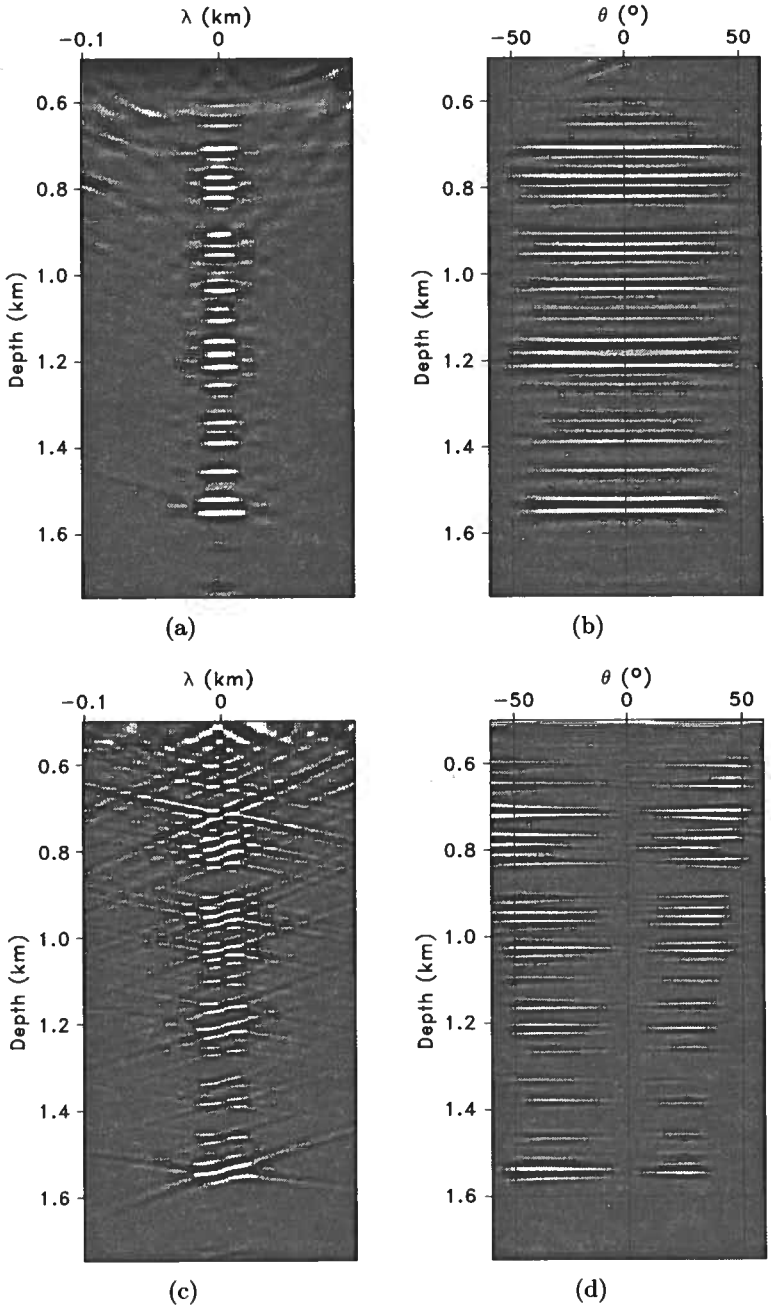

Figure 2.8. Horizontal cross-correlation lags for PP (a) and PS (c) reflections for the model in Figures 2.3(a) and (b). These CIGs correspond to 81 sources from $x = 5.5$ to 7.5 km at $z = 0.5$ km. The CIG is located at $x = 6.5$ km. Panels (b) and (d) depict PP and PS angle gathers decomposed from the horizontal lag gathers in panels (a) and (c), respectively. Since the velocity used for imaging is correct, the PP and PS gathers are flat. The PP angle gathers do not change polarity at normal incidence, but the PS angle gathers change polarity at normal incidence.

2.8 Discussion

The presentation of the angle-domain reverse time migration method outlined in the preceding sections deliberately ignores several practical challenges in order to maintain the focus of this chapter to the actual elastic imaging condition. However, for completeness, I would like to briefly mention several complementary issues that need to be addressed in conjunction with the imaging condition in order to design a practical method for elastic reverse time migration.

First, reconstruction of the receiver wavefield requires that the multicomponent recorded data be injected into the model in reverse time. In other words, the recorded data act as a displacement sources at receiver positions. In elastic materials, displacement sources trigger both compressional and transverse wave modes, no matter what portion of the recorded elastic wavefield is used as a source. For example, injecting a recorded compressional mode triggers both a compressional (physical) mode and a transverse (non-physical) mode in the subsurface . Both modes propagate in the subsurface and might correlate with wave modes from the source side. There are several ways to address this problem, such as by imaging in the angle-domain where the non-physical modes appear as events with non-flat move-out. One can make an analogy between these non-physical waves and multiples that also lead to non-flat events in the angle-domain. Thus, the source injection artifacts might be eliminated by filtering the migrated images in the angle domain, similar to the technique employed by Sava & Guitton (2005) for suppressing multiples after imaging.

Second, the data recorded at a free surface contain both up-going and down-going waves. Ideally, one should use only the up-going waves as a source for reconstructing the elastic wavefields by time-reversal. In the examples, I assume an absorbing surface in order to avoid this additional complication and concentrate on the imaging condition. However, practical implementations require directional separation of waves at the surface (Wapenaar & Haimé, 1990; Wapenaar *et al.*, 1990; Admundsen & Reitan, 1995; Admundsen *et al.*, 2001; Hou & Marfurt, 2002). Furthermore, a free surface allows other wave modes to be

generated in the process of wavefield reconstruction using the elastic wave equation, e.g. Rayleigh and Love waves. Although these waves do not propagate deep into the model, they might interfere with the directional wavefield separation at the surface.

Third, I suggest in this chapter that angle-dependent reflectivity constructed using extended imaging conditions might allow for elastic AVA analysis. This theoretical possibility requires that the wavefields are correctly reconstructed in the subsurface to account for accurate amplitude variation. For example, boundaries between regions with different material properties need to be reasonably located in the subsurface to generate correct mode conversions, and the radiation pattern of the source also needs to be known. None of these aspects is part of my analyses, but they represent important considerations for practical elastic wavefield imaging.

Fourth, the wave-mode separation using divergence and curl operators, as required by Helmholtz decomposition, does not work well in elastic anisotropic media. Anisotropy requires that the separation operators take into account the local anisotropic parameters that may vary spatially. This extension will be presented in the next chapter.

2.9 Conclusions

I present a method for reverse time migration with angle-domain imaging formulated for multicomponent elastic data. The method is based on the separation of elastic wavefields reconstructed in the subsurface into pure wave-modes using conventional Helmholtz decomposition. Elastic wavefields from the source and receivers are separated into pure compressional and transverse wave-modes which are then used for angle-domain imaging. The images formed using this procedure are interpretable in terms of the subsurface physical properties, for example, by analyzing the PP or PS angle-dependent reflectivity. In contrast, images formed by simple crosscorrelation of Cartesian components of reconstructed elastic wavefields mix contributions from P and S reflections and are harder to interpret. Artifacts caused by back-propagating the recorded data with displacement sources are present in

both types of images, although they are easier to distinguish and attenuate on the images constructed with pure elastic wave-modes separated prior to imaging.

The methodology is advantageous not only because it forms images with clearer physical meaning, but also because it is based on more accurate physics of wave propagation in elastic materials. For example, this methodology allows for wave-mode conversions in the process of wavefield reconstruction. This is in contrast with alternative methods for multicomponent imaging which separate wave-modes on the surface and then image those independently. In addition, elastic images can be formed in the angle-domain using extended imaging conditions, which offers the potential for migration velocity analysis (MVA) and amplitude versus angle (AVA) analysis.

Chapter 3

Elastic wavefield separation for VTI media

3.1 Summary

Wave propagation in anisotropic media can be modeled with elastic wave equations which correctly characterizes both kinematics and dynamics. However, because P and S modes are both propagated using elastic wave equations, there is a need to separate P and S modes to obtain images that represent reflection coefficients of different reflection types. The separation of wave modes into P and S from isotropic elastic wavefields is typically done using Helmholtz decomposition. However, Helmholtz decomposition using conventional divergence and curl operators in anisotropic media does not give satisfactory results and leaves the different wave modes only partially separated. The separation of anisotropic wavefields requires the use of more sophisticated operators which depend on local material parameters. Anisotropic wavefield separation operators are constructed using the polarization vectors evaluated by solving the Christoffel equation at each point of the medium. These polarization vectors can be represented in the space domain as localized filtering operators, which resemble conventional derivative operators. The spatially-variable "pseudo" derivative operators perform well in heterogeneous VTI media even in areas of rapid velocity/density variations. Synthetic results indicate that the operators can be used to separate wavefields for VTI media with arbitrary strength of anisotropy.

3.2 Introduction

Wave equation migration for elastic data usually consists of two steps. The first step is wavefield reconstruction in the subsurface from data recorded at the surface. The second

step is the application of an imaging condition which extracts reflectivity information from the reconstructed wavefields.

The elastic wave equation migration for multicomponent data can be implemented in two ways. The first approach is to separate recorded elastic data into compressional and transverse (P and S) modes and use the separated data for acoustic wave equation migration separately. This acoustic imaging approach to elastic waves is more frequently used, but it is fundamentally based on the assumption that P and S data can be successfully separated on the surface, which is not always true (Etgen, 1988; Zhe & Greenhalgh, 1997). The second approach is to extrapolate the entire elastic wavefield at once, and then separate wave modes prior to applying an imaging condition. The reconstruction of elastic wavefields can be implemented using various techniques, including by time reversal (RTM) (Chang & McMechan, 1986, 1994) or by Kirchhoff integral techniques (Hokstad, 2000).

The imaging condition applied to the reconstructed vector wavefields directly determines the quality of the images. Conventional crosscorrelation imaging condition does not separate the wave modes and crosscorrelates the Cartesian components of the elastic wavefields. In general, the various wave modes (P and S) are mixed on all wavefield components and cause crosstalk and image artifacts. In Chapter 2, I suggest using imaging conditions based on elastic potentials, which require crosscorrelation of separated modes. Potential-based imaging condition creates images that have clear physical meaning, in contrast with images obtained with Cartesian wavefield components, thus justifying the need for wave mode separation.

As the need for anisotropic imaging increases, more processing and migration are performed based on anisotropic acoustic one-way wave equations (Alkhalifah, 1998, 2000; Shan, 2006; Shan & Biondi, 2005; Fletcher *et al.*, 2009; Fowler *et al.*, 2010). However, much less research has been done on anisotropic elastic migration based on two-way wave equations. Elastic Kirchhoff migration (Hokstad, 2000) obtains pure-mode and converted mode images by downward continuation of elastic vector wavefields with a visco-elastic wave

equation. The wavefield separation is effectively done with elastic Kirchhoff integration, which handles both P and S waves. However, Kirchhoff migration does not perform well in areas of complex geology where ray theory breaks down (Gray *et al.*, 2001), thus requiring migration with more accurate methods, such as reverse time migration.

One of the complexities that impedes anisotropic migration using elastic wave equation is the difficulty to separate anisotropic wavefields into different wave modes after reconstructing the elastic wavefields. However, the proper separation of anisotropic wave modes is as important for anisotropic elastic migration as is the separation of isotropic wave modes for isotropic elastic migration. The main difference between anisotropic and isotropic wavefield separation is that Helmholtz decomposition is only suitable for the separation of isotropic wavefields.

In this chapter, I show how to construct wavefield separators for VTI (transverse isotropic with a vertical symmetry axis) media applicable to models with spatially varying parameters. I apply these operators to anisotropic elastic wavefields and show that they successfully separate anisotropic wave modes, even for media with strong anisotropy.

The main application of this technique is to elastic reverse time migration. In this case, complete wavefields containing both P and S wave modes are reconstructed from recorded data. The reconstructed wavefields are separated into pure wave modes prior to the application of a conventional crosscorrelation imaging condition. I limit the scope of this chapter only to the wave-mode separation procedure in highly heterogeneous media, although the ultimate goal of this procedure is to aid elastic RTM.

3.3 Separation method

Separation of scalar and vector potentials can be achieved by Helmholtz decomposition, which is applicable to any vector field $\mathbf{W}(x, y, z)$. By definition, the vector wavefield $\mathbf{W}$ can be decomposed into a curl-free scalar potential Θ and a divergence-free vector potential

$\mathbf{\Psi}$ according to the relation (Aki & Richards, 2002):

$$\mathbf{W} = \nabla\Theta + \nabla \times \mathbf{\Psi}\,. \tag{3.1}$$

Equation 3.1 is not used directly in practice, but the scalar and vector components are obtained indirectly by the application of the divergence and curl operators to the extrapolated elastic wavefield:

$$P = \nabla \cdot \mathbf{W}\,, \tag{3.2}$$

$$\mathbf{S} = \nabla \times \mathbf{W}\,. \tag{3.3}$$

For isotropic elastic fields far from the source, quantities P and $\mathbf{S}$ describe compressional and shear wave modes, respectively (Aki & Richards, 2002).

Equations 3.2 and 3.3 allow one to understand why divergence and curl pass compressional and transverse wave modes, respectively. In the discretized space domain, one can write:

$$P = \nabla \cdot \mathbf{W} = D_x[W_x] + D_y[W_y] + D_z[W_z]\,, \tag{3.4}$$

where D_x, D_y, and D_z represent spatial derivatives in the x, y, and z directions, respectively. Applying derivatives in the space domain is equivalent to applying finite difference filtering to the functions. Here, $D\,[\cdot]$ represents spatial filtering of the wavefield with finite difference operators. In the Fourier domain, one can represent the operators D_x, D_y, and D_z by $i\,k_x$, $i\,k_y$, and $i\,k_z$, respectively; therefore, one can write an equivalent expression to equation 3.4 as:

$$\widetilde{P} = i\,\mathbf{k} \cdot \widetilde{\mathbf{W}} = i\,k_x\,\widetilde{W}_x + i\,k_y\,\widetilde{W}_y + i\,k_z\,\widetilde{W}_z\,, \tag{3.5}$$

where $\mathbf{k} = \{k_x, k_y, k_z\}$ represents the wave vector, and $\widetilde{\mathbf{W}}(k_x, k_y, k_z)$ is the 3D Fourier transform of the wavefield $\mathbf{W}(x, y, z)$. We see that in this domain, the operator $i\,\mathbf{k}$ essentially projects the wavefield $\widetilde{\mathbf{W}}$ onto the wave vector $\mathbf{k}$, which represents the polarization direction for P waves. Similarly, the curl operator projects the wavefield onto the direction orthogonal

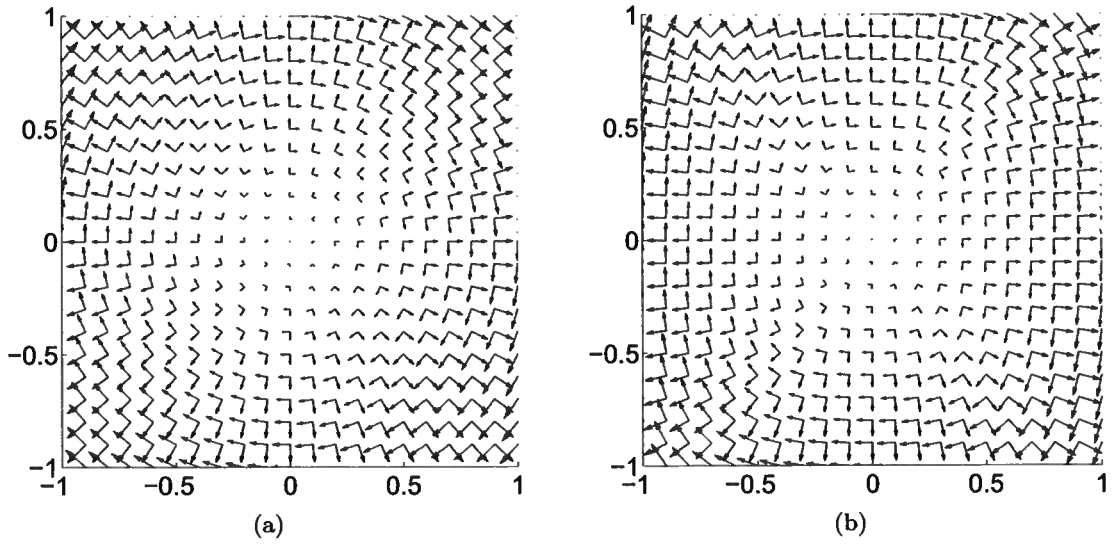

Figure 3.1. P and S polarization vectors as a function of normalized wavenumbers k_x and k_z ranging from -1 to $+1$ cycles, for (a) an isotropic model with $V_P = 3$ km/s and $V_S = 1.5$ km/s, and (b) an anisotropic (VTI) model with $V_{P0} = 3$ km/s, $V_{S0} = 1.5$ km/s, $\epsilon = 0.25$, and $\delta = -0.29$. The P-wave polarization vectors point radially (exactly for the isotropic medium and roughly for the VTI medium), and the SV-wave polarization vectors are orthogonal to the P-vectors for a given wave vector $\mathbf{k}$.

to the wave vector $\mathbf{k}$, which represents the polarization direction for S waves (Dellinger & Etgen, 1990). For illustration, Figure 3.1(a) shows the polarization vectors of the P mode of a 2D isotropic model as a function of normalized k_x and k_z ranging from -1 to 1 cycles. The polarization vectors are radial because the P waves in an isotropic medium are polarized in the same directions as the wave vectors.

Dellinger & Etgen (1990) suggest to extend wave mode separation to anisotropic media by projecting the wavefields onto the directions in which the P and S modes are polarized. This requires modification of the wave-separation equation 3.5 by projecting the wavefields onto the true polarization directions $\mathbf{U}$ to obtain P-waves:

$$\widetilde{P} = i\,\mathbf{U}(\mathbf{k}) \cdot \widetilde{\mathbf{W}} = i\,U_x\,\widetilde{W}_x + i\,U_y\,\widetilde{W}_y + i\,U_z\,\widetilde{W}_z\,. \tag{3.6}$$

In anisotropic media, $\mathbf{U}(k_x, k_y, k_z)$ is different from $\mathbf{k}$, as illustrated in Figure 3.1(b), which

shows the polarization vectors of P wave mode for a 2D VTI anisotropic model with normalized k_x and k_z ranging from -1 to 1 cycles. Polarization vectors are not radial because P waves in an anisotropic medium are not polarized in the same directions as wave vectors, except in the isotropy plane ($k_z = 0$) and along the symmetry axis ($k_x = 0$).

Dellinger & Etgen (1990) demonstrate wave mode separation in the wavenumber domain using projection of the polarization vectors, as indicated in equation 3.6. However, for heterogeneous media, this equation breaks down because the polarization vectors are spatially varying. One can write an expression equivalent to equation 3.6 in the space domain for each grid point as:

$$P = \nabla_a \cdot \mathbf{W} = L_x[W_x] + L_y[W_y] + L_z[W_z]\,, \tag{3.7}$$

where L_x, L_y, and L_z represent the inverse Fourier transforms of iU_x, iU_y, and iU_z, respectively. $L[\cdot]$ represents spatial filtering of the wavefield with anisotropic separators. L_x, L_y, and L_z define the pseudo derivative operators in the x, y, and z directions for an anisotropic medium, respectively, and they change from location to location according to the material parameters.

We obtain the polarization vectors $\mathbf{U}(\mathbf{k})$ by solving the Christoffel equation (Aki & Richards, 2002; Tsvankin, 2005):

$$\left[\mathbf{G} - \rho V^2 \mathbf{I}\right] \mathbf{U} = 0\,, \tag{3.8}$$

where $\mathbf{G}$ is the Christoffel matrix $G_{ij} = c_{ijkl} n_j n_l$, in which c_{ijkl} is the stiffness tensor, n_j and n_l are the unit wave vector components in the j and l directions, and $i, j, k, l = 1, 2, 3$. The parameter V corresponds to the eigenvalues of the matrix $\mathbf{G}$. The eigenvalues V represent the phase velocities of different wave modes and are functions of the wave vector $\mathbf{k}$ (corresponding to n_j and n_l in the matrix $\mathbf{G}$). For plane waves propagating in vertical

symmetry planes of a VTI medium, one can set k_y to 0 to get

$$\begin{bmatrix} c_{11}k_x^2 + c_{55}k_z^2 - \rho V^2 & 0 & (c_{13}+c_{55})\,k_x k_z \\ 0 & c_{66}k_x^2 + c_{55}k_z^2 - \rho V^2 & 0 \\ (c_{13}+c_{55})\,k_x k_z & 0 & c_{55}k_x^2 + c_{33}k_z^2 - \rho V^2 \end{bmatrix} \begin{bmatrix} U_x \\ U_y \\ U_z \end{bmatrix} = 0\,. \qquad (3.9)$$

The middle row of this matrix characterizes the SH wave polarized in the y direction, and P and SV modes are uncoupled from the SH mode and are polarized in the vertical plane. The top and bottom rows of this equation allow one to compute the polarization vector $\mathbf{U} = \{U_x, U_z\}$(the eigenvectors of the matrix $\mathbf{G}$) of P- or SV- waves given the stiffness tensor at every location of the medium.

One can extend the procedure described here to heterogeneous media by computing two different operator for each mode at every grid point. In vertical symmetry planes of VTI media, the operators are 2D and depend on the local values of the stiffness coefficients. For each point, I pre-compute the polarization vectors as a function of the local medium parameters, and transform them to the space domain to obtain the wave mode separators. I assume that the medium parameters vary smoothly (locally homogeneous), but even for complex media, the localized operators work in the same way as the long finite difference operators. If one represents the stiffness coefficients using Thomsen parameters (Thomsen, 1986), then the pseudo-derivative operators L_x and L_z depend on ϵ, δ, V_{P0} and V_{S0}, which can be spatially varying. One can compute and store the operators for all grid points in the medium, and then use these operators to separate P and S modes from reconstructed elastic wavefields at different time steps. Thus, wavefield separation in VTI media can be achieved simply by non-stationary filtering with the operators L_x and L_z.

3.4 Operator properties

In this section, I discuss the properties of the anisotropic "derivative" operators, including order of accuracy, size, and compactness.

3.4.1 Operator orders

As shown in the previous section, the isotropic separation operators (divergence and curl) in equations 3.4 and 3.5 are exact in the x and k domains. The exact derivative operators are infinitely long series in the *discretized* space domain. In practice, when evaluating the derivatives numerically, one needs to take some approximations to make the operators short and computationally efficient. Usually, difference operators are evaluated at different orders of accuracy. The higher order the approximation is, the more accurate and longer the operator becomes. For example, the 2^{nd} order operator has coefficients $(-\frac{1}{2}, +\frac{1}{2})$, and the more accurate 4^{th} order operator has coefficients $(+\frac{1}{12}, -\frac{2}{3}, \frac{2}{3}, -\frac{1}{12})$ (Fornberg & Ghrist, 1999).

In the wavenumber domain, for isotropic media, as shown by the black line in Figure 3.2(b), the exact difference operator is ik. Appendix A shows the k domain equivalents of the 2^{nd}, 4^{th}, 6^{th}, and 8^{th} order finite difference operators, and they are plotted in Figure 3.2(b). The higher order operators have responses closer to the exact operator ik (black line). To obtain vertical and horizontal derivatives of different orders of accuracy, I weight the polarization vector $i\mathbf{k}$ components ik_x and ik_z by the weights shown in Figure 3.2(c). For VTI media, similarly, I weight the anisotropic polarization vector $i\mathbf{U}(\mathbf{k})$ components iU_x and iU_z by these same weights. The weighted vectors are then transformed back to space domain to obtain the anisotropic stencils.

3.4.2 Operator size and compactness

Figure 3.3 shows the derivative operators of 2^{nd}, 4^{th}, 6^{th}, and 8^{th} orders in the z and x directions for isotropic and VTI (ϵ=0.25, δ=-0.29) media. As we can see, isotropic operators become longer when the order of accuracy is higher. Anisotropic operators, however, do not change much in size. One can see that the central parts of the anisotropic operators look similar to their corresponding isotropic operators and change with the order of accuracy; while the outer parts of these anisotropic operators all look similar, and do not change

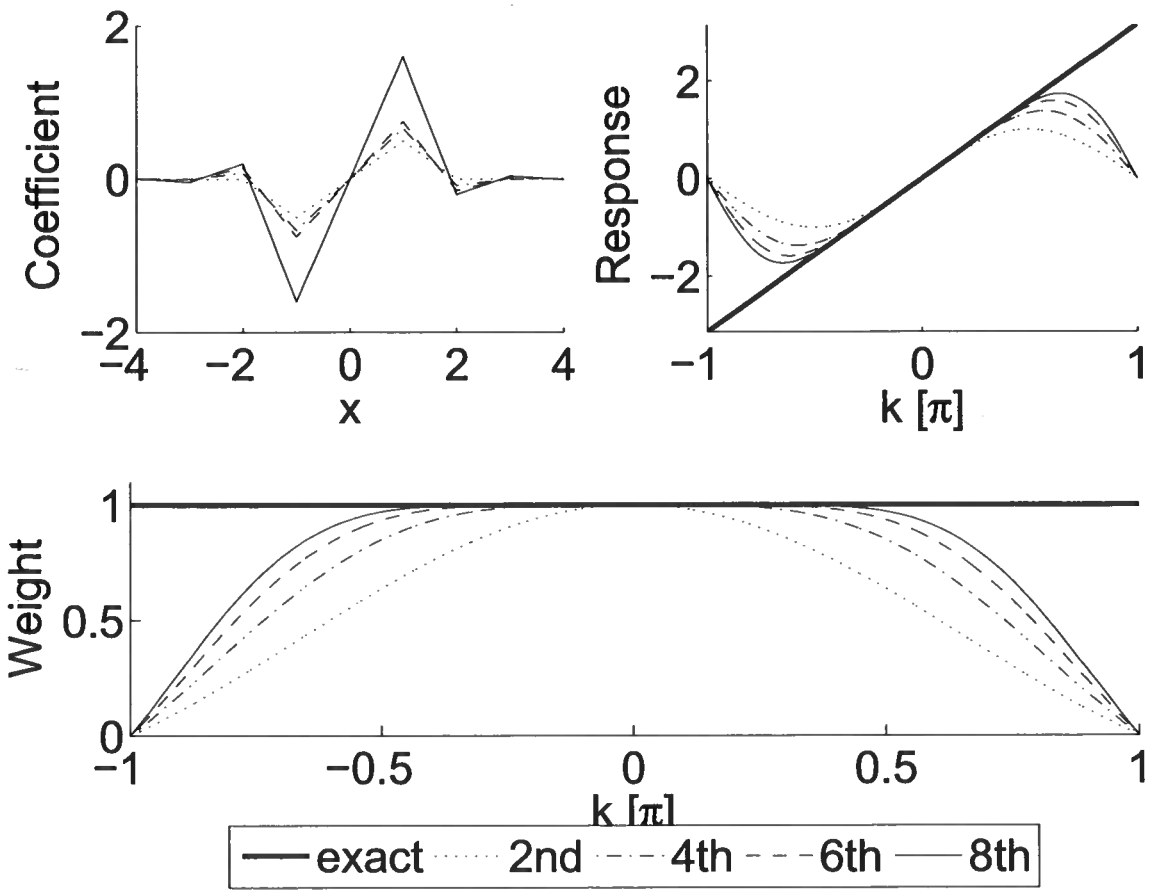

Figure 3.2. Comparison of derivative operators of different orders of accuracy (2^{nd}, 4^{th}, 6^{th}, and 8^{th} orders in space, as well as the approximation applied in Dellinger & Etgen (1990)–cosine taper) in both (a) the x domain and (b) the k domain. (c) Weights to apply to the components of the polarization vectors.

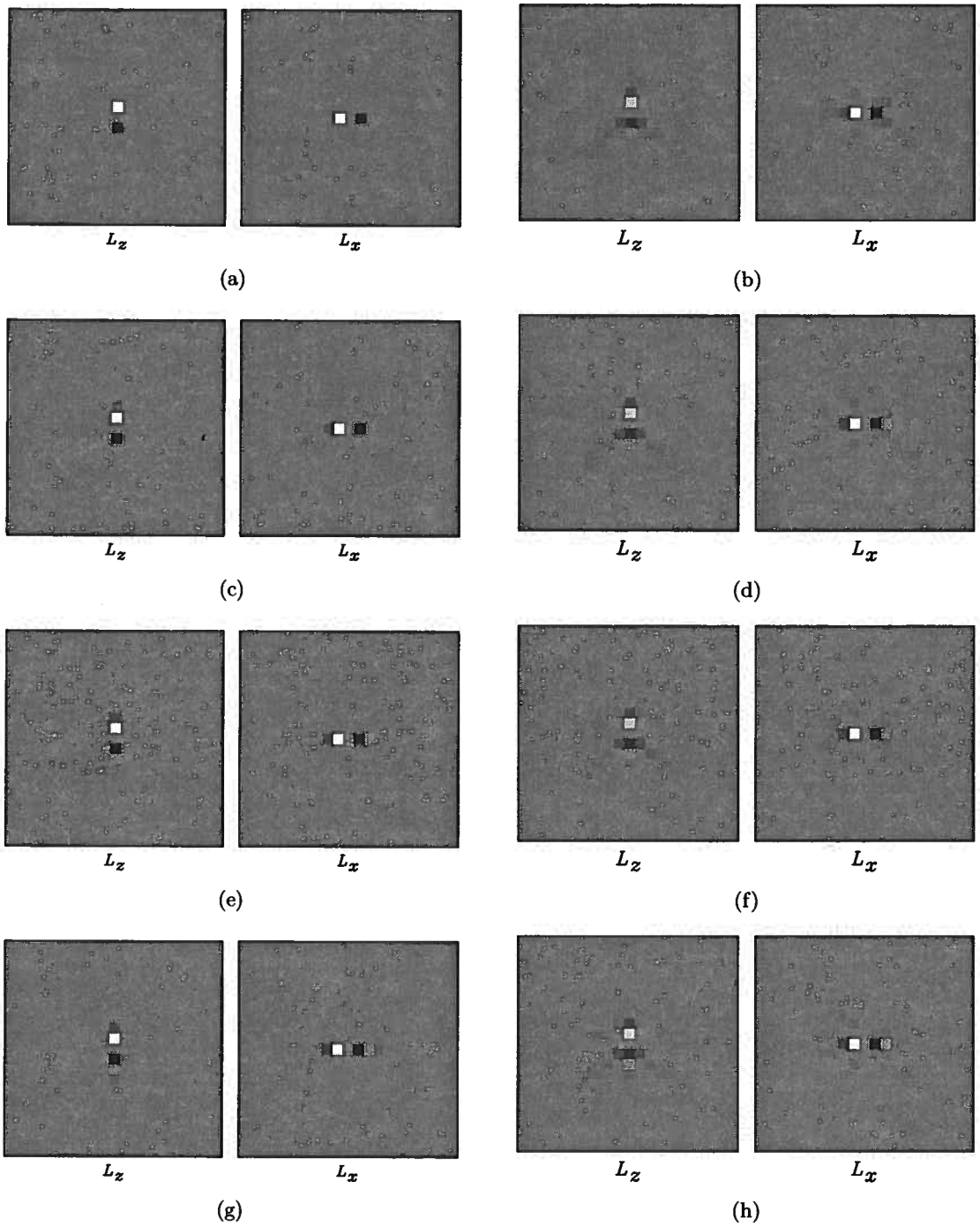

Figure 3.3. 2^{nd}, 4^{th}, 6^{th}, and 8^{th} order derivative operators for an isotropic medium (V_P = 3 km/s and V_S = 1.5 km/s) and a VTI medium (V_{P0} = 3 km/s, V_{S0} = 1.5 km/s, ϵ = 0.25, and $\delta = -0.29$). The left column includes isotropic operators, and the right column includes anisotropic operators. From top to bottom are operators with increasing orders of accuracy.

much with the order of accuracy. This indicates that the central parts of the operators are determined by the order of accuracy, while the outer parts are representation of the degree of anisotropy.

Figure 3.4 shows anisotropic derivative operators with same order of accuracy (8^{th} order in space) for three VTI media with different combinations of ϵ and δ. These operators have similar central parts, but different outer parts. This result is consistent with the previous observation that the central part of an operator is determined by the order of accuracy, and the outer part is controlled by the anisotropy parameters.

Figure 3.5(a) shows the influence of approximation to finite difference (2^{nd} and 8^{th} order, Figures 3.3(h) and (b)). The "anisotropic" part ("diagonal tails") is almost the same, and the difference comes from the central part. Figure 3.5(b) shows the difference between operators with different anisotropy (Figures 3.4(a) and (b)). The difference mainly lies in the "tails" of the operators.

Comparison between Figures 3.4(a) and (b) shows that when one a has large difference between ϵ and δ, the operator is big in size and when the difference of ϵ and δ stays the same, the parameter δ affects the operator size. A comparison between Figures 3.4(b) and (c) shows that when the difference between ϵ and δ becomes smaller and δ does not change, the operator get smaller in size. This result is consistent with the polarization equation for VTI media with weak anisotropy (Tsvankin, 2005):

$$\nu_P = \theta + B\left[\delta + 2\left(\epsilon - \delta\right)\sin^2\theta\right]\sin 2\theta\,, \tag{3.10}$$

where

$$B \equiv \frac{1}{2f} = \frac{1}{2\left(1 - V_{S0}^2/V_{P0}^2\right)}.$$

V_{P0} and V_{S0} are P- and S-wave velocities along the symmetry axis, respectively, θ is the phase angle, and ν_p is the P wave polarization angle. This equation demonstrates the deviation of anisotropic polarization vectors from the isotropic ones: the difference of ϵ and δ (which is close to η for weak anisotropy) and the parameter δ control the deviation of ν_P

from θ and, therefore, the size of the anisotropic derivative operators.

3.4.3 Operator truncation

The derivative operators for isotropic and anisotropic media are very different in both shape and size , and the operators vary with the strength of anisotropy. In theory, analytic isotropic derivatives are point operators in the *continuous* limit. If one can do perfect Fourier transform to ik_x and ik_z (without doing the approximations to different orders of accuracy as one does in Figure 3.2), one gets point derivative operators. This is because ik_x is constant in the z direction (see Figure 3.6(a)), whose Fourier transform is delta function; the exact expression of ik_x in the k domain also makes the operator point in the x direction. This makes the isotropic derivative operators point operators in the x and z direction. And when one applies approximations to the operators, they are compact in the space domain.

However, even if one does perfect Fourier transformation to iU_x and iU_z (without doing the approximations for different orders of accuracy) for VTI media, the operators will not be point operators because iU_x and iU_z are not constants in z and x directions, respectively (see Figure 3.6(b)). The x domain operators spread out in all directions (Figures 3.3(b), (d), (f), and (h)).

This effect is illustrated by Figure 3.3. When the order of accuracy decreases, the isotropic operators become more compact (shorter in space), while the anisotropic operators do not get more compact. No matter how one improves the compactness of isotropic operators, one does not get compact *anisotropic* operators in the space domain by the same means.

Because the size of the anisotropic derivative operators is usually large, it is natural that one would truncate the operators to save computation. Figure 3.7 shows a snapshot of an elastic wavefield and corresponding derivative operators for a VTI medium with $\epsilon = 0.25$ and $\delta = -0.29$. Figure 3.8 shows the attempt of separation using truncated operator size of (a) 11×11, (b) 31×31 and (c) 51×51 out of the full operator size 65×65. Figure 3.8 shows

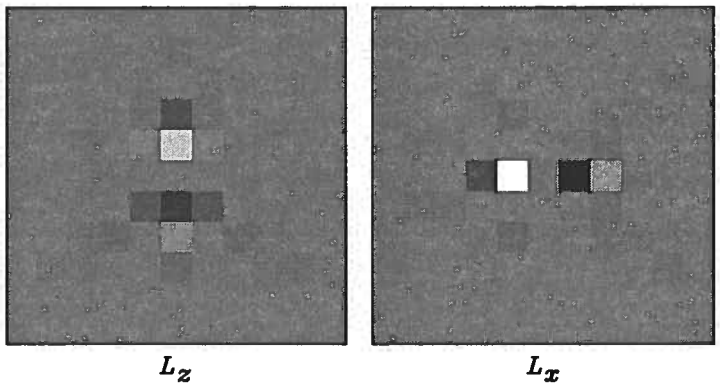

(a)

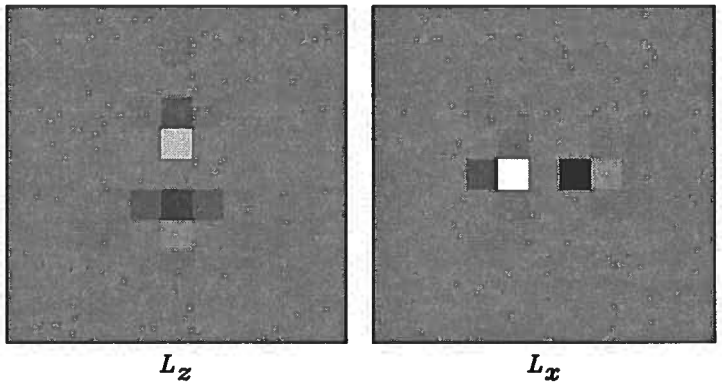

(b)

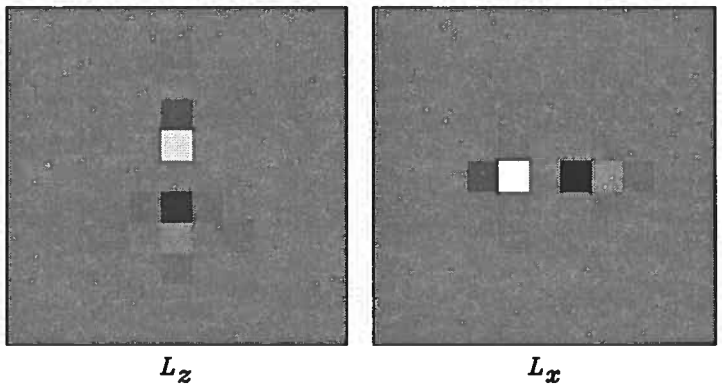

(c)

Figure 3.4. 8^{th} order anisotropic pseudo derivative operators for three VTI media: a) ϵ=0.25, δ=-0.29, b) ϵ=0.54, δ=0, and c) ϵ=0.2, δ=0.

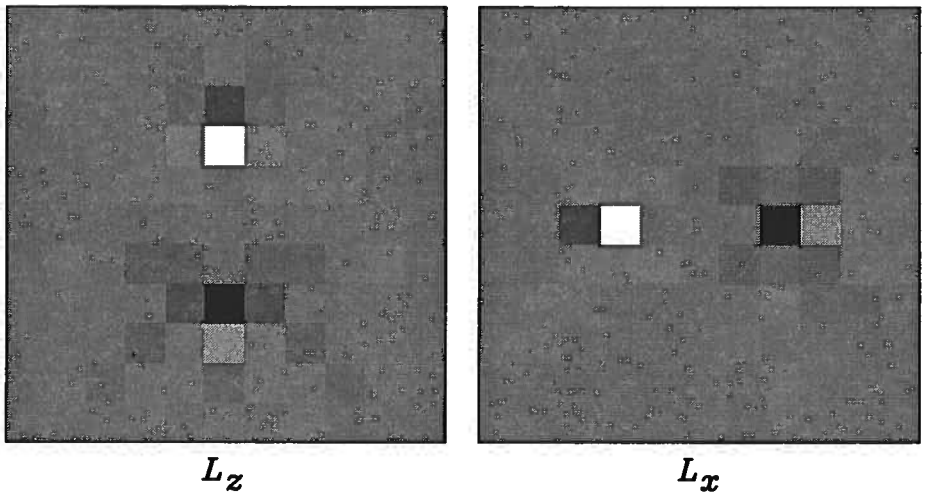

(a)

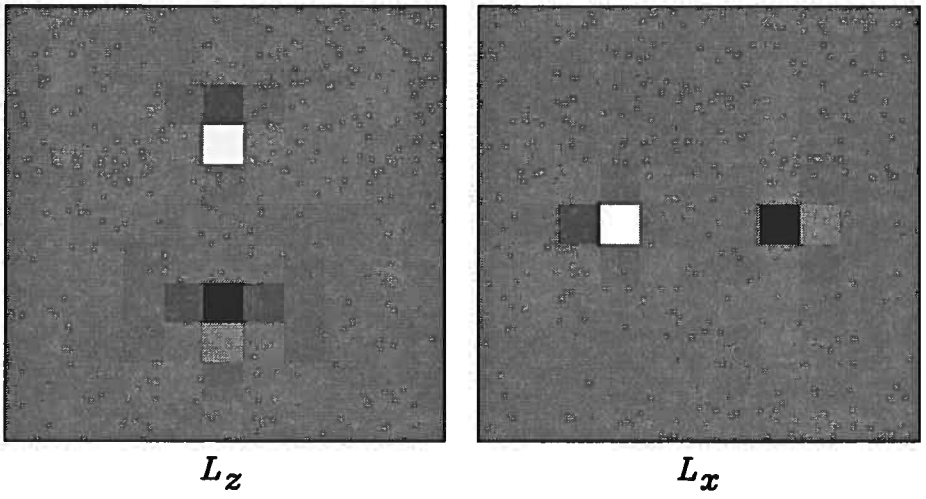

(b)

Figure 3.5. (a) Difference between the 8^{th} and 2^{nd} order operators (Figures 3.3(h) and (b)) in the z and x directions for a VTI medium with anisotropy ϵ=0.25, δ=-0.29. (b) The difference between the 8^{th} order anisotropic operators for a VTI medium with anisotropy ϵ=0.25, δ=-0.29 (Figure 3.4(a)) and a VTI medium with anisotropy ϵ=0.54, δ=0 (Figure 3.4(b)).

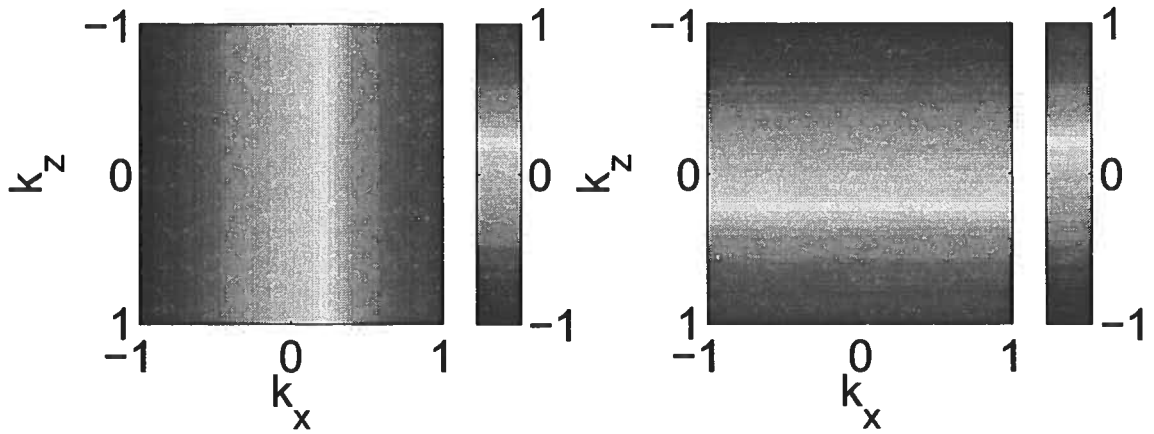

(a)

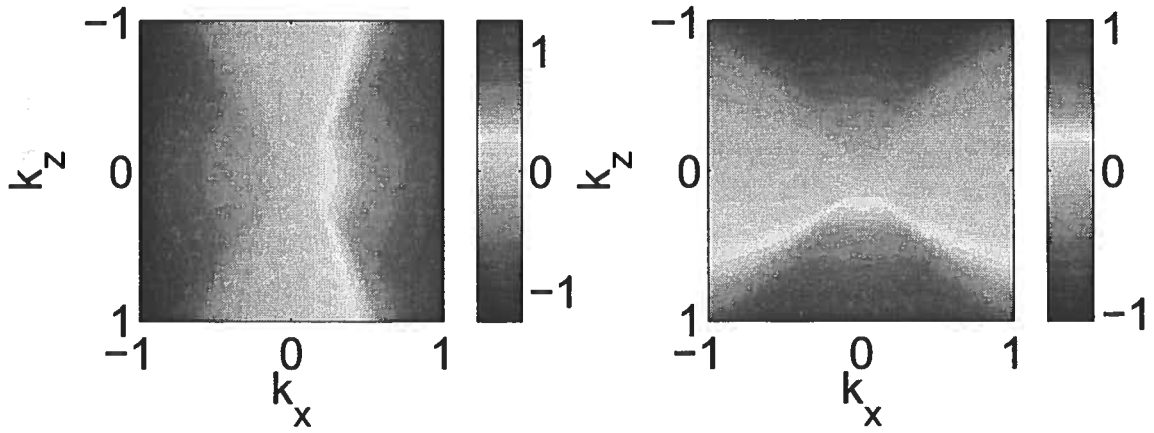

(b)

Figure 3.6. (a) Isotropic and (b) VTI ($\epsilon = 0.25$, $\delta = -0.29$) polarization vectors (Figure 3.2) projected on to the x (left column) and z directions (right column). The isotropic polarization vectors components in the z and x directions depend only on k_z and k_x, respectively. In contrast, the anisotropic polarization vectors components are functions of both k_x and k_z.

that the truncation causes the wave-modes incompletely separated. This is because the truncation changes the directions of the polarization vectors, thus projecting the wavefield displacements onto wrong directions. Figure 3.9 presents the P-wave polarization vectors before and after the truncation. For a truncated operator size of 11×11, the polarization vectors deviate from the correct ones to a maximum of $10°$, but even this difference makes the separation incomplete.

3.5 Examples

I illustrate the anisotropic wave mode separation with a simple synthetic example and a more challenging elastic Sigsbee 2A model (Paffenholz *et al.*, 2002).

3.5.1 Simple model

I consider a 2D isotropic model characterized by the V_P, V_S, and density shown in Figures 3.10(a)–(c). The model contains negative P and S velocity anomalies that cause triplications on the wavefronts. The source is located at the center of the model. Figure 3.11(a) shows the vertical and horizontal components of one snapshot of the simulated elastic wavefield (generated using the 8^{th} order finite difference solution of the elastic wave equation), Figure 3.11(b) shows the separation to P and S modes using divergence and curl operators, and Figure 3.11(c) shows the mode separation obtained using the pseudo operators which are dependent on the medium parameters. A comparison of Figures 3.11(b) and (c) indicates that the divergence and curl operators and the pseudo operators work identically well for this isotropic medium.

I then consider a 2D anisotropic model similar to the previous model shown in Figures 3.10(a)–(c) (with V_P and V_S representing the vertical P and S wave velocities), and additionally characterized by the parameters ϵ and δ shown in Figures 3.10(d) and (e), respectively. The parameters ϵ and δ vary gradually from top to bottom and left to right, respectively. The upper left part of the medium is isotropic and the lower right part is strongly anisotropic. Since the difference between ϵ and δ at the bottom part of the model

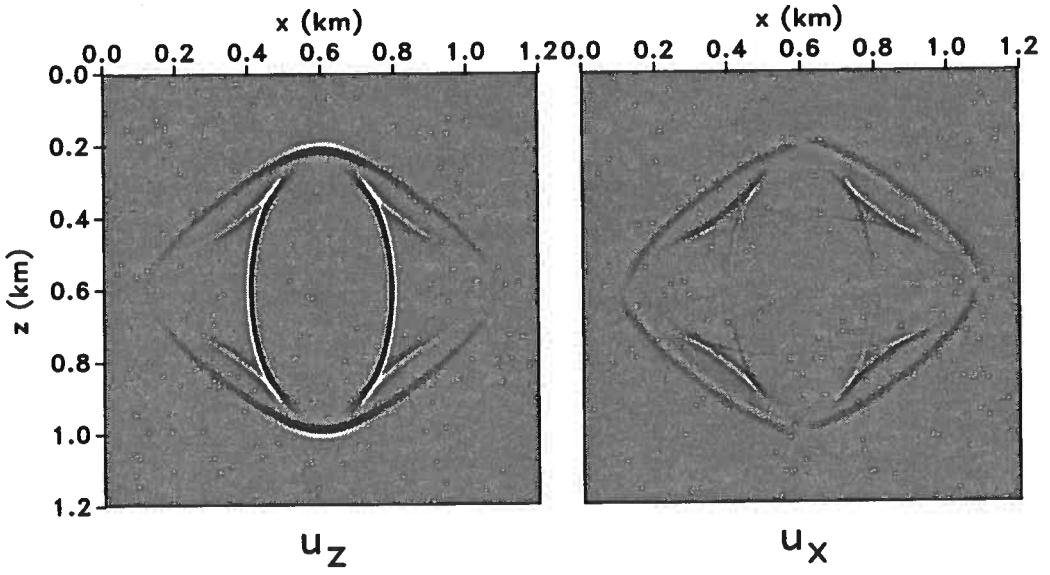

(a)

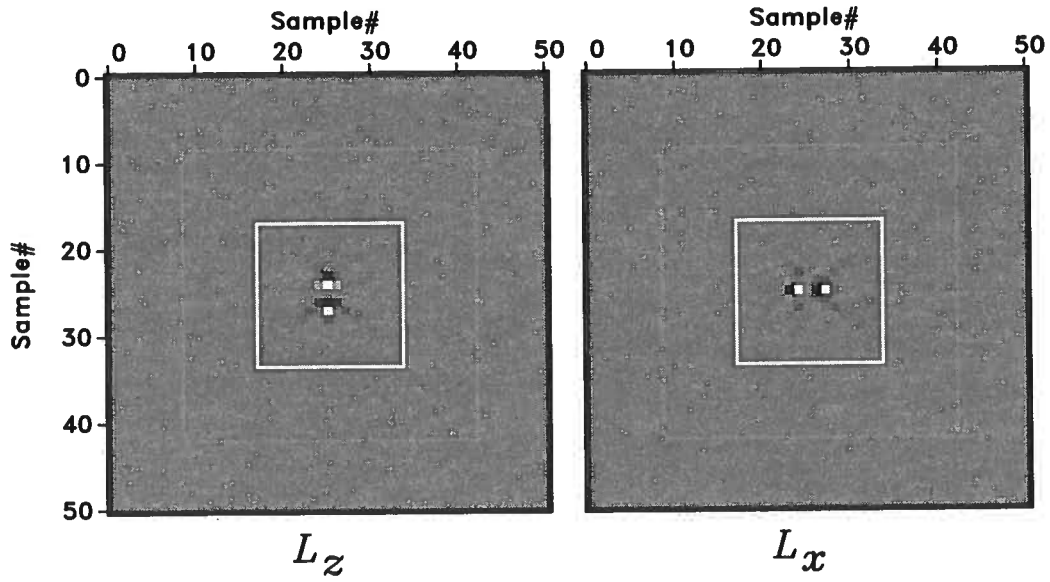

(b)

Figure 3.7. (a) A snapshot of an elastic wavefield showing the vertical (left) and horizontal (right) components for a VTI medium ($\epsilon = 0.25$ and $\delta = -0.29$). (b) 8^{th} order anisotropic pseudo derivative operators in z (left) and x (right) direction for this VTI medium. The boxes show the truncation of the operator to sizes of 11×11, 31×31, and 51×51.

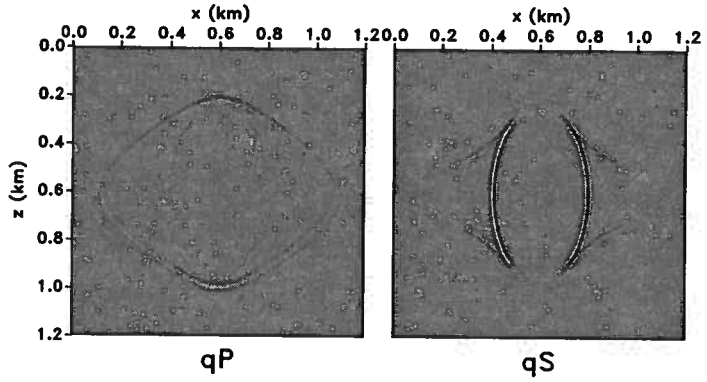

(a)

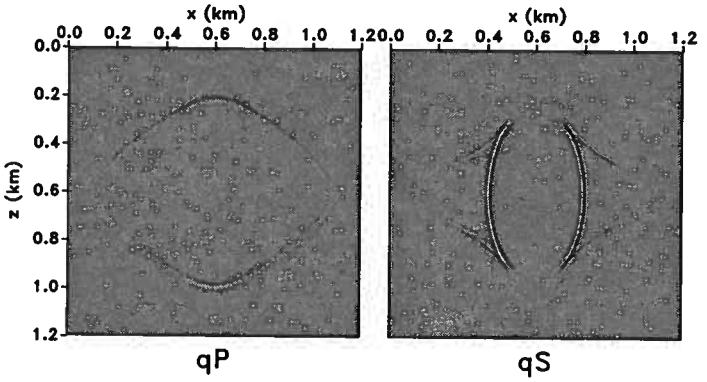

(b)

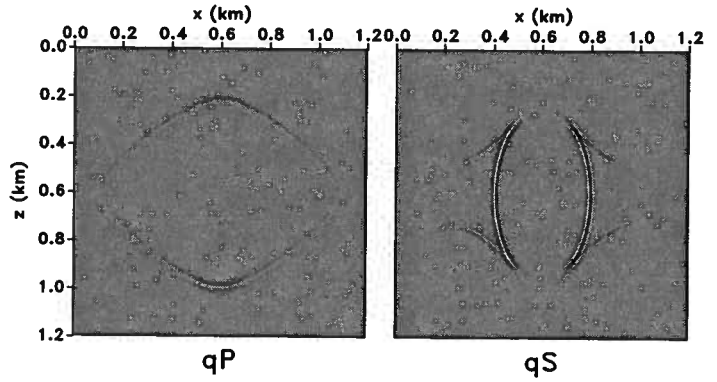

(c)

Figure 3.8. Separation by 8^{th} order anisotropic pseudo derivative operators of different sizes: (a) 11×11, (b) 31×31, (c) 51×51, shown in Figure 3.7(b). The plot shows the larger the size of the operators, the better the separation is.

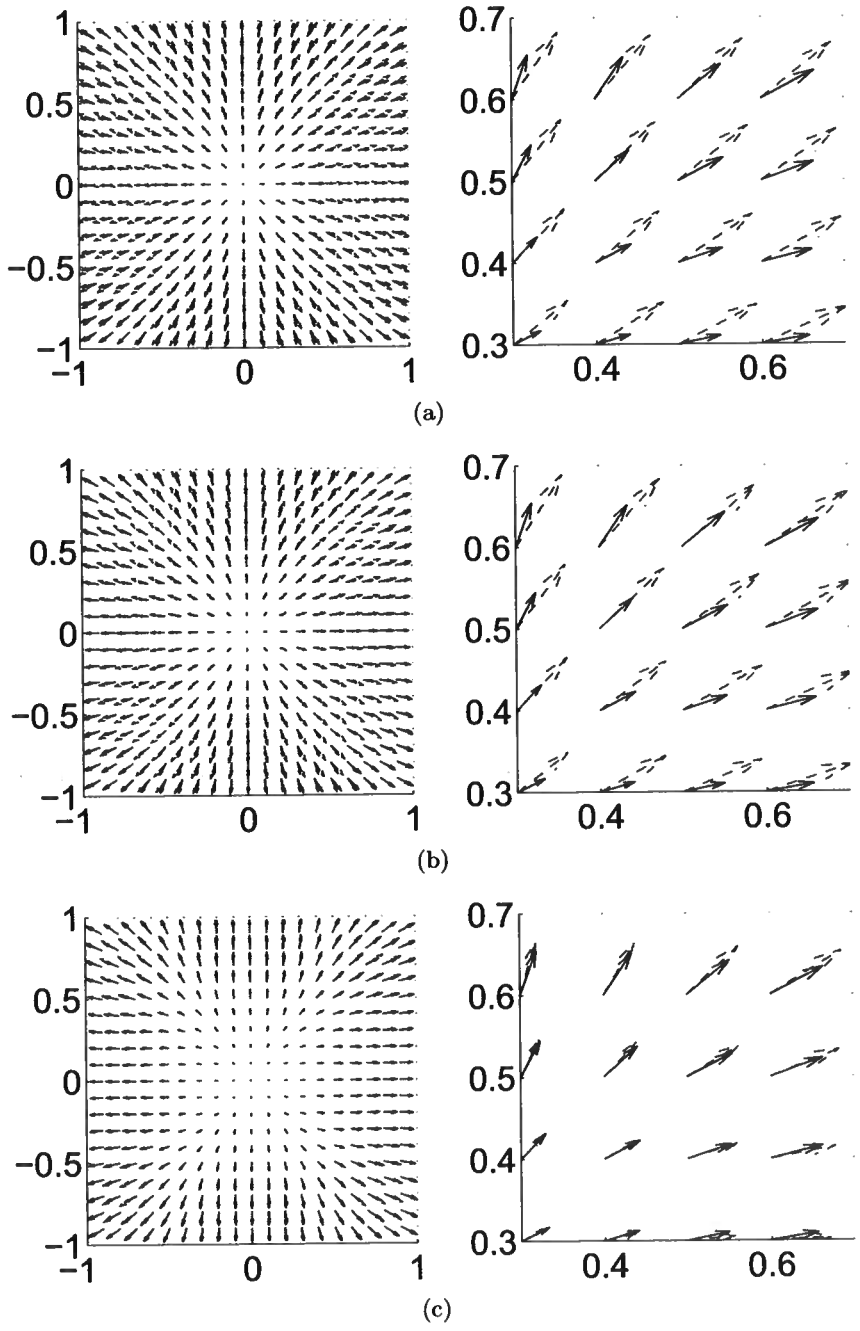

Figure 3.9. Deviation of polarization vectors by truncating the size of the space-domain operator to (a) 11×11, (b) 31×31, (c) 51×51 out of 65×65. The left column shows polarization vectors from -1 to $+1$ cycles in both x and z directions, and the right column zooms to 0.3 to 0.7 cycles. The solid vectors are the exact polarization vectors, and the dashed ones are the effective polarization vectors after truncation of the operator in the x domain.

is large, the S waves in this region are severely triplicated due to this strong anisotropy.

Figure 3.12 illustrates the pseudo derivative operators obtained at different locations in the model defined by the intersections of x coordinates 0.3, 0.6, 0.9 km and z coordinates 0.3, 0.6, 0.9 km. Since the operators correspond to different combination of the parameters ϵ and δ, they have different forms. The isotropic operator at coordinates $x = 0.3$ km and $z = 0.3$ km, shown in Figure 3.12(a), is purely vertical and horizontal, while the anisotropic operators (Figure 3.12(b) to (i)) have "tails" radiating from the center. The operators become larger at locations where the medium is more anisotropic, for example, at coordinates $x = 0.9$ km and $z = 0.9$ km.

Figure 3.13(a) shows the vertical and horizontal components of one snapshot of the simulated elastic anisotropic wavefield, Figure 3.13(b) shows the separation to P and S modes using conventional isotropic divergence and curl operators, and Figure 3.13(c) shows the mode separation obtained using the pseudo operators constructed using the local medium parameters. A comparison of Figure 3.13(b) and 3.13(c) indicates that the spatially-varying derivative operators successfully separate the elastic wavefields into P and S modes, while the divergence and curl operators only work in the isotropic region of the model.

3.5.2 Sigsbee model

The second model (Figure 3.14) uses an elastic anisotropic version of the Sigsbee 2A model (Paffenholz *et al.*, 2002). In the modified model, V_{P0} is taken from the original model, the V_{P0}/V_{S0} ratio ranges from 1.5 to 2, the parameter ϵ ranges from 0 to 0.48 (Figure 3.14(d)) and the parameter δ ranges 0 from to 0.10 (Figure 3.14(e)). The model is isotropic in the salt and the top part of the model. A vertical point force source is located at coordinates $x = 14.5$ km and $z = 5.3$ km to simulate the elastic anisotropic wavefield.

Figure 3.15 shows one snapshot of the simulated elastic anisotropic wavefields using the model shown in Figure 3.14. Figure 3.16 illustrates the separation of the anisotropic elastic wavefields using the divergence and curl operators, and Figure 3.17 illustrates the separation

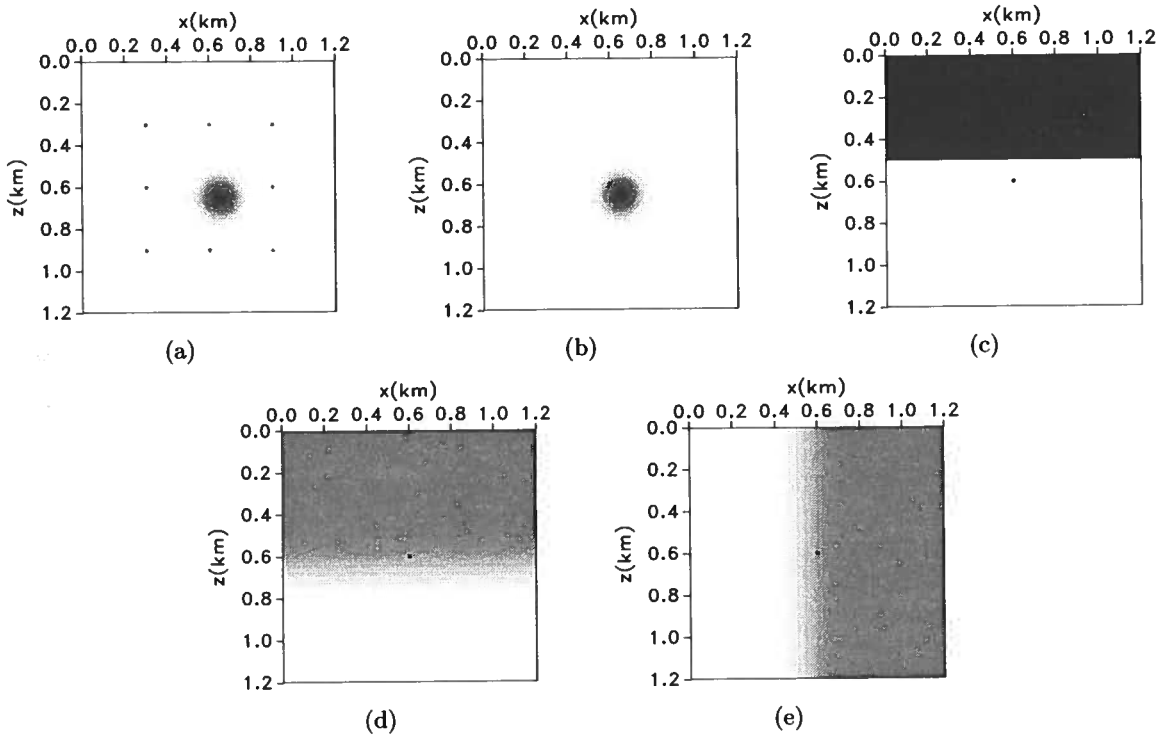

Figure 3.10. 1.2 km× 1.2 km model with parameters (a) $V_{p0} = 3$ km/s except for a low velocity Gaussian anomaly around $x = 0.65$ km and $z = 0.65$ km, (b) $V_{S0} = 1.5$ km/s except for a low velocity Gaussian anomaly around $x = 0.65$ km and $z = 0.65$ km, (c) $\rho = 1.0$ g/cm^3 in the top layer and 2.0 g/cm^3 in the bottom layer, (d) ϵ smoothly varying from 0 to 0.25 from top to bottom, (e) δ smoothly varying from 0 to -0.29 from left to right. A vertical point force source is located at $x = 0.6$ km and $z = 0.6$ km shown by the dot in panels (b), (c), (d), and (e). The dots in panel (a) correspond to the locations of the anisotropic operators shown in Figure 3.12 .

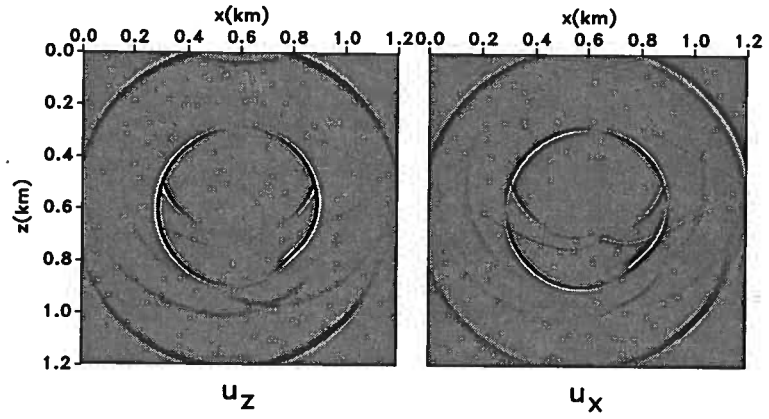

(a)

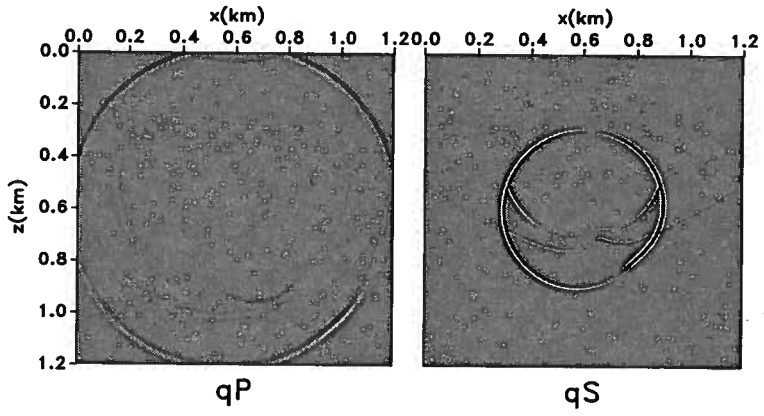

(b)

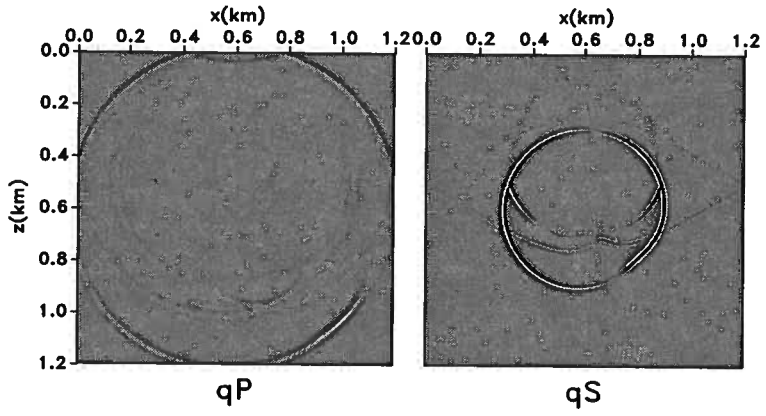

(c)

Figure 3.11. (a) One snapshot of the isotropic wavefield modeled with a vertical point force source at x=0.6 km and z=0.6 km for the model shown in Figure 3.10, (b) isotropic P and S wave modes separated using divergence and curl operators, and (c) isotropic P and S wave modes separated using pseudo derivative operators. Both (b) and (c) show good separation results.

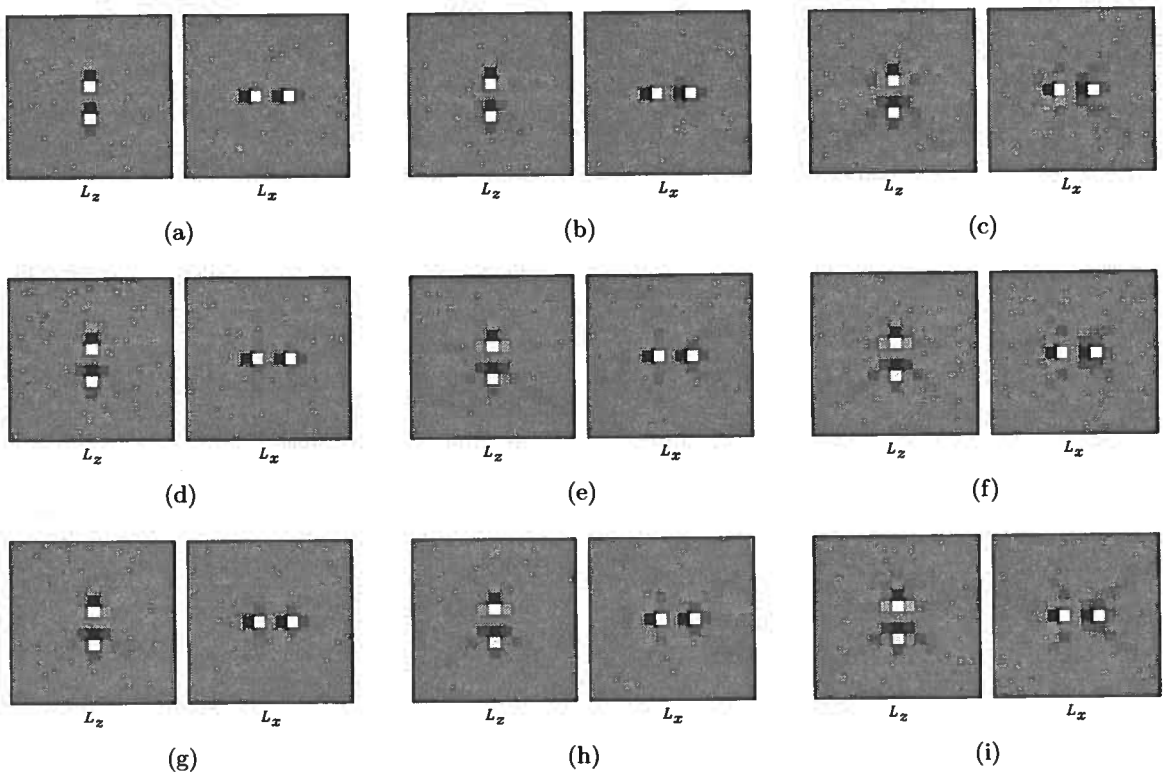

Figure 3.12. 8^{th} order anisotropic pseudo derivative operators in the z and x directions at the intersections of x=0.3, 0.6, 0.9 km and z=0.3, 0.6, 0.9 km for the model shown in Figure 3.10.

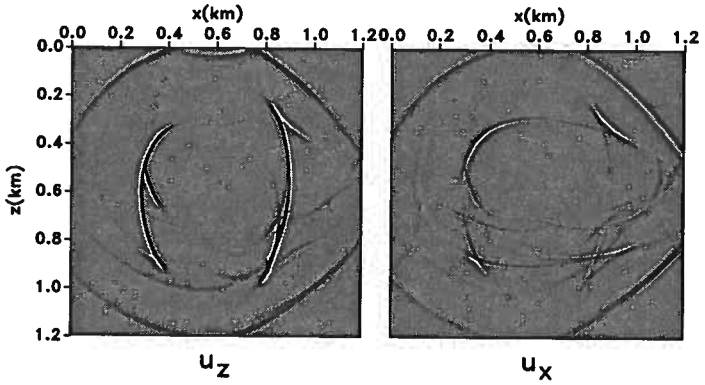

(a)

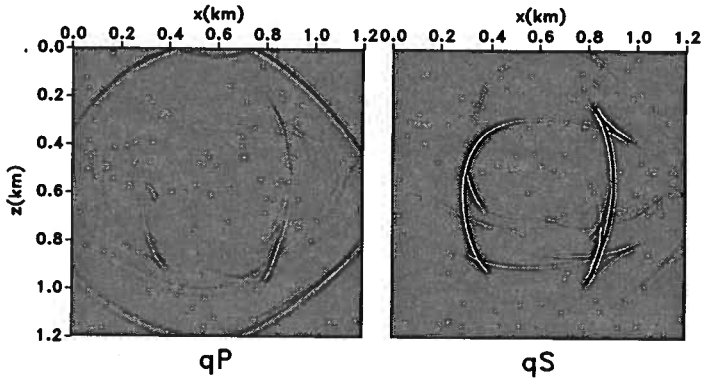

(b)

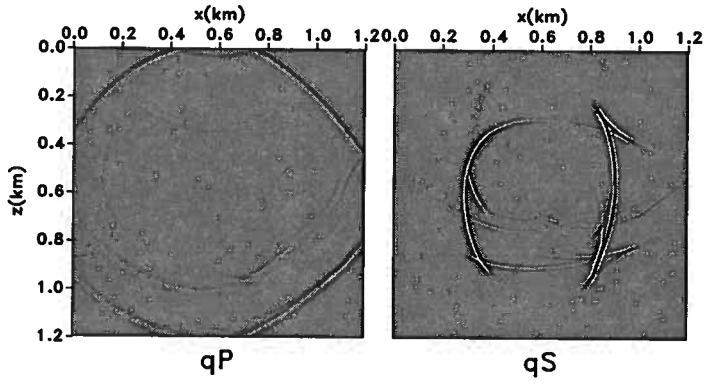

(c)

Figure 3.13. (a) One snapshot of the anisotropic wavefield modeled with a vertical point force source at x=0.6 km and z=0.6 km for the model shown in Figure 3.10, (b) anisotropic P and S modes separated using divergence and curl operators, and (c) anisotropic P and S modes separated using pseudo derivative operators. The separation of wavefields into P and S modes in (b) is not complete, which is obvious at places such as at coordinates $x = 0.4$ km $z = 0.9$ km. In contrast, the separation in (c) is much better, because the correct anisotropic derivative operators are used..

using my pseudo derivative operators. Figure 3.16 shows the residual of unseparated P and S wave modes, such as at coordinates $x = 13$ km and $z = 7$ km in the P panel and at $x = 11$ km and $z = 7$ km in the S panel. The residual of S waves in the P panel of Figure 3.16 is very significant because of strong reflections from the salt bottom. This extensive residual can be harmful to under-salt elastic or even acoustic migration, if not removed completely. In contrast, Figure 3.17 shows the P and S modes better separated, demonstrating the effectiveness of the anisotropic pseudo derivative operators constructed using the local medium parameters. These wavefields composed of well separated P and S modes are essential for producing clean seismic images.

In order to test the separation with spatially invariant anisotropy in the model, I show in Figure 3.18 the separation with $\epsilon = 0.3$ and $\delta = 0.1$ in the k domain. This separation assumes a model with homogeneous anisotropy. The separation shows that there is still residual in the separated panels. Although the residual is much weaker compared to separating using an isotropic model, it is still visible at locations such as at coordinates $x = 13$ km and $z = 7$ km, and $x = 13$ km and $z = 4$ km in the P panel and at $x = 16$ km and $z = 2.5$ km in the S panel.

3.6 Discussion

The separation of P and S wave-modes is based on the projection of elastic wavefields onto their respective polarization vectors. For VTI media, P and S mode polarization vectors can be conveniently obtained by solving the Christoffel equation. The Christoffel equation is a plane-wave solution to the elastic wave equation. Since the displacements, velocity and acceleration field have the same form of elastic wave equation, the separation algorithm applies to all these wavefields. The P and SV mode separation can be extended to TTI (transverse isotropic with a tilted symmetry axis) media by solving a TTI Christoffel matrix, and obtain TTI separators. Physically, the TTI media is just a rotation of VTI media. This extension will be presented in Chapter 4.

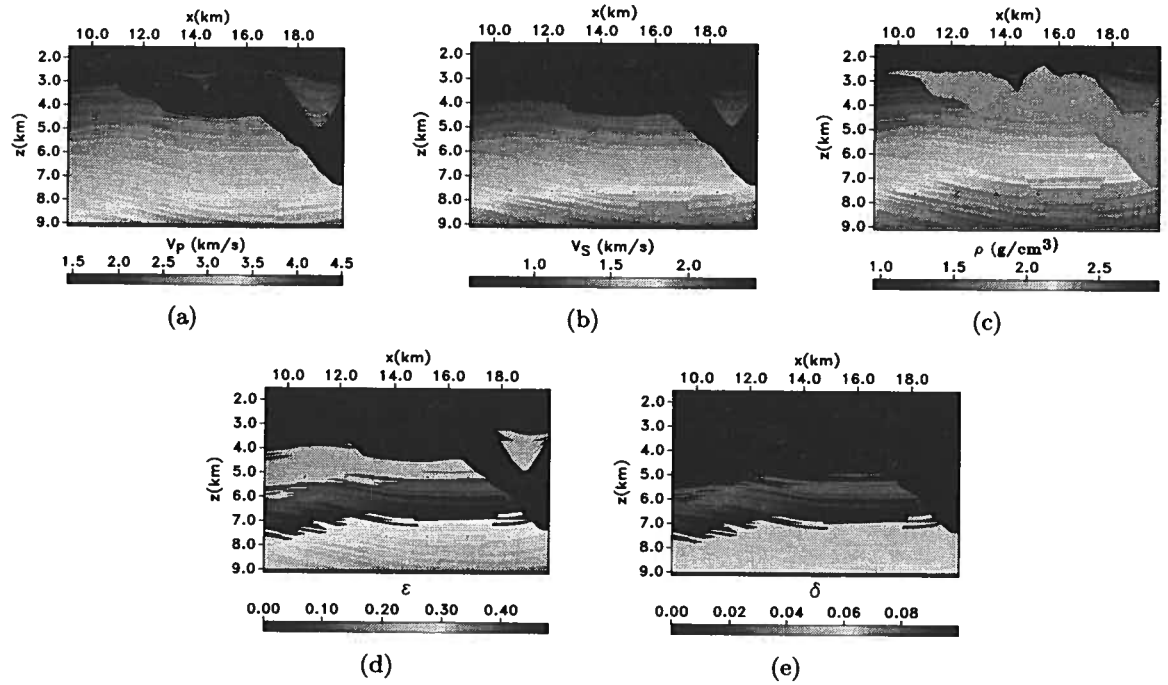

Figure 3.14. Sigsbee 2A model in which (a) is the P wave velocity (taken from the original Sigsbee 2A model (Paffenholz *et al.*, 2002)), (b) is the S wave velocity, where V_{P0}/V_{S0} ratio ranges from 1.5 to 2.0, (c) is the density ranging from 1.0 g/cm^3 to 2.2 g/cm^3, (d) is the parameter ϵ ranging from 0.20 to 0.48, and (e) is the parameter δ ranging from 0 to 0.10 in the rest of the model.

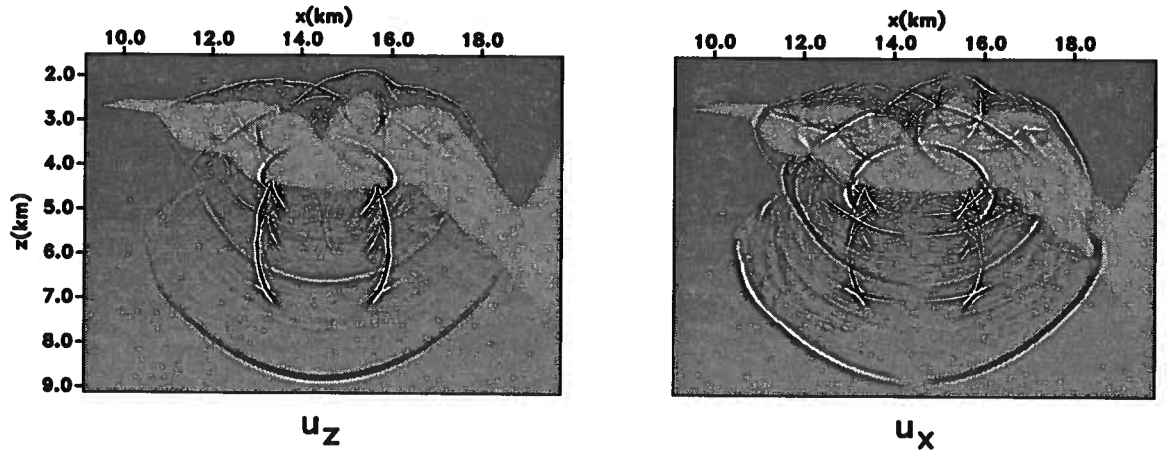

Figure 3.15. Anisotropic wavefield modeled with a vertical point force source at $x = 14.3$ km and $z = 5.3$ km for the model shown in Figure 3.14.

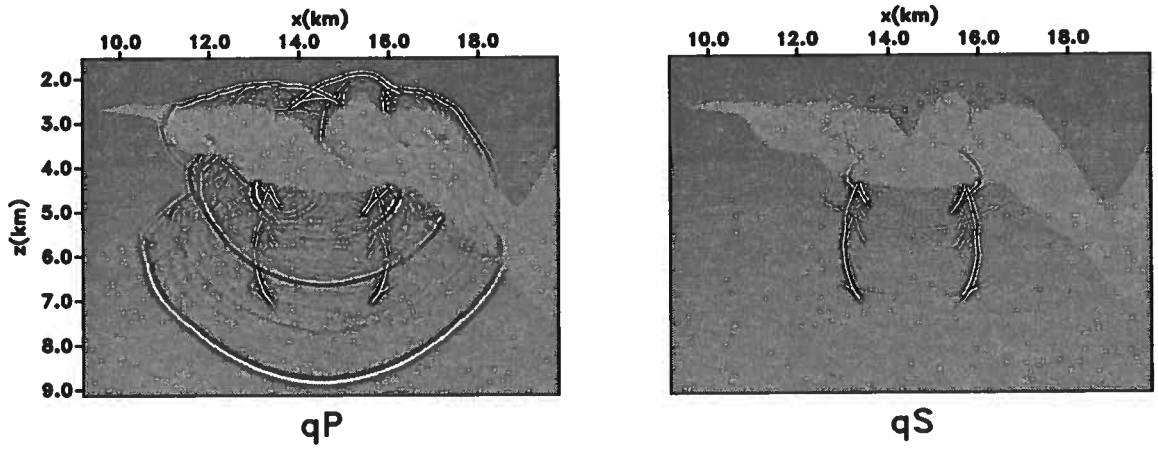

Figure 3.16. Anisotropic P and S modes separated using divergence and curl operators for the vertical and horizontal components of the elastic wavefields shown in Figure 3.15. Residuals are obvious at places such as at coordinates $x = 13$ km and $z = 7$ km in the P panel and at $x = 11$ km and $z = 7$ km in the S panel.

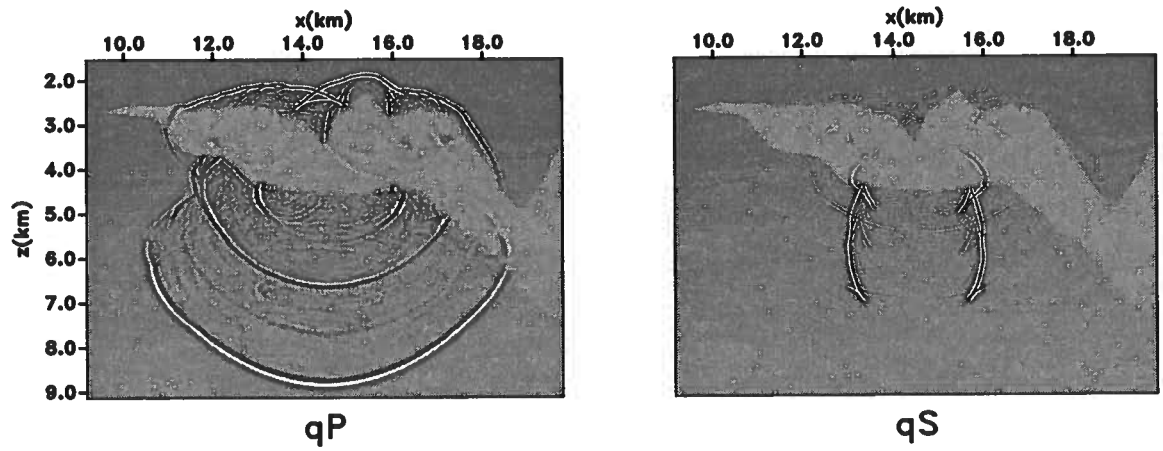

Figure 3.17. Anisotropic P and S modes separated using pseudo derivative operators for the vertical and horizontal components of the elastic wavefields shown in Figure 3.15. They show better separation of P and S modes.

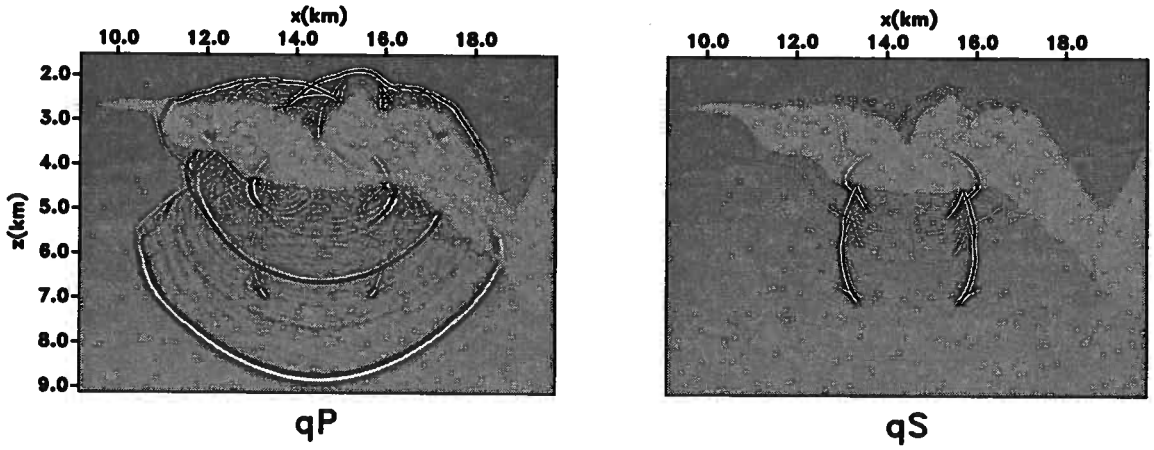

Figure 3.18. Anisotropic P and S modes separated in the k domain for the vertical and horizontal components of the elastic wavefields shown in Figure 3.15. The separation assumes $\epsilon = 0.3$ and $\delta = 0.1$ throughout the model. The separation is incomplete. Residuals are still visible at places such at coordinates $x = 13$ km and $z = 7$ km, and $x = 13$ km and $z = 4$ km in the P panel and at $x = 16$ km and $z = 2.5$ km in the S panel.

Suppose that in a 2D seismic survey for an area characterized by VTI anisotropy, the survey line is along the dip of the structure. In this vertical symmetry plane of the VTI media, SV and SH waves are uncoupled most of the time, where SH wave is polarized out of plane. One only needs to decompose P and SV modes in the vertical plane. The plane wave solution is sufficient for most TI media, except for a special case where there exists a singularity point at an oblique propagation angle in the vertical plane (a line singularity in 3D), at which angle SV and SH wave velocities coincide. At this point, the SV wave polarization is not uniquely defined by Christoffel equation. S waves at the singularity are polarized in a plane orthogonal to the P wave polarization vector. However, this is not a problem since we define SV waves polarized in vertical planes only, therefore I remove the singularity by using the cylindrical coordinates. The situation is more complicated in S-wave coupling in orthorhombic media, where there is at least one singularity per quadrant. As pointed out by Dellinger & Etgen (1990), the singularity in orthorhombic media is a global property of the media and cannot be removed, therefore the separation using polarization

vectors in 3D orthorhombic media is not straightforward.

The anisotropic derivative operators depend on the medium parameters. In Figure 3.19, I show how sensitive the separation is to the medium parameters. One elastic wavefield snapshot is shown in Figure 3.7(a) for a VTI medium with $V_{P0}/V_{S0} = 2$ and $\epsilon = 0.25$, $\delta = -0.29$. I try to separate the P and SV modes with (a) $\epsilon = 0.4$, $\delta = -0.1$, (b) $\epsilon = 0$, $\delta = -0.3$ and (c) $\epsilon = 0$, $\delta = 0$. The results shows that parameters (a) help achieve good separation, showing that the accuracy in ϵ and δ is important. The worst-case scenario is shown by parameters (c), where isotropy is assumed for this VTI medium.

3.7 Conclusions

I present a method for obtaining spatially-varying pseudo-derivative operators with application to wave mode separation in anisotropic media. The main idea is to utilize polarization vectors constructed in the wavenumber domain using the local medium parameters and then transform these vectors back to the space domain. The main advantage of applying the pseudo derivative operators in the space domain constructed in this way is that they are suitable for heterogeneous media. The wave-mode separators obtained using this method are spatially-variable filtering operators, which can be used to separate wavefields in VTI media with arbitrary strength of anisotropy. This methodology is applicable for elastic RTM in heterogeneous anisotropic media.

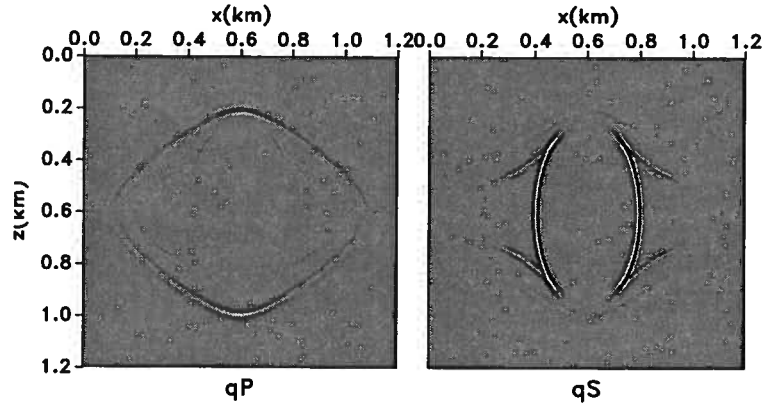

(a)

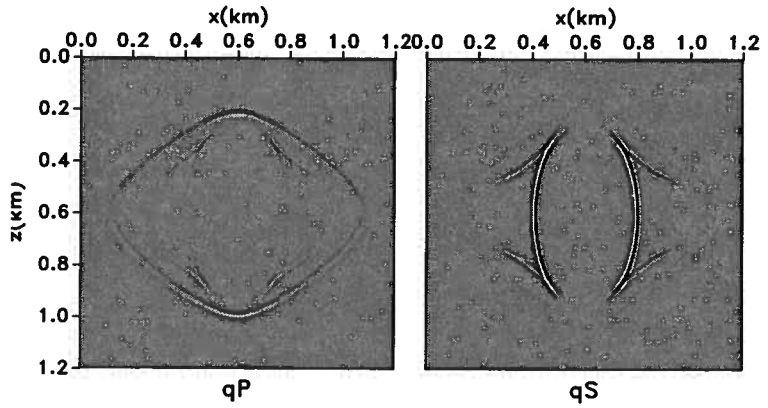

(b)

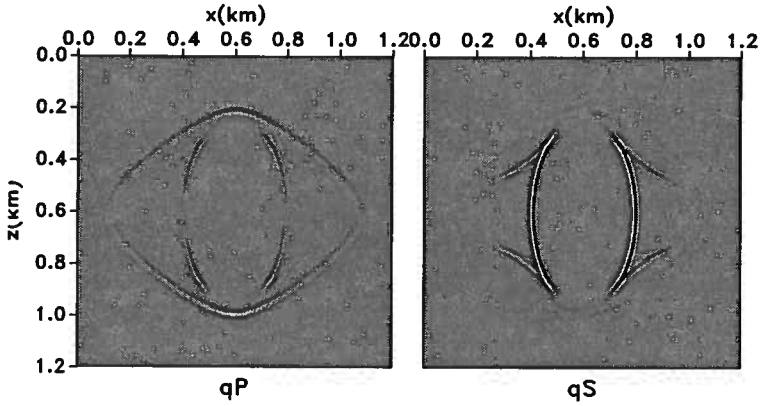

(c)

Figure 3.19. P and SV wave mode separation for a snapshot shown in Figure 3.7(a). The true medium parameters are $\epsilon = 0.25$, $\delta = -0.29$. The separation assumes medium parameters of (a)$\epsilon = 0.4$, $\delta = -0.1$, (b) $\epsilon = 0$, $\delta = -0.3$, and (c)$\epsilon = 0$, $\delta = 0$. Hard clipping was applied to show the weak events. The plot shows that different estimate of anisotropy parameters has influence on the the wave mode separation.

Chapter 4

Elastic wave-mode separation for TTI media

4.1 Summary

Seismic imaging in areas characterized by complex geology requires techniques based on accurate reconstruction of the seismic wavefields. A crucial component of the methods in this category, collectively known as wave-equation migration, is the imaging condition which extracts information about the discontinuities of physical properties from the reconstructed wavefields at every location in space. Conventional acoustic migration techniques image a scalar wavefield representing P waves, in contrast to elastic migration techniques, which image a vector wavefield representing both the P- and S-waves. For elastic imaging, it is desirable that the reconstructed vector fields are decomposed into pure wave-modes, such that the imaging condition produces interpretable images, characterizing, for example, PP or PS reflectivity. In Chapter 3, I show that, in symmetry planes of VTI (transversely isotropic with a vertical symmetry axis) media, wave-mode separation can be achieved by projection of the reconstructed vector fields on the polarization vectors characterizing various wave modes. For heterogeneous media, the polarization directions change with position, therefore wave-mode separation needs to be implemented using space-domain filters. For transversely isotropic media with a tilted symmetry axis (TTI), the polarization vectors depend on the elastic material parameters, including the tilt angle. Using these parameters, I separate the wave-modes by constructing nine filters corresponding to the nine Cartesian components of the three polarization directions at every grid point. Since the S polarization vectors in TI media are not defined in the singular directions, e.g. along the symmetry axis, I construct these vectors by exploiting the orthogonality between the SV and SH polarization vectors,

as well as their orthogonality to the P polarization vector. This procedure allows one to separate all three modes, with better preserved P-wave amplitudes than S-wave amplitudes. Realistic synthetic examples show that this wave-mode separation is effective for both 2D and 3D models with strong heterogeneity and anisotropy.

4.2 Introduction

Acoustic migration is currently the most common procedure for seismic imaging; imaging with multicomponent data has been recognized to benefit lithology discrimination, parameter estimation, and reservoir characterization (Stewart *et al.*, 2003b). In Chapter 2, I investigate elastic imaging by using pure modes, which requires a mode-separation before application of an imaging condition. Chapter 3 illustrates P- and SV-wave mode separation in the symmetry planes of VTI media. The mode separation in heterogeneous VTI media is implemented as non-stationary filtering the wavefields with spatially varying separators in the space domain. Synthetic examples indicate that separation is effective even for complex geology with high heterogeneity.

However, VTI models are suitable only for limited geological settings with horizontal layering. Many case studies have shown that TTI (transversely isotropic with a tilted symmetry axis) models better represent complex geologies like thrusts and fold belts, e.g., the Canadian Foothills (Godfrey, 1991). Using the VTI assumption to image structures characterized by TTI anisotropy introduces both kinematic and dynamical errors in migrated images. For example, Vestrum *et al.* (1999), Isaac & Lawyer (1999), and Behera & Tsvankin (2009) show that seismic structures can be mispositioned if isotropy, or even VTI, is assumed when the medium above the imaging targets is TTI. To carry out elastic wave-equation migration for TTI models and apply the imaging condition that crosscorrelates the separated wave-modes, the wave-mode separation algorithm needs to be adapted to TTI media. For sedimentary layers bent under geological forces, TTI migration models usually incorporate locally varying tilts, and for simplicity, the local symmetry axes are usually assumed to be

orthogonal to the reflectors throughout the model (Charles *et al.*, 2008; Alkhalifah & Sava, 2010). Therefore, in complex TI models, both the local anisotropy parameters ϵ and δ, and the local symmetry axes with tilt ν and azimuth α can be space-dependent.

Wave-mode separation technique by projecting the vector wavefields onto polarization vectors has been applied only to P- and SV-mode separation for 2D wavefields (Dellinger, 1991) and to P-mode separation for 3D wavefields (Dellinger, 1991) in *homogeneous* VTI media. In Chapter 3, I extend P- and SV-mode separation to *heterogeneous* VTI media. For 3D models, the main challenge resides in the fact that fast and slow shear modes have complicated polarizations around symmetry-axis propagation directions. It is possible to apply the 2D separation method to 3D TTI models using the following procedure. First, project the elastic wavefields onto symmetry-axis planes (which contains P- and SV-modes) and isotropy plane (which contain the SH-mode only); then separate P- and SV-modes in the symmetry-axis planes using divergence and curl operators for isotropic media or polarization vector projection for TI media. However, this approach is difficult in practice as wavefields are usually constructed in Cartesian coordinates and symmetry-axis planes of the models are not aligned with the Cartesian coordinates. Furthermore, for heterogeneous models, the symmetry-axis planes change spatially, which makes projection of wavefields onto symmetry-axis planes impossible. To avoid these problems, I propose a simpler and more straightforward solution to separate wave-modes with 3D operators, which eliminates the need for projecting the wavefields onto symmetry-axis planes. The new approach constructs shear-wave filters by exploiting the mutual orthogonality of shear modes with the P mode, whose polarization vectors are computed by solving 3D Christoffel equations.

In this chapter, I extend mode separation to symmetry-axis planes of TTI media and generalize the algorithm to 3D TI media. Then, I demonstrate wave-mode separation in 2D with examples for homogeneous and heterogeneous media and separation in 3D with an example for homogeneous TTI media.

4.3 Wave-mode separation for 2D TI media

In Chapter 3, I show mode separation for symmetry-axis planes of VTI media. The separation algorithm for TTI models is similar to the approach used for VTI models. The main difference is that for VTI media, the wavefields consist of P- and SV-modes, and equations 3.6 and 3.7 can be used for separation in all vertical planes of a VTI medium. However, for TTI media, this separation only works in the plane containing the normal to the reflector, where P- and SV-waves are polarized, while other vertical planes contain SH-waves as well. Note that the "SH-wave" is a term which is originally used in isotropic media to refer to a shear-wave polarized horizontally and perpendicular to the 2D reflection plane, in which P-wave is polarized. I use the term "SH-wave" in TI media as a shear-mode that is polarized perpendicular to the symmetry-axis plane. The SH-wave in TI media is not necessarily horizontal (Figure 4.6).

To obtain the polarization vectors for P and S modes in the symmetry planes of TTI media, one needs to solve for the Christoffel equation 3.8 with

$$G_{11} = c_{11}n_x^2 + 2c_{15}n_xn_z + c_{55}n_z^2, \tag{4.1}$$

$$G_{12} = c_{15}n_x^2 + (c_{13} + c_{55})\, n_xn_z + c_{35}n_z^2, \tag{4.2}$$

$$G_{22} = c_{55}n_x^2 + 2c_{35}n_xn_z + c_{33}n_z^2. \tag{4.3}$$

Here, since the symmetry axis of the TTI medium is not aligned with the vertical axis k_z, the TTI Christoffel matrix is different from its VTI equivalent. The stiffness tensor is determined by the parameters V_{P0}, V_{S0} , ϵ, δ, and the tilt angle ν.

In anisotropic media, $\mathbf{U}_P$ generally deviates from the wave vector direction $\mathbf{k} = \frac{\omega}{V}\mathbf{n}$, where ω is the angular frequency, V is the phase vector. Figures 4.5(a) and (b) show the P-mode polarization in the wavenumber domain for a VTI medium and a TTI medium with a 30° tilt angle, respectively. The polarization vectors for the VTI medium deviate from radial directions, which represent the isotropic polarization vectors $\mathbf{k}$. The polarization

vectors of the TTI medium are rotated 30° about the origin from the vectors of the VTI medium.

Figures 4.1(a) and (b) show the components of the P-wave polarization vectors for a VTI medium and a TTI medium with a 30° tilt angle, respectively. Figure 4.1(c) shows that the polarization vectors in Figure 4.1(b) rotated to the symmetry axis and its orthogonal direction of the TTI medium. Comparing Figures 4.1(a) and (c), we see that within the circle that has a radius of π radians, the components of this TTI medium are rotated 30° from those of the VTI medium. However, note that the z and x components of the polarization vectors for the VTI medium (Figure 4.1(a)) are symmetric with respect to the x and z axes, respectively; in contrast, the vectors of the TTI medium (Figure 4.1(c)) are not symmetric because the the TTI symmetry axis is not aligned with the z-axis of the Cartesian system.

To maintain continuity at the negative and positive Nyquist wavenumbers for Fourier transform to obtain space-domain filters, i.e. at $k_x, k_z = \pm\pi$ radians, one needs to apply tapers to the vector components. For VTI media, a taper corresponding to the function (Appendix A)

$$f(k) = -\frac{8\sin(k)}{5k} + \frac{2\sin(2k)}{5k} - \frac{8\sin(3k)}{105k} + \frac{\sin(4k)}{140k} \tag{4.4}$$

can be applied to the x and z components of the polarization vectors (Figure 4.1(a)), where k represent the components k_x and k_z of the vector $\mathbf{k}$. This taper ensures that U_x and U_z are zero at $k_z = \pm\pi$ radians and $k_x = \pm\pi$ radians, respectively. The components U_x and U_z are continuous in the z and x directions across the Nyquist wave numbers, respectively, due to the symmetry of the VTI media. Moreover, the application of this taper transforms polarization vector components to 8^{th} order derivatives. If the components of the isotropic polarization vectors $\mathbf{k}$ are tapered by the function in equation 4.4 and then transformed to the space domain, one obtains the conventional 8^{th} order finite difference derivative operators $\frac{\partial}{\partial x}$ and $\frac{\partial}{\partial z}$ (Appendix A). Therefore, the VTI separators reduce to conventional derivatives—the components of the divergence and curl operators—when the medium is

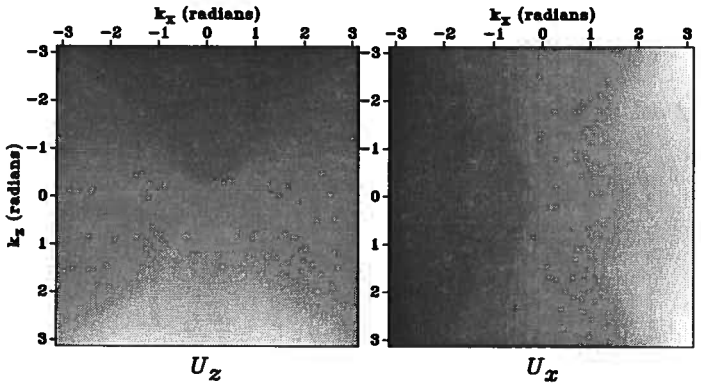

(a)

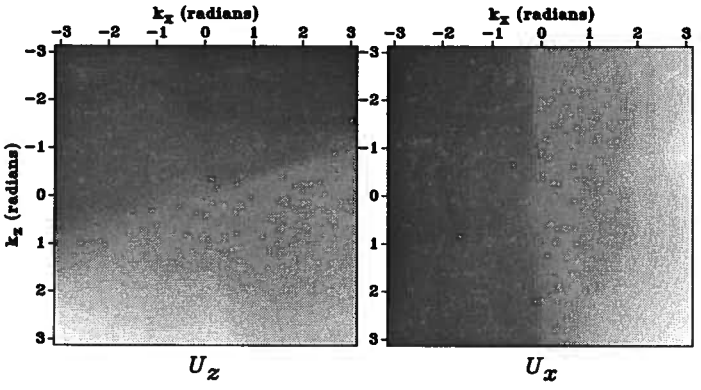

(b)

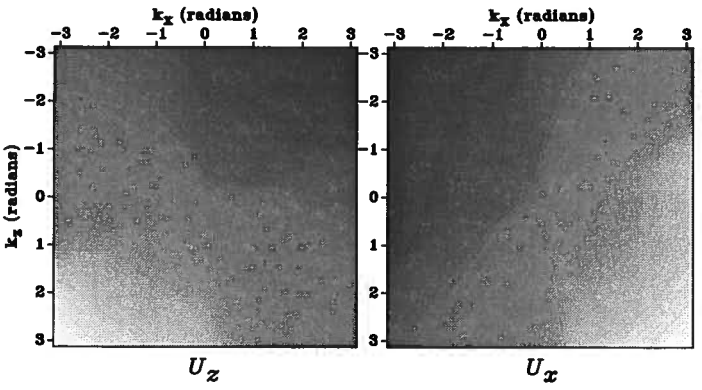

(c)

Figure 4.1. Z and x components of the polarization vectors for P-mode in the Fourier domain for (a) a VTI medium with $\epsilon = 0.25$ and $\delta = -0.29$, and for (b) a TTI medium with $\epsilon = 0.25$, $\delta = -0.29$, and $\nu = 30°$. Panel (c) represents the projection of the polarization vectors shown in (b) onto the tilt axis and its orthogonal direction.

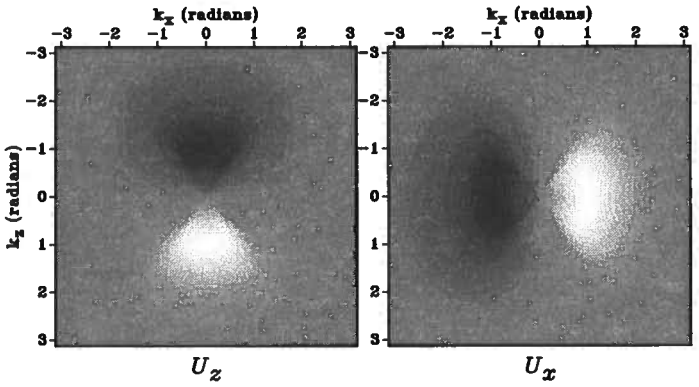

(a)

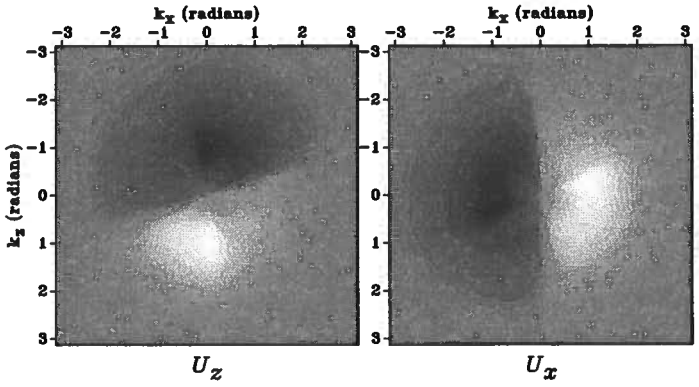

(b)

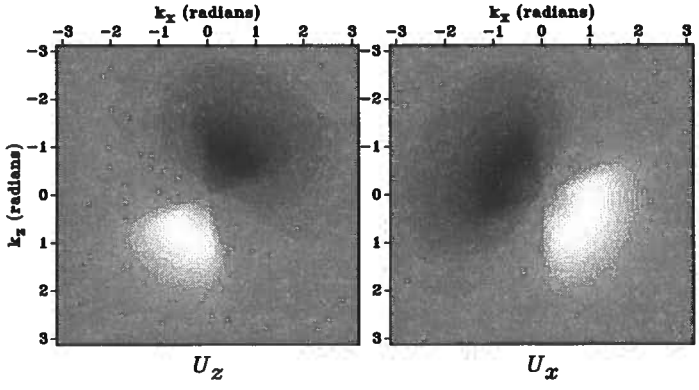

(c)

Figure 4.2. Wavenumber-domain vectors in Figure 4.1 are tapered by the function in equation 4.5 to avoid Nyquist discontinuity. Panel (a) corresponds to Figure 4.1(a), panel (b) corresponds to Figure 4.1(b), and panel (c) corresponds to Figure 4.1(c).

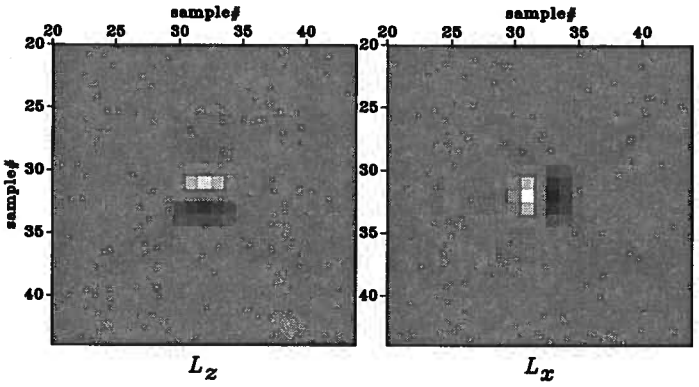

(a)

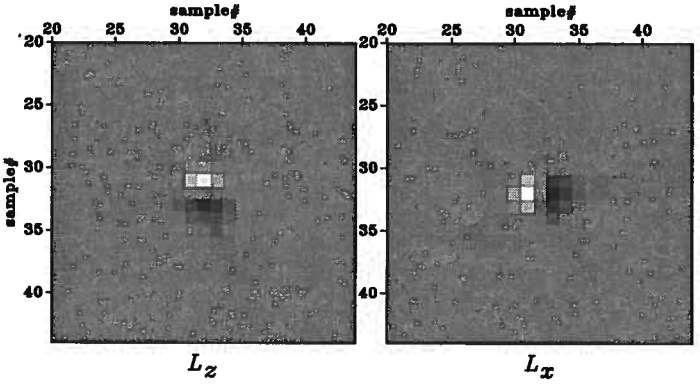

(b)

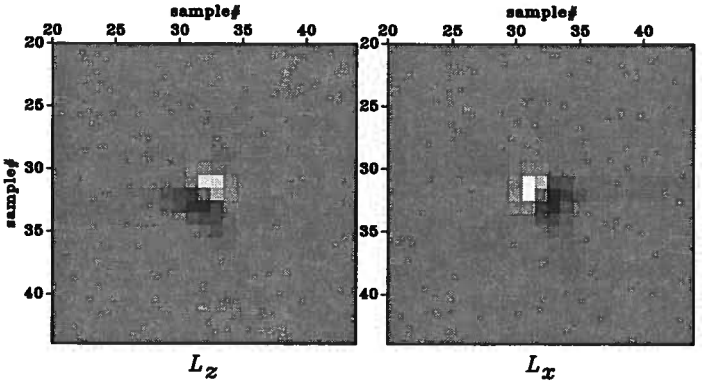

(c)

Figure 4.3. Space-domain wave-mode separators for the medium shown in Figure 4.5. They are the Fourier transformation of the polarization vectors shown in Figure 4.2. Panel (a) corresponds to Figure 4.2(a), panel (b) corresponds to Figure 4.2(b), and panel (c) corresponds to Figure 4.2(c). The zoomed views show 24×24 samples out of the original 64×64 samples around the center of the filters.

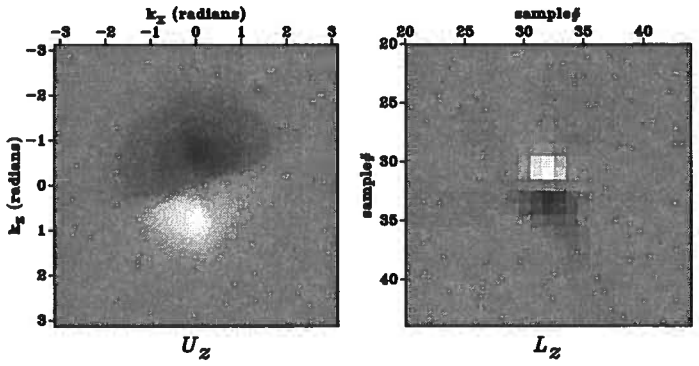

(a)

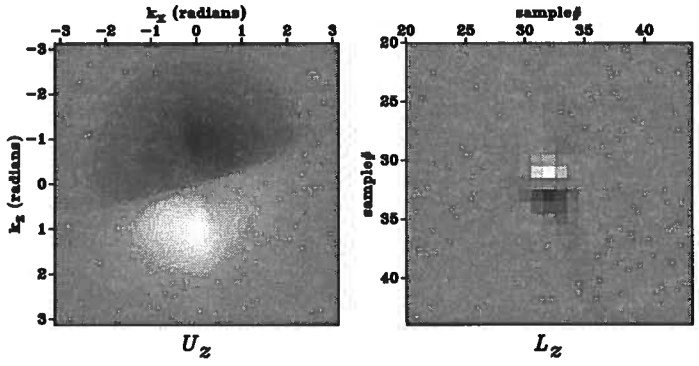

(b)

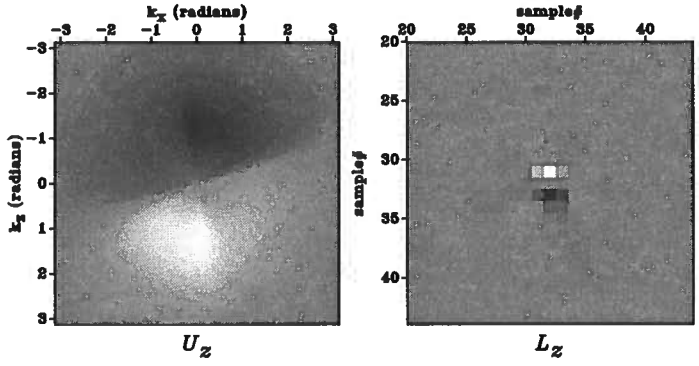

(c)

Figure 4.4. Panels (a)–(c) correspond to component U_z (left) and operator L_z (right) for σ values of 0.25, 1.00, and 1.25 radians in equation 4.5, respectively. A larger value of σ results in more spread components in the wavenumber domain and more concentrated operators in the space domain.

isotropic.

For TTI media, due to the asymmetry of the Fourier domain derivatives (Figure 4.1(b)), one needs to apply a rotational symmetric taper to the polarization vector components to obtain continuity across Nyquist wavenumbers. A simple Gaussian taper

$$g(\mathbf{k}) = C\,exp\left[-\frac{|\mathbf{k}|^2}{2\sigma^2}\right] \tag{4.5}$$

can be used, where C is a normalizing constant. When one chooses a standard deviation of $\sigma = 1$ radian, the magnitude of this taper at $|\mathbf{k}| = \pi$ radians is about 0.7% of the peak value, and therefore the TTI components can be safely assumed to be continuous across the Nyquist wavenumbers. Tapering the polarization vector components in Figure 4.1 with the function in equation 4.5, one obtains the plots in Figure 4.2. The panels in Figure 4.2, which exhibits circular continuity across the Nyquist wavenumbers, transform to the space-domain separators in Figure 4.3. The space-domain filters for TTI media is rotated from the VTI filters, also by the tilt angle ν.

The value of σ determines the size of the operators in the space domain and also affects the frequency content of the separated wave-modes. For example, Figure 4.4 shows the component U_z and operator L_z for σ values of 0.25, 1.00, and 1.25 radians. A larger value of σ results in more concentrated operators in the space domain and better preserved frequency of the separated wave-modes. However, one needs to ensure that the function $g(\mathbf{k})$ at $|\mathbf{k}| = \pi$ radians is small enough to assume continuity of the value function across Nyquist wavenumbers. When one chooses $\sigma = 1$ radian, the TTI components can be safely assumed to be continuous across the Nyquist wavenumbers.

For heterogeneous models, I can pre-compute the polarization vectors at each grid point as a function of the V_{P0}/V_{S0} ratio, the Thomsen parameters ϵ and δ, and tilt angle ν. I then transform the tapered polarization vector components to the space domain to obtain the spatially-varying separators L_x and L_z. The separators for the entire model are stored and used to separate P- and S-modes from reconstructed elastic wavefields at different time

steps. Thus, wavefield separation in TI media can be achieved simply by non-stationary filtering with spatially varying operators. I assume that the medium parameters vary slowly in space and that they are locally homogeneous. For complex media, the localized operators behave similarly to the long finite difference operators used for finite difference modeling at locations where medium parameters change rapidly.

4.4 Wave-mode separation for 3D TI media

In order to separate all three modes, P, SV, and SH, one needs to construct 3D separators. Dellinger (1991) shows that P-waves can be separated from two shear modes by a straightforward extension of the 2D algorithm. Indeed, for 3D TI media, one can always obtain the P-mode by constructing P-wave separators represented by the polarization vector $\mathbf{U}_P = \{U_x, U_y, U_z\}$ and then projecting the 3D elastic wavefields onto the vector $\mathbf{U}_P$. The P-wave polarization vector with components $\{U_x, U_y, U_z\}$ is obtained by solving the 3D Christoffel equation (Aki & Richards, 2002; Tsvankin, 2005):

$$\begin{bmatrix} G_{11}-\rho V^2 & G_{12} & G_{13} \\ G_{12} & G_{22}-\rho V^2 & G_{23} \\ G_{13} & G_{23} & G_{33}-\rho V^2 \end{bmatrix} \begin{bmatrix} U_x \\ U_y \\ U_z \end{bmatrix} = 0\,. \tag{4.6}$$

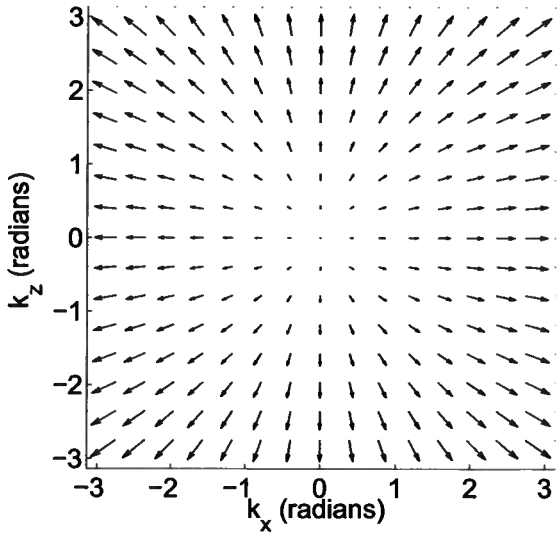

(a)

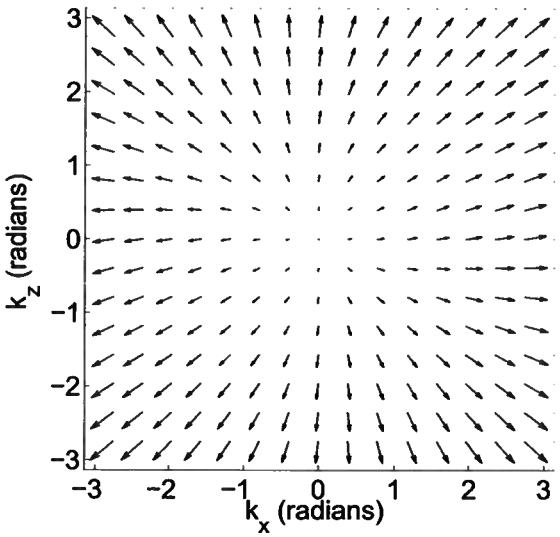

(b)

Figure 4.5. Polarization vectors of P-mode as a function of normalized wavenumbers k_x and k_z ranging from $-\pi$ radians to $+\pi$ radians, for (a) a VTI model with $V_{P0} = 3.0$ km/s, $V_{S0} = 1.5$ km/s, $\epsilon = 0.25$ and $\delta = -0.29$, and for (b) a TTI model with the same model parameters as (a) and a symmetry axis tilt $\nu = 30°$. The vectors in (b) are rotated 30° with respect to the vectors in (a) around $k_x = 0$ and $k_z = 0$.

The notation in this equation is the same as in equation 3.8. For TTI media, the matrix $\mathbf{G}$ has the elements

$$G_{11} = c_{11}n_x^2 + c_{66}n_y^2 + c_{55}n_z^2 + 2c_{16}n_xn_y + 2c_{15}n_xn_z + 2c_{56}n_yn_z\,, \tag{4.7}$$

$$G_{22} = c_{66}n_x^2 + c_{22}n_y^2 + c_{44}n_z^2 + 2c_{26}n_xn_y + (c_{45}+c_{46})n_xn_z + 2c_{24}n_yn_z\,, \tag{4.8}$$

$$G_{33} = c_{55}n_x^2 + c_{44}n_y^2 + c_{33}n_z^2 + 2c_{45}n_xn_y + 2c_{35}n_xn_z + 2c_{34}n_yn_z\,, \tag{4.9}$$

$$G_{12} = c_{16}n_x^2 + c_{26}n_y^2 + c_{45}n_z^2 + (c_{12}+c_{66})n_xn_y + (c_{14}+c_{56})n_xn_z + (c_{25}+c_{46})n_yn_z\,, \tag{4.10}$$

$$G_{13} = c_{15}n_x^2 + c_{46}n_y^2 + c_{35}n_z^2 + (c_{14}+c_{56})n_xn_y + (c_{13}+c_{55})n_xn_z + (c_{36}+c_{45})n_yn_z\,, \tag{4.11}$$

$$G_{23} = c_{56}n_x^2 + c_{24}n_y^2 + c_{34}n_z^2 + (c_{25}+c_{46})n_xn_y + (c_{36}+c_{45})n_xn_z + (c_{23}+c_{44})n_yn_z\,. \tag{4.12}$$

When constructing shear mode separators, one faces an additional complication: SV- and SH-waves have the same velocity along the symmetry axis of a TI medium, and this singularity prevents one from obtaining polarization vectors for shear modes in this particular direction by solving the Christoffel equation (Tsvankin, 2005). In 3D TI media, the polarization of the shear modes excited by point sources are non-linear around the singular directions and cannot be characterized by a plane-wave solution (Vavryčuk, 2002). Consequently, constructing 3D global separators for fast and slow shear modes is difficult.

To mitigate the effects of this "kiss" singularity, I use the mutual orthogonality among the P, SV, and SH modes depicted in Figure 4.6. In this figure, vector $\mathbf{n} = \{\sin\nu\cos\alpha, \sin\nu\sin\alpha, \cos\nu\}$ represents the symmetry axis of a TTI medium, with ν and α being the tilt and azimuth of the symmetry axis, respectively. The wave vector $\mathbf{k}$ characterizes the propagation direction of a plane wave. Vectors $\mathbf{P}$, $\mathbf{SV}$, and $\mathbf{SH}$ symbolize the compressional, and fast and slow shear polarization directions, respectively. For TI media, the symmetry axis $\mathbf{n}$ and any wave vector $\mathbf{k}$ form a symmetry plane. For a plane wave propagating in the

direction $\mathbf{k}$, the P-wave is polarized in this symmetry plane and deviates from the vector $\mathbf{k}$; the SV- and SH-waves are polarized perpendicular to the P-mode, in and out of the symmetry plane, respectively.

Using this mutual orthogonality among all three modes, I first obtain the SH-wave polarization vector $\mathbf{U}_{SH}$ by cross multiplying vectors $\mathbf{n}$ and $\mathbf{k}$, which ensures that the SH mode is polarized orthogonal to symmetry planes:

$$\begin{aligned} \mathbf{U}_{SH} &= \mathbf{n} \times \mathbf{k} \\ &= \{k_z n_y - k_y n_z, \\ &\quad k_x n_z - k_z n_x, \\ &\quad k_y n_x - k_x n_y\}. \end{aligned} \tag{4.13}$$

Then I calculate the SV polarization vector $\mathbf{U}_{SV}$ by cross multiplying polarization vectors P and SH modes, which ensures the orthogonality between SV and P modes and SV and SH modes:

$$\begin{aligned} \mathbf{U}_{SV} &= \mathbf{U}_P \times \mathbf{U}_{SH}, \\ &= \{k_y n_x U_y - k_x n_y U_y + k_z n_x U_z - k_x n_z U_z, \\ &\quad k_z n_y U_z - k_y n_z U_z + k_x n_y U_x - k_y n_x U_x, \\ &\quad k_x n_z U_x - k_z n_x U_x + k_y n_z U_y - k_z n_y U_y\}. \end{aligned} \tag{4.14}$$

Here, the magnitude of the P-wave polarization vectors for a certain wavenumber $|\mathbf{k}|$ is a constant:

$$|U_P| = \sqrt{U_x^2 + U_y^2 + U_z^2} = c. \tag{4.15}$$

This ensures that for a certain wavenumber, P-waves obtained by projecting the elastic wavefields onto the polarization vectors are uniformly scaled. For comparison, the magni-

tudes of all three modes are respectively

$$|U_P| = c, \tag{4.16}$$

$$|U_{SV}| = c\sin\phi, \tag{4.17}$$

$$|U_{SH}| = c\sin\phi, \tag{4.18}$$

where ϕ is the polar angle of the propagating plane wave, i.e., the angle between vectors $\mathbf{k}$ and $\mathbf{n}$. Figure 4.7 shows the polarization vectors of P-, SH-, and SV-modes computed using equations 4.6, 4.13, and 4.14, respectively. All P-wave polarization vectors in Figure 4.7(a) all have the same magnitude, but the SV and SH polarization vectors in Figures 4.7(c) and (b) do not. In the symmetry axis direction, they are zero vectors, and in the isotropy plane, they are unit vectors. The amplitudes and directions of the shear-mode polarization vectors in $\mathbf{k}$-domain change smoothly. Using separators represented by solutions of equation 4.6 and expressions 4.13 and 4.14 to filter the wavefields, I obtain separated shear modes that are scaled differently than is the P-mode. For a certain wavenumber, the shear modes are scaled by $\sin\phi$, with ϕ being the polar angle, which increases from zero in the symmetry direction to unity in the orthogonal propagation directions. Physically, S-wave polarizations in the symmetry direction are determined by the source. However, to simplify the problem, the shear-waves around singularity are zeroed.

The components of the polarization vectors for P-, SV-, and SH-waves can be transformed back to the space domain to construct spatial filters for 3D heterogeneous TI media. For example, Figure 4.8 illustrates nine spatial filters transformed from the Cartesian components of the polarization vectors shown in Figure 4.7. All these filters can be spatially varying when the medium is heterogeneous. Therefore, in principle, wave-mode separation in 3D would perform well even for models that have complex structures and arbitrary tilts and azimuths of TI symmetry.

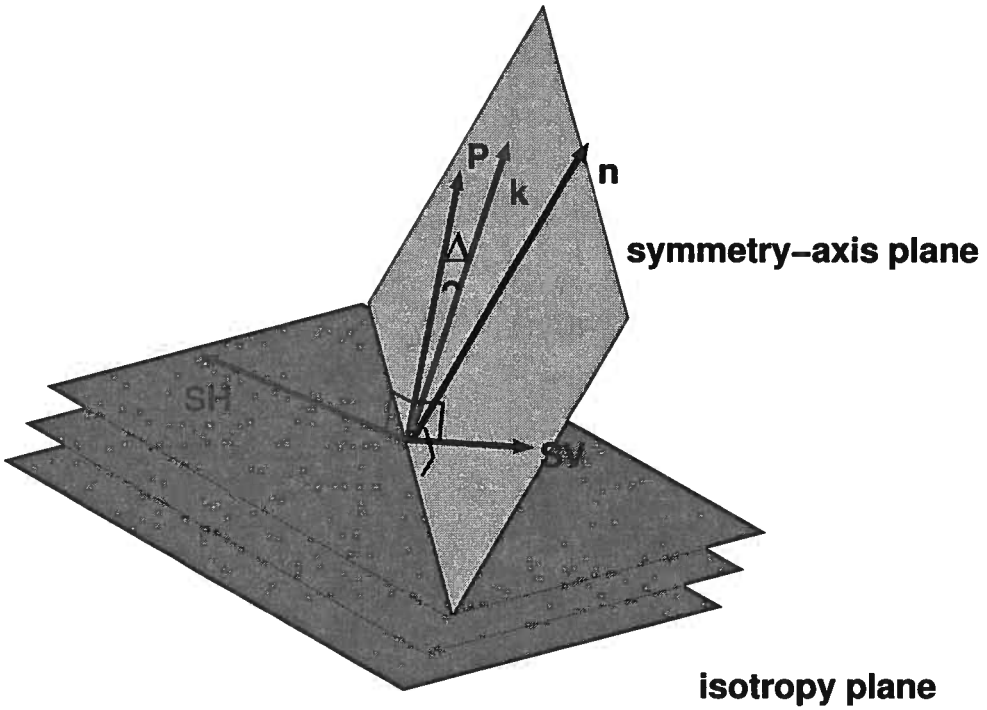

Figure 4.6. (a) Schematic showing the elastic wave-mode polarization in a 3D TI medium. The three parallel planes represent the isotropy planes of the medium. The vector **n** represents the symmetry axis, which is orthogonal to the isotropy plane and has tilt angle ν and azimuth angle α. The vector **k** is the propagation direction of a plane wave. The angles between vectors **k** and **n** is the polar angle θ in equation 3.10. Wave modes P, SV, and SH are polarized in the directions **P**, **SV**, and **SH**, respectively, and are polarized orthogonal to each other for a fixed wave vector **k**. The deviation of vectors **P** and **k** indicates that the medium is anisotropic.

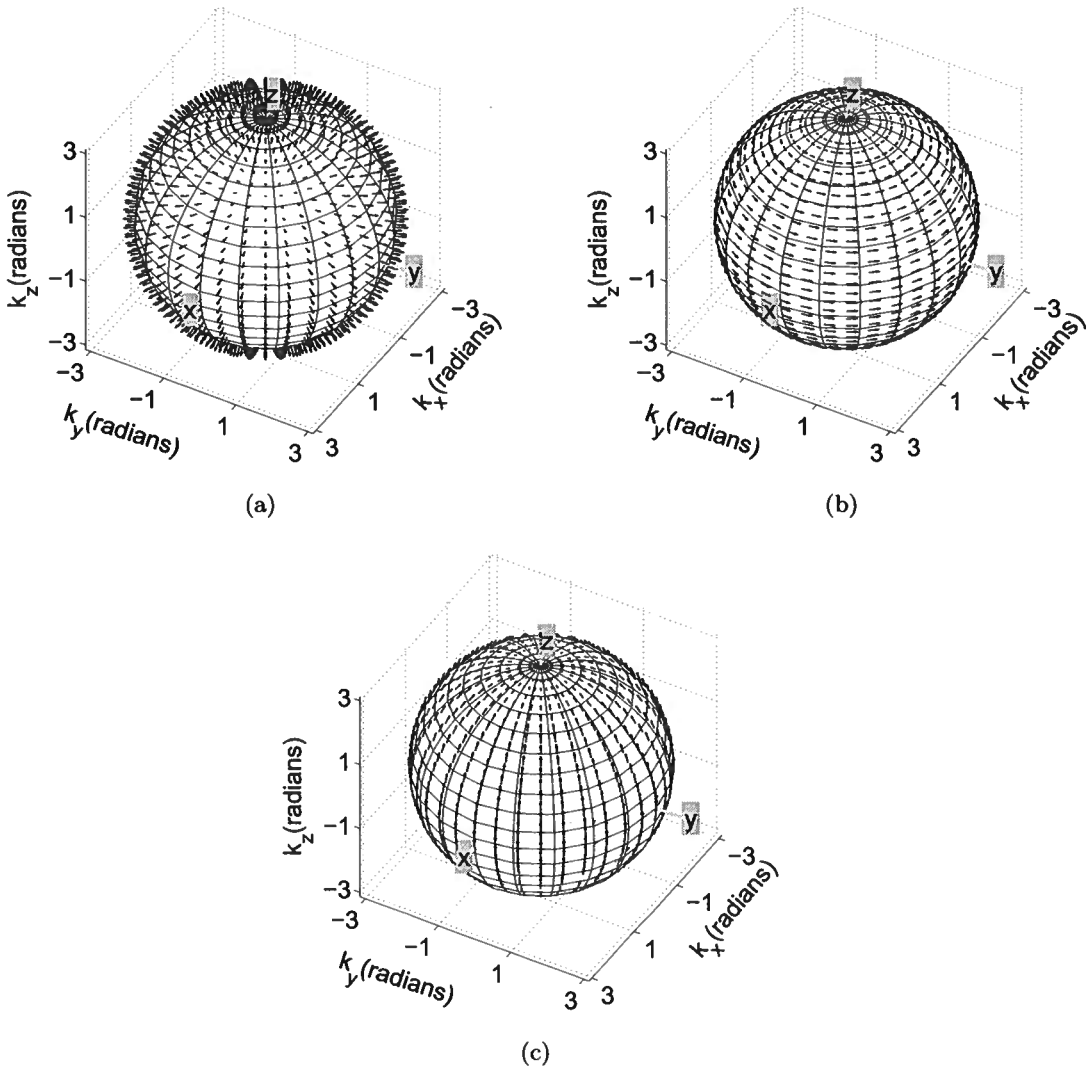

Figure 4.7. Wave-mode polarization for P-, SH-, and SV-mode for a VTI medium with parameters $V_{P0} = 4.95$ km/s, $V_{S0} = 2.48$ km/s, $\epsilon = 0.4$, and $\delta = 0.1$. The P-mode polarization is computed using the 3D Christoffel equation, and SV and SH polarizations are computed using equations 4.14 and 4.13. Note that the SV- and SH-wave polarization vectors have zero amplitude in the vertical direction.

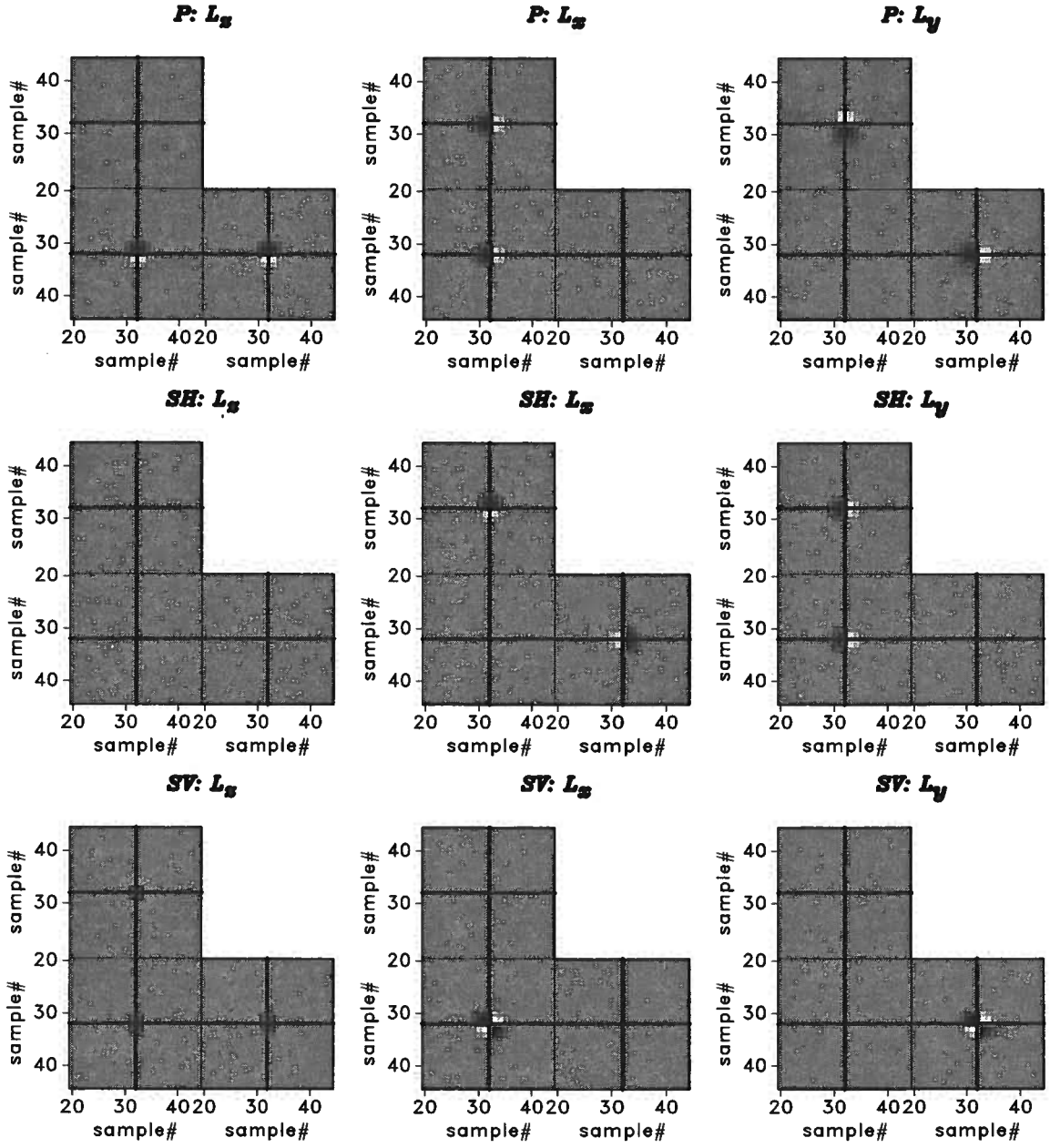

Figure 4.8. Separation filters L_x, L_y, and L_z for the P, SV, and SH modes for a VTI medium. The corresponding wavenumber-domain polarization vectors are shown in Figure 4.7. Note that the filter L_z for the SH mode is blank because the z component of the polarization vector is zero. The zoomed views show 24×24 samples out of the original 64×64 samples around the center of the filters.

4.5 Examples

I illustrate the anisotropic wave-mode separation with a simple fold synthetic example and a more challenging example based on the elastic Marmousi II model (Bourgeois *et al.*, 1991). I then show the wave-mode separation for a 3D TTI model.

4.5.1 2D TTI fold model

Consider the 2D fold model shown in Figure 4.9. Panels 4.9(a)–(f) show V_{P0}, V_{S0}, density, parameters ϵ, δ, and the local tilts ν of the model, respectively. The symmetry axis is orthogonal to the reflectors throughout the model. Figure 4.10 illustrates the separators obtained at different locations in the model and defined by the intersections of x coordinates 0.15, 0.3, 0.45 km and z coordinates 0.15, 0.3, 0.45 km, shown by the dots in Figure 4.9(f). Since the operators correspond to different combinations of the V_{P0}/V_{S0} ratio and parameters ϵ, δ, and tilt angle ν, they have different forms. However, the orientation of the operators conform to the corresponding tilts at the locations shown by the dots in Figure 4.9(f). For complex models, the symmetry-axis orientations vary spatially, which makes it difficult to rotate the wavefields to the local symmetry-axis directions. Consequently, the elastic wavefields are reconstructed in unrotated Cartesian coordinates, and when separating wave-modes, I use operators constructed in the unrotated Cartesian coordinates. To illustrate the relationship between the operators and the local tilts, the filters in Figure 4.10 are projected onto the local symmetry axes and the orthogonal directions at the filter location. As shown in Figure 4.3, the rotated filters (Figure 4.3(c)) show a clearer relation with the tilt angle, while the non-rotated filters (Figure 4.3(b)), which are used in the wave-mode separation, do not.

Figure 5.5(a) shows the vertical and horizontal components of one snapshot of the simulated elastic anisotropic wavefield; Figure 4.11(b) shows the separation into P- and S-modes using divergence and curl operators; Figure 4.11(c) shows the separation into P and S modes using VTI filters, i.e., assuming zero tilt throughout the model; and Figure 4.11(d)

shows the separation obtained with the TTI operators constructed using the local medium parameters with correct tilts. The isotropic separation shown in Figure 4.11(b) is incomplete; for example, at $x = 0.4$ km and $z = 0.1$ km, and at $x = 0.4$ km and $z = 0.35$ km, residuals for direct P and S arrivals are visible in the P and S panels, respectively. A comparison of Figures 4.11(c) and (d) indicates that the spatially-varying derivative operators with correct tilts successfully separate the elastic wavefields into P and S modes, while the VTI operators only work in the part of the model that is locally VTI.

4.5.2 Marmousi II model

The second model (Figure 4.12) uses an elastic anisotropic version of the Marmousi II model (Bourgeois *et al.*, 1991). In the modified model, V_{P0} is taken from the original model (Figure 4.12(a)), the V_{P0}/V_{S0} ratio ranges from 2 to 2.5, (Figure 4.12(b)), and the density ρ is taken from the original model (Figure 4.12(c)). The parameters ϵ and δ are derived from the density model ρ with the relations of $\epsilon = 0.25\rho - 0.3$ and $\epsilon = 0.125\rho - 0.1$, respectively. The parameter ϵ ranges from 0.13 to 0.36 Figure 4.12(d), and parameter δ ranges from 0.11 to 0.24 Figure 4.12(e). These anisotropy parameters are obtained by assuming linear relationships to the density model, and therefore, they both follow the structure of the model. Figure 4.12(f) represents the local dips obtained from the density model using plane wave destruction filters (Fomel, 2002). The dip model is used to both simulate the wavefields and construct TTI separators. A displacement source oriented at 45° to the vertical direction and located at coordinates $x = 11$ km and $z = 1$ km is used to simulate the elastic anisotropic wavefield.

Figure 4.13(a) presents one snapshot of the simulated elastic wavefields using the anisotropic model shown in Figure 4.12. Figures 4.13(b), (c), and (d) demonstrate the separation using conventional divergence and curl operators, VTI filters, and correct TTI filters, respectively. The VTI filters are constructed assuming zero tilt throughout the model, and the TTI filters are constructed with the dips used for modeling. As expected, the con-

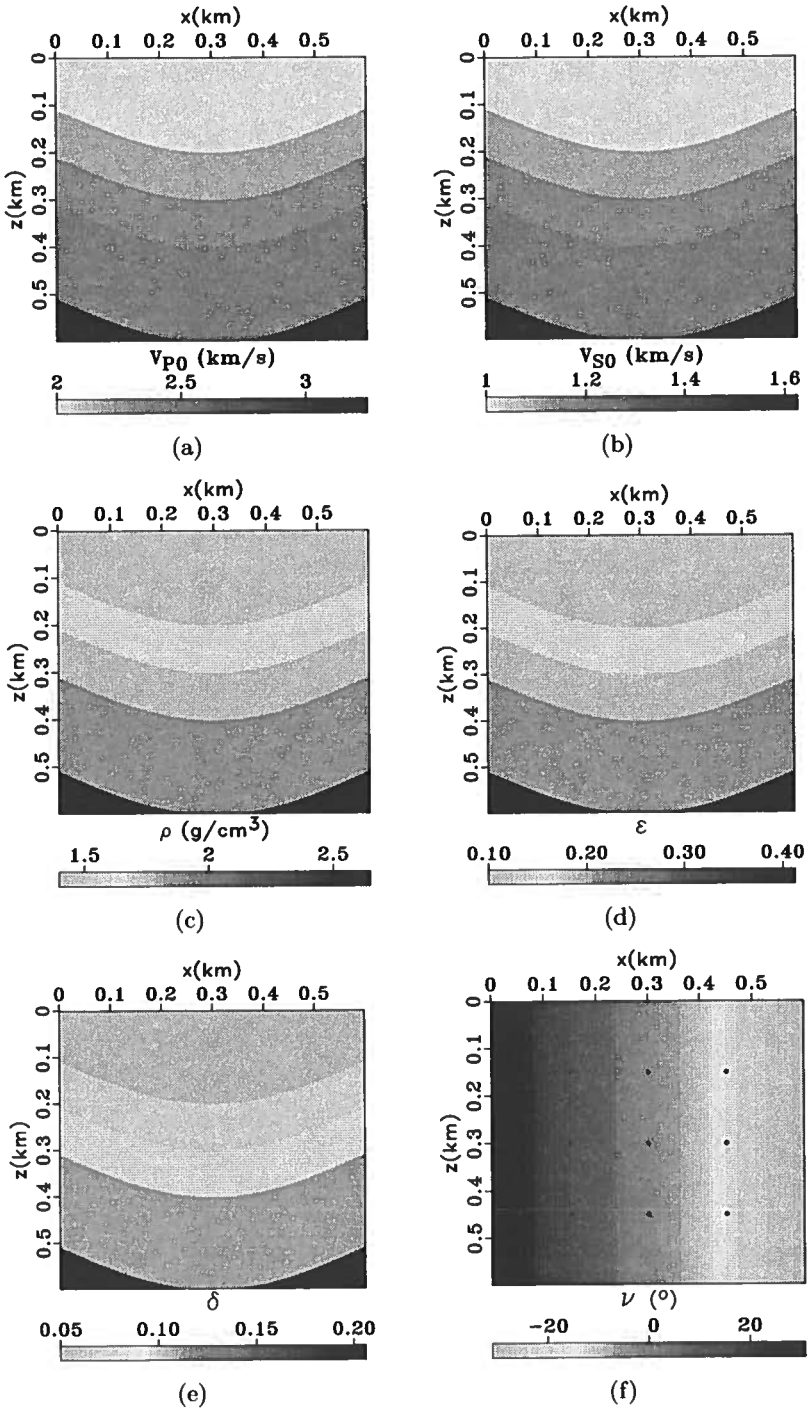

Figure 4.9. Fold model with parameters (a) V_{P0}, (b) V_{S0}, (c) density, (d) ϵ, (e) δ, and (f) tilt angle ν. The dots in panel (f) correspond to the locations of the anisotropic operators shown in Figure 4.10.

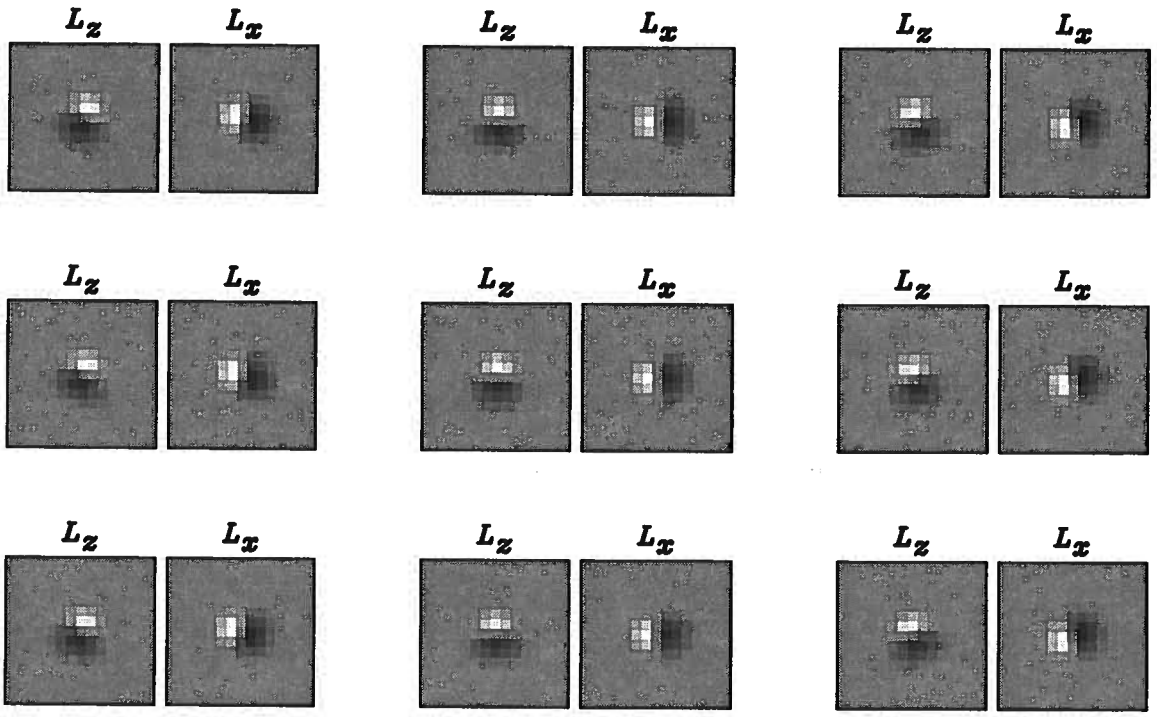

Figure 4.10. TTI wave-mode separation filters projected to local symmetry axes and their orthogonal directions. Here, I use $\sigma = 1$ in equation 4.5 to taper the polarization vector components before the Fourier transform. The filters correspond to the intersections of $x = 0.15$, 0.3, 0.45 km and $z = 0.15$, 0.3, 0.45 km for the model shown in Figure 4.9. The locations of these operators are also shown by the dots in Figure 4.9(f).

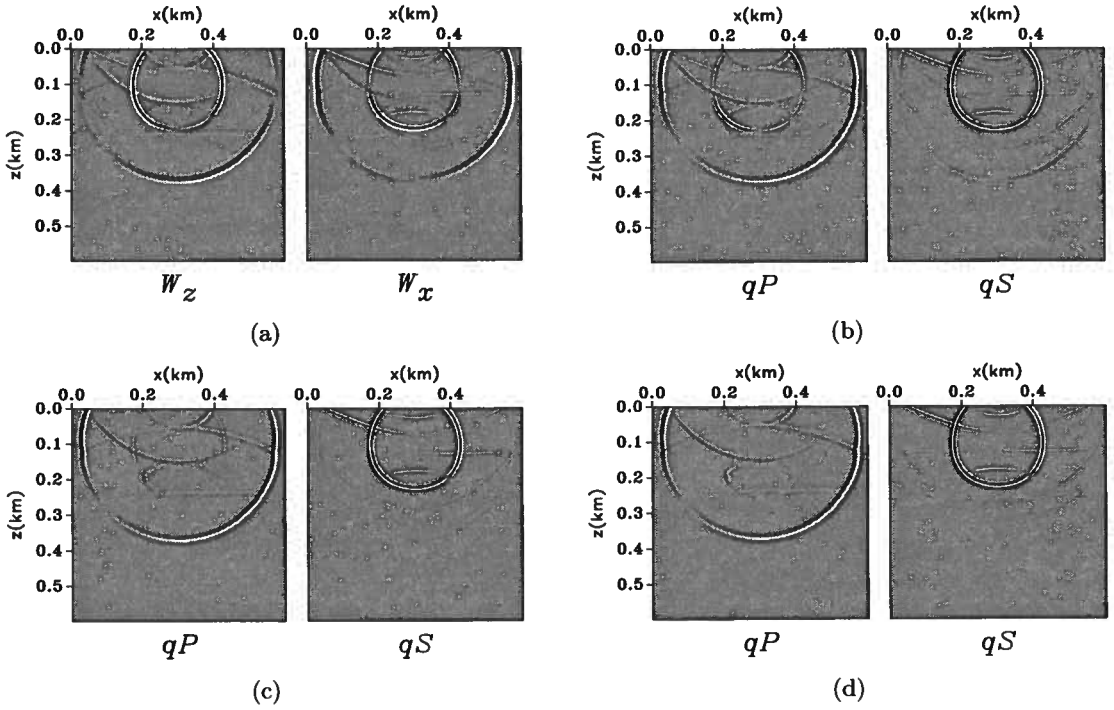

Figure 4.11. (a) A snapshot of the anisotropic wavefield simulated with a vertical point displacement source at $x = 0.3$ km and $z = 0.1$ km for the model shown in Figure 4.9. Panels (b) to (d) are the anisotropic P and S modes separated using isotropic, VTI, and TTI separators, respectively. The separation is incomplete in panels (b) and (c) where the model is strongly anisotropic and where the model tilt is large, respectively. Panel (d) shows the best separation among all.

ventional divergence and curl operators fail at locations where anisotropy is strong. For example, in Figure 4.13(b) at coordinates $x = 12.0$ km and $z = 1.0$ km, there are strong S-wave residuals, and at coordinates $x = 13.0$ km and $z = 1.5$ km, there are strong P-wave residuals. VTI separators fail at locations where the dip, and, therefore, the symmetry-axis tilt, is large. For example, in Figures 4.13(c) at coordinates $x = 10.0$ km and $z = 1.2$ km, there are strong S-wave residuals. However, even for this complicated model, separation using TTI separators is effective at locations where medium parameters change rapidly.

4.5.3 3D TTI model

I use a homogeneous TTI model to illustrate the separation of P-, SV-, and SH-modes. Figure 4.14 shows a snapshot of the elastic wavefields in the z, x, and y directions. A displacement source located at the center of the model and oriented at tilt 45° and azimuth 45° is used to excite the wavefield. Figure 4.15 shows successfully separated P-, SV-, and SH-modes. In this model, the parameter γ, which is responsible for the anisotropy of SH-mode, is set to zero so that there is no SH-wave angular velocity variation. The spherical wavefront in the SH-panel indicates successful separation of SV- and SH-modes.

Because this model is homogeneous, the separation is implemented in the wavenumber domain to reduce computation cost. For heterogeneous models, 3D non-stationary filtering is necessary to separate different wave-modes. I do not perform wave-mode separation in 3D heterogeneous models because of the high computational cost, as will be discussed in more detail in the following section.

4.6 Discussion

4.6.1 Computational issues

The separation of wave-modes for heterogeneous TI models requires non-stationary spatial filtering with large operators (operators of 50 samples in each dimension are used in this chapter), which is computationally expensive. The cost is directly proportional to the size of the model and to the size of each operator. Furthermore, in a simple imple-

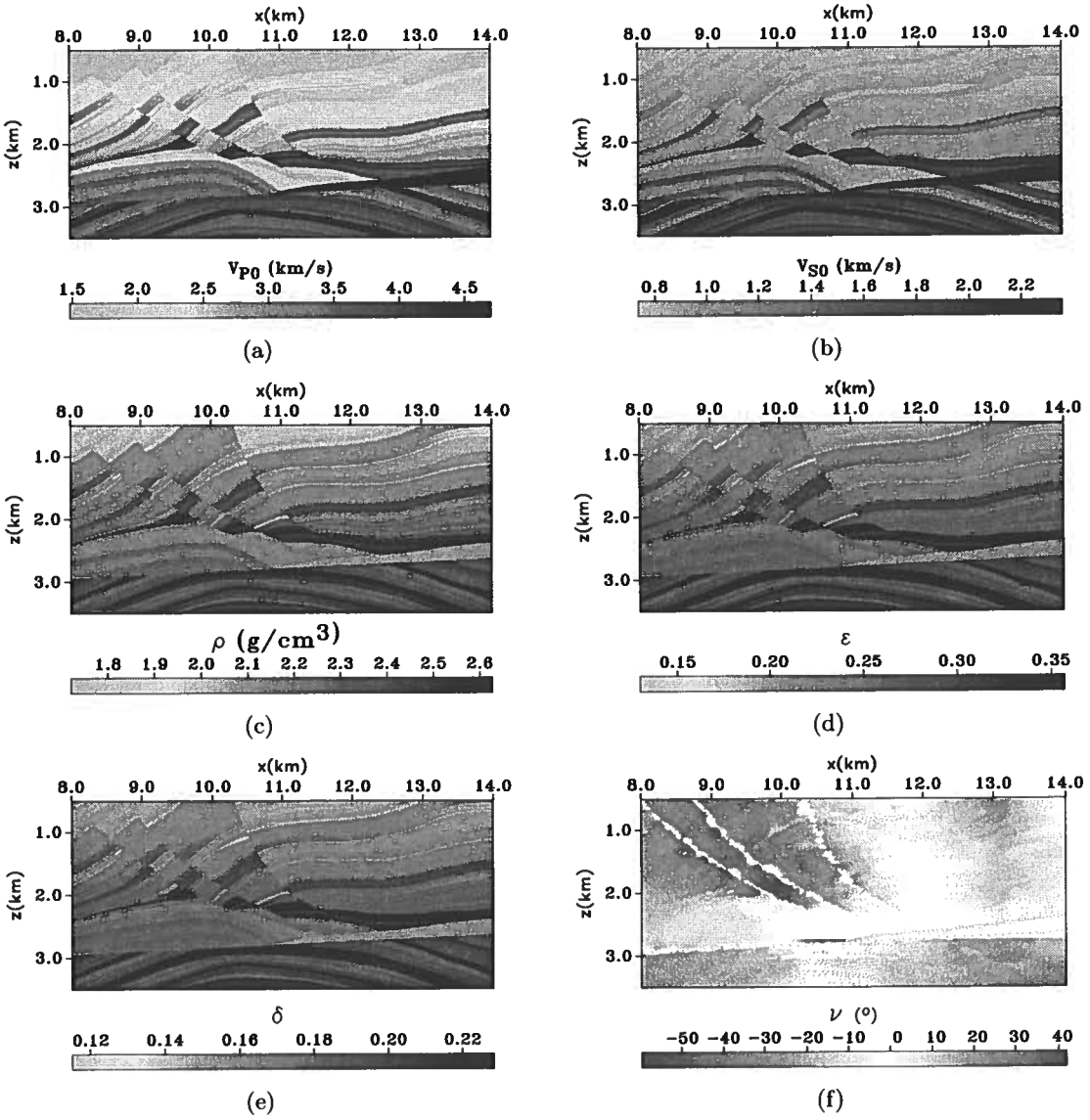

Figure 4.12. Anisotropic elastic Marmousi II model with (a) V_{P0}, (b) V_{S0}, (c) density, (d) ϵ, (e) δ, and (f) local tilt angle ν.

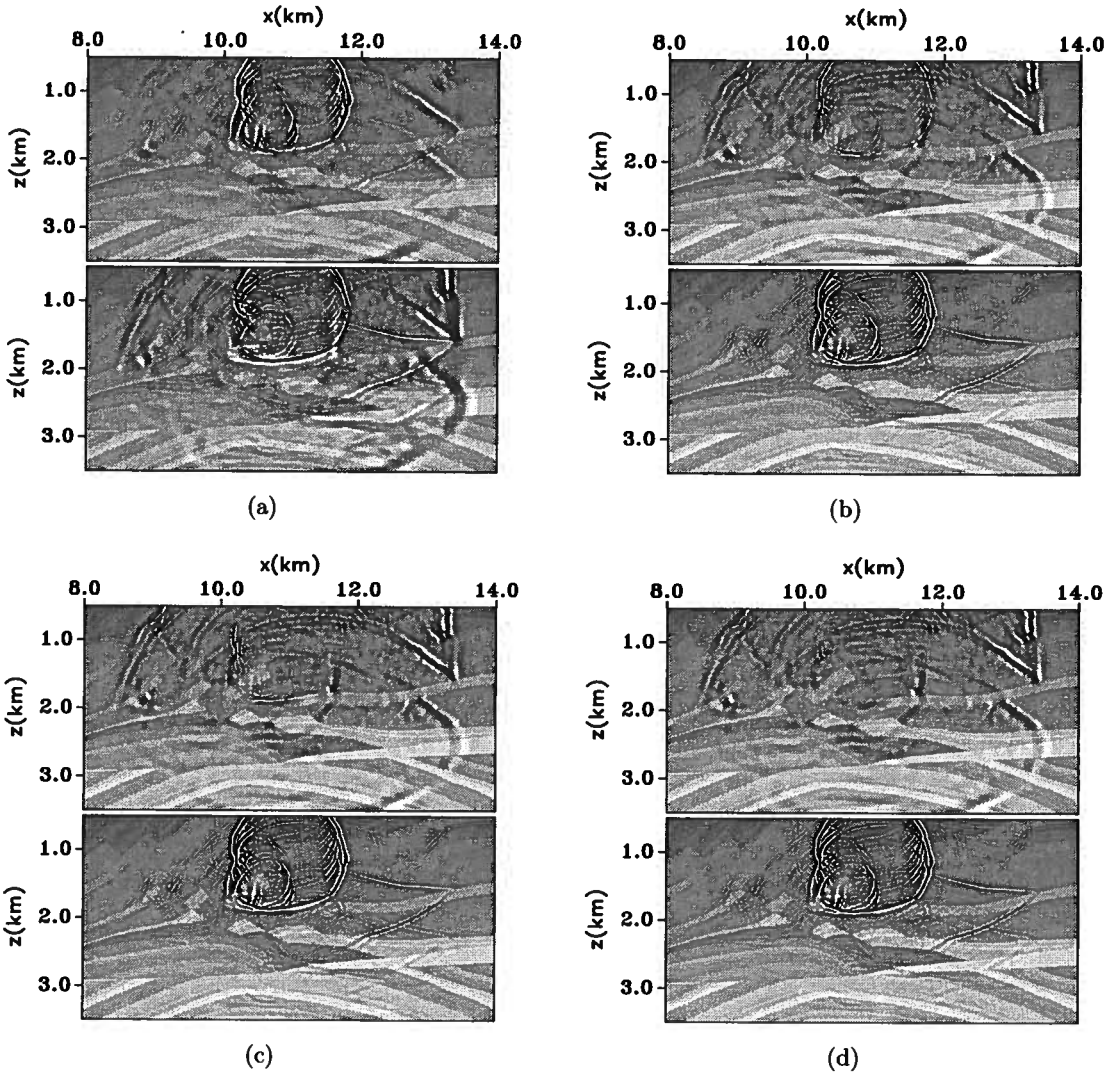

Figure 4.13. (a) A snapshot of the vertical and horizontal displacement wavefield simulated for model shown in Figure 4.12. Panels (b) to (c) are the P- and SV-wave separation using $\nabla\cdot$ and $\nabla\times$, VTI separators and TTI separators, respectively. The separation is incomplete in panels (b) and (c) where the model is strongly anisotropic and where the model tilt is large, respectively. Panel (d) shows the best separation.

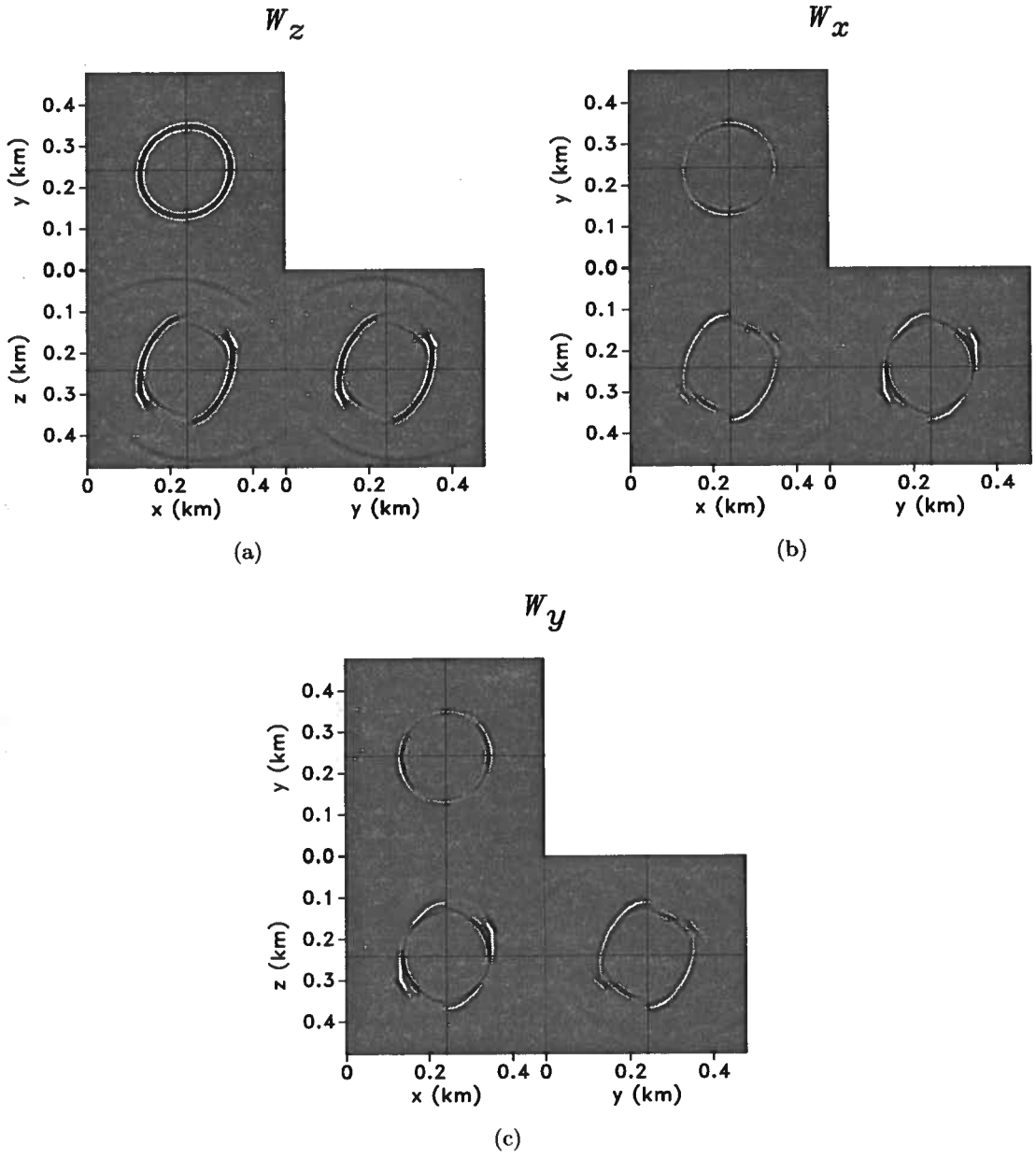

Figure 4.14. A snapshot of the elastic wavefield in the z, x and y directions for a 3D VTI model. The model has parameters $V_{P0} = 3.5$ km/s, $V_{S0} = 1.75$ km/s, $\rho = 2.0$ g/cm^3, $\epsilon = 0.4$, $\delta = 0.1$, and $\gamma = 0.0$. A displacement source oriented at 45° to the vertical direction and located at coordinates $x = 11$ km and $z = 1$ km is used to simulate the elastic anisotropic wavefield.

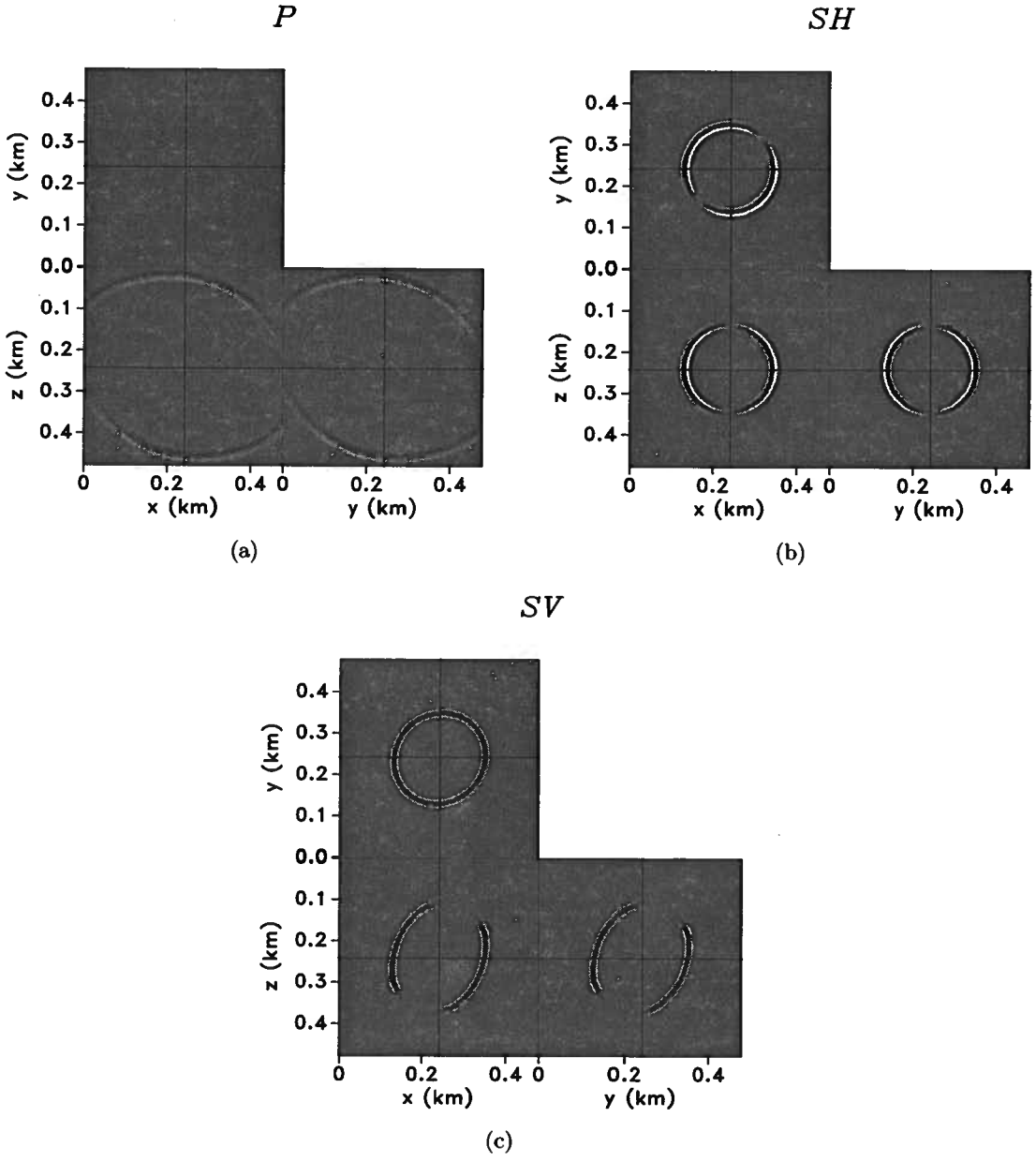

Figure 4.15. Separated P-, SV- and SH-wave-modes for the elastic wavefields shown in Figure 4.14. P, SV, and SH are well separated from each other.

mentation, the storage for the separation operators of the entire model is proportional to the size of the model and to the size of each operator. Suppose that a 3D elastic TTI model is characterized by model parameters V_{P0}, V_{S0}, ϵ, δ, and symmetry axis tilt angle ν and azimuth angle α. For a 3D model of $300 \times 300 \times 300$ grid points, if one assumes that all operators have a size of $50 \times 50 \times 50$ samples, the storage for the operators is 300^3 grid points $\times\ 50^3$ samples/independent operator $\times$ 3 independent operators/grid point $\times$ 4 Bytes/sample = 40.5 TB. This is not feasible in ordinary processing. However, since there are relatively few medium parameters (i.e., the V_{P0}/V_{S0} ratio, ϵ, δ, and angles ν and α), which determine the properties of the operators, one can construct a look-up table of operators as a function of these parameters, and search the appropriate operators at every location in the model when doing wave-mode separation. For example, suppose one knows that $V_{P0}/V_{S0} \in [1.5, 2.0]$, $\epsilon \in [0, 0.3]$, $\delta \in [0, 0.1]$, the symmetry axis tilt $\nu \in [-90°, 90°]$ and azimuth $\alpha \in [-180°, 180°]$, one can sample the V_{P0}/V_{S0} ratio at every 0.1, ϵ and δ at every 0.03, and the angles at every 15°. In this case, one only needs a storage of $6 \times 10 \times 3 \times 12 \times 24$ combinations of medium parameters$\times 50^3$ sample/independent operator$\times$3 independent operators/combination of medium parameters$\times$ 4 Bytes/sample = 77 GB; this is more manageable, although still a large volume to store.

4.6.2 S wave-mode amplitudes

Although the procedure used in this chapter to separate S-waves into SV- and SH-modes is straightforward, the amplitudes of S-modes are not accurate because the S-wave separators are not normalized for any given wavenumbers. The amplitudes of S-modes obtained in this way are zero in the symmetry-axis direction and gradually increase to unity in the isotropy plane.

The main problem that prevents one from constructing the 3D global shear wave separators is that the SV and SH polarization vectors are singular in the symmetry-axis direction, i.e., they are not defined by the plane-wave solution of the TI elastic wave equa-

tion. Various studies (Kieslev & Tsvankin, 1989; Vavryčuk, 2002; Tsvankin, 2005) show that S-waves excited by point forces can have non-linear polarization in several special directions. For example, around the direction of point force, the S-wave can have non-linear polarization. This phenomenon exists even in isotropic media. Anisotropic velocity and amplitude variations can also cause the S-waves to be polarized non-linearly. For instance, S-wave triplication, S-wave singularities, and S-wave velocity extrema can all result in S-wave polarization anomalies. In these special directions, SV- and SH-mode polarizations are incorrectly defined by plane-wave theory. One possibility for obtaining more accurate S-wave amplitudes is to approximate the anomalous polarization with the major axes of the quasi-ellipses of the S-wave polarization, which can be obtained by incorporating the first-order term in the ray tracing method. This extension is impractical and remains outside the scope of this chapter.

Although the simplified approach used in this chapter ignores the complicated polarization behavior in some propagation directions, it does successfully separate fast and slow shear modes kinematically. This allows one to use the separated scalar shear-modes for implementing the subsequent imaging condition and obtain images with clear physical meaning.

4.7 Conclusions

In this chapter, I present a method for obtaining spatially-varying wave-mode separators for TI models, which can be used to separate elastic wave-modes in complex media. The method computes the components of the polarization vectors in the wavenumber domain and then transforms them to the space domain to obtain spatially-varying filters. In order for the operators to work in TI models with a titled symmetry axis, I incorporate one more parameter—the local tilt angle ν—in addition to the parameters needed for the VTI operators. This kind of spatial filters can be used to separate complicated wavefields in TI models with strong heterogeneity and anisotropy. I test the separation with synthetic

models that have realistic geologic complexity. The results support the effectiveness of wave-mode separation with non-stationary filtering.

I also extend the wave-mode separation to 3D TI models. The separation of three modes in 3D TI media is based on the plane-wave solution to the elastic wave equation. The P-mode separators can be constructed by solving the Christoffel equation for the P-wave eigenvectors with local medium parameters. The SV and SH separators are constructed using the mutual orthogonality among P, SV, and SH modes. For the three modes, there are a total number of nine separators, with three components for each mode. The separators vary with the medium parameters V_{P0}, V_{S0}, ϵ, δ, and tilt ν and azimuth α of the symmetry axis. In anisotropic media, P-waves polarize more linearly than S-waves. Therefore, the plane-wave approximation preserves the separated P-waves better than the S-waves. Nevertheless, the proposed technique successfully separates fast and slow shear wavefields. The process of constructing 3D separators and separating wave-modes in 3D eliminates the step of projecting the wavefields into symmetry-axis plane and isotropy plane, which is only effective for models with an invariant symmetry axis. Spatially-varying 3D separators have potential benefits for complex models and can be used to separate wave-modes in elastic reverse time migration (RTM) for TTI models. The spatially-varying 3D separators are built at a large computational and storage cost, and therefore, a more efficient separation method, such as the proposed table look-up alternative, is necessary for a successful implementation.

Chapter 5

Improving the efficiency of elastic wave-mode separation for heterogeneous TTI media

5.1 Summary

In this chapter, I show an efficient method for wave-mode separation, which exploits the same general idea of projecting wavefields onto polarization vectors. The method consists of two steps: 1) separate wave-modes in the wavenumber domain at a number of reference models to obtain the same number of partially separated wavefields; then transform all the wavefields to the space domain; 2) interpolate the wavefields (obtained in step 1) in the space domain using the spatially-variable model parameters. The new method resembles the phase-shift plus interpolation (PSPI) technique (Gazdag & Sguazzero, 1984), which interpolates the wavefields that are reconstructed at several reference velocities. Synthetic examples show that the separation followed by interpolation is effective for models with complex geology. The new technique has the benefit of both speed and accuracy.

5.2 Introduction

In Chapters 3 and 4, I show wave-mode separation in symmetry-axis planes of TI media. For heterogeneous models, wave-mode separation can be performed in the space domain using non-stationary spatial filtering, which is computationally expensive. In fact, the cost becomes prohibitive in 3D because it is proportional to the number of grids in the model and the size of each filter (Chapter 4). Zhang & McMechan (2010) separate wave modes for heterogeneous models that are comprised of several distinct geologic units, where the polarization vectors in each unit are stationary. They separate wave modes using

medium parameters taken from each unit and obtain a final separation by combining correctly separated modes from corresponding blocks. This approach is only effective when the model is simple and when it is easy to choose the separated modes from the corresponding units.

In this chapter, I propose a new approach for wave-mode separation in two steps. First, choose some reference models based on the model parameter distribution and separate wave modes in the wavenumber domain at these reference models. Then, transform all the separated modes to the space domain. Finally, interpolate the wavefields in the space domain using the spatially-variable model parameters. My approach is effective for geologic models with a high heterogeneity.

In the following, I show that wave-mode separation can be carried out more efficiently in a mixed domain—separation in the wavenumber domain followed by interpolation in the space domain. This procedure, which resembles the phase-shift plus interpolation (PSPI) process from wave-equation migration (Gazdag & Sguazzero, 1985; Ursenbach & Bale, 2009; Bale *et al.*, 2007), offers both speed and accuracy. I use synthetic examples to show that the proposed approach is efficient: I achieve approximately the same accuracy as the space-domain separation and significantly reduce the computational cost.

5.3 Wave mode separation in the wavenumber domain by interpolation

As illustrated in Chapters 3 and 4, accurate separation of wave modes for heterogeneous TI media requires non-stationary filtering with large operators in the space domain, which is computationally expensive. The computation cost is directly proportional to the size of the model and the size of the space-domain filters. Furthermore, in a simple implementation, the storage of the separation filters for the entire model is also proportional to the size of the model times the size of the filters. Thus, the spatial separation becomes prohibitively expensive in 3D.

I show a method to separate the wave-modes in the wavenumber domain at a much

lower cost: the wave-modes are first separated at a number of reference models in the wavenumber domain; then the separated modes obtained at these references are interpolated in the space domain. Here, for 3D TTI media, the model space is multi-dimensional:

$$\mathbf{m} = \{V_{P0}, V_{S0}, \epsilon, \delta, \gamma, \nu, \alpha\}\,, \tag{5.1}$$

where V_{P0} and V_{S0} are the P and S velocities along the symmetry axis, respectively; ϵ, δ, and γ are the Thomsen parameters; ν and α are the tilt and azimuth of the symmetry axis, respectively. All of these parameters can be spatially varying.

Mathematically, the separation is first carried out with reference model $\mathbf{m}^k$, $k = 1, 2, ...N$, with N being the number of reference models. Then the wave modes are inverse Fourier transformed to the space domain:

$$M^k(\mathbf{x}) = \mathcal{F}^{-1}\left\{\sum_{j=1}^{3} i\widetilde{W}_j(\mathbf{k})U^k_{Mj}(\mathbf{k})\right\}. \tag{5.2}$$

Here, M stands for different wave modes, i.e. P, SV, SH, and j stands for the x, y, and z components of the wavefields. At reference model $\mathbf{m}^k$, the polarization vector components are expressed by

$$U^k_{Mj} = U_{Mj}(\mathbf{m}^k)\,. \tag{5.3}$$

At any given model $\mathbf{m}$ one can express its polarization vectors as a weighted sum of the vectors at a subset of the reference models:

$$U_{Mj}(\mathbf{m}) = \sum_k w^k\left(\mathbf{m}(\mathbf{x}), \mathbf{m}^1, \mathbf{m}^2, \cdots, \mathbf{m}^N\right) U_{Mj}(\mathbf{m}^k)\,. \tag{5.4}$$

A Fourier transform of Equation 5.4 gives the $\mathbf{x}$-domain-weighted filters as

$$L_{Mj}(\mathbf{x}) = \sum_k w^k(\mathbf{x})L^k_{Mj}(\mathbf{x})\,. \tag{5.5}$$

Next, one can separate the wave-modes for a heterogeneous model as a weighted sum of the wave-modes obtained at the reference models. From equation 3.7, an accurate P-mode

separation in the space domain is formulated as:

$$qP = \nabla_a \cdot \mathbf{W} = L_{Px}[W_x] + L_{Py}[W_y] + L_{Pz}[W_z]\,. \tag{5.6}$$

Generally, for P, SV, or SH mode, this equation can be written as

$$M(\mathbf{x}) = \sum_{j=1}^{3} L_{Mj}(\mathbf{x})[W_j(\mathbf{x})]\,, \tag{5.7}$$

where j denotes a Cartesian component in 3D. Insertion of Equation 5.5 into equation 5.7 yields

$$M(\mathbf{x}) = \sum_{j=1}^{3} \left(\sum_{k} w^k(\mathbf{x}) L^k_{Mj}(\mathbf{x}) \right) [W_j(\mathbf{x})]\,. \tag{5.8}$$

Rearranging this equation, we obtain

$$M(\mathbf{x}) = \sum_{k} w^k(\mathbf{x}) \left\{ \sum_{j=1}^{3} L^k_{Mj}(\mathbf{x})\,[W_j(\mathbf{x})] \right\}, \tag{5.9}$$

The term in the curly brackets is a separated mode using reference model $\mathbf{m}^k$ in equation 5.7. Therefore, we have the interpolated wave modes as

$$M(\mathbf{x}) = \sum_{k} w^k(\mathbf{x}) M^k(\mathbf{x})\,. \tag{5.10}$$

Here, we see that the weights used to interpolate among the separated wave-modes M^k (in equation 5.10) are exactly the same as the weights used to interpolate among the polarization vectors U^k(in equation 5.4) or space-domain filters L^k(in equation 5.5). Therefore, one simply needs to compute the weights based on the heterogeneous multi-dimensional model, and then use these weights to obtain the interpolated wave modes.

The separation problem now becomes a question of how to find the interpolation weights for the chosen reference models. There are two types of methods one can use:

1. Determine the form of the function one wants to interpolate (the polarization vectors, in this case), use a few references to define the function (model), and then calculate the weights for the reference models based on the function. I call this process the

"analytic" method.

2. Regardless of the form of the function, find the interpolation weights for the reference models using numerical interpolation methods, e.g. inverse-distance weight interpolation, natural neighbor interpolation, etc. For symmetry, I refer to this process as "numerical" method.

In the following, I show the implementation of both methods and compare their performance.

5.4 Analytic interpolation method

This section describes the dependence of the polarization vectors on model parameters. From the approximate function form of the vectors, one can find the interpolation weights for the references at an arbitrary model.

In an anisotropic medium, the P-, SV-, and SH-modes are polarized orthogonal to each other for a fixed wave vector $\mathbf{k}$, as depicted by Figure 4.6. The P- and SV-modes are polarized in the symmetry-axis plane, and the SH-mode is polarized in the isotropy plane. The P-mode polarization vector $\mathbf{P}$ deviates from the wave vector $\mathbf{k}$ by an angle Δ. From the cartoon, one can see that the easiest to separate is the SH-mode because it is always polarized in the isotropy plane, and this fact is not influenced by the strength of anisotropy. In equation 4.13, we have

$$\begin{aligned} U_{SHx} &= k_z n_y - k_y n_z \,, \\ U_{SHy} &= k_x n_z - k_z n_x \,, \\ U_{SHz} &= k_y n_x - k_x n_y \,. \end{aligned} \tag{5.11}$$

These equations show that the SH-mode polarization does not depend on anisotropy and that the mode can be interpolated between separated SH modes that are obtained using different $\mathbf{n}$. Since only two variables (two $\mathbf{n}$ components) exist in each polarization vector

component, only two references are needed for interpolation of all $\mathbf{U}_{SH}$ components:

$$U_{SHj}(\mathbf{n}) = \sum_{k=1}^{2} w^k U_{SHj}(\mathbf{n}^k)\,. \tag{5.12}$$

For a heterogeneous TTI model, the SH-mode can be obtained by

$$SH(\mathbf{x}) = \sum_{k=1}^{2} w^k(\mathbf{x}) SH^k(\mathbf{x})\,, \tag{5.13}$$

where $SH^k = \mathcal{F}^{-1}\left\{\sum_{j=1}^{3} i\widetilde{W}_j^k U_{SHj}^k\right\}$.

For VTI media, the P-wave polarization angle can be approximately represented by the expression (Tsvankin, 2005)

$$\nu_P = \theta + B\left[\delta + 2\left(\epsilon - \delta\right)\sin^2\theta\right]\sin 2\theta\,, \tag{5.14}$$

with

$$B = \frac{1}{2\left(1 - V_{S0}^2/V_{P0}^2\right)}.$$

Here, V_{P0} and V_{S0} are P- and S-wave velocities along the symmetry axis; and the angle θ is the angle between the phase vector $\mathbf{k}$ and the symmetry axis $\mathbf{n}$ (Figure 4.6). This expression is an approximation for weakly anisotropic media and indicates that the anisotropic polarization vector ($\mathbf{U}$) deviates from the isotropic polarization vector ($\mathbf{k}$) by a small angle Δ:

$$\nu_P = \theta + \Delta\left(\theta, R, \epsilon, \delta\right)\,. \tag{5.15}$$

For a 3D TTI medium, whose symmetry-axis tilt and azimuth angles are nonzero, the orientation of the P polarization vector also depends on these two angles. Assuming a constant V_{P0}/V_{S0} ratio and a small angle Δ, we get

$$\begin{aligned} U_{Mj} &= U_{Mj}^0 + \Delta U_{Mj} \\ &\approx U_{Mj}^0 + (a\,\epsilon + b\,\delta)\sum_{i\le j}\sum_{j=1}^{3} d_{ij} n_i n_j\,, \end{aligned} \tag{5.16}$$

where a, b, d_{ij} are functions of θ (refer to Appendix B for derivation). Here, M stands for P

or SV mode, and $n_i (i = 1, 2, 3)$ is a component of the symmetry axis $\mathbf{n}$.

There are 12 coefficients in Equation 5.16, and therefore at least 12 references are needed to determine ΔU^k_{Mj}, and thus following equation 5.10, I obtain the interpolated separation

$$M(\mathbf{x}) = \sum_{k=0}^{12} w^k(\mathbf{x}) M^k(\mathbf{x}) , \tag{5.17}$$

with $\sum_{k=0}^{12} w^k(\mathbf{x}) = 1$, M^0 being the separation obtained with isotropy model parameters, and M^k (k=1 to 12) being the separation with anisotropy reference model $\mathbf{m}^k = \{\epsilon^k, \delta^k, \nu^k, \alpha^k\}$ (Refer to Appendix B for details). For a model with either the tilt angle ν or the azimuth α being constant, the required minimum number of references is fewer. Here, a minimum number of 12 anisotropy references are necessary to determine ΔU_{MJ}. Of course, if one uses more references, he can always use the neighboring 12 references for the interpolation. In this chapter, in order to reduce the total separation cost, I limit the the number of anisotropy references to 12.

In summary, the method separates the Thomsen parameters (ϵ and δ) from the symmetry-axis-related parameters (n_x, n_y, n_z or ν and α). This procedure cascades and lowers the dimension for interpolation, and thus the interpolation becomes possible for high dimension (see Appendix B). The benefit of using this analytic method is that the choice of reference models is not critical because one can use any set of reference models to fit the function, as long as the weights for the reference models can be computed (The weights cannot be computed if the interpolation problem degenerates. For example, if three nodal points are co-linear for 2D linear interpolation, then the weights cannot be computed). The shortcoming is that the polarization vector function I use is an approximation, and thus the polarization vectors obtained at the non-nodal models are inaccurate.

5.5 Numerical interpolation method

The above section discusses the possibility of simplifying the dependence of the polarization vectors on various model parameters and using the model to calculate the interpo-

lation weights.

Alternatively, one can find the interpolation weights using known numerical interpolation methods. In this section, I test two types of interpolation methods: inverse-distance weighting (IDW) and natural neighbor interpolation. I choose these two methods because they are applicable for a limited number of irregularly scattered data points. Other interpolation methods usually require gridded data points and the number of data points grows rapidly with the increased dimension of the model space. For example, if one is satisfied with linear interpolation in 4D, then he has to use at least $2^4 = 16$ data points, since two points make a line in each dimension. If one wants to use polynomial or spline interpolation with degree higher than one, then at least $3^4 = 81$ data points have to be used in 4D.

Even though the model space shown in equation 5.1 is seven-dimensional, I show in the previous section that the γ parameter does not influence the mode polarization (even for the SH mode; see equation 5.11) and I simplify the problem by assuming that the model has a constant V_{P0}/V_{S0} ratio (both for wavefield reconstruction and wave-mode separation).

5.5.1 Inverse distance weighting (IDW) interpolation

Inverse distance weighting is suitable for multivariate interpolation. The method assigns values to non-nodal points by using values from the usually scattered set of nodal points (Shepard, 1968). The value at a given model $\mathbf{m}$ is interpolated from N known reference models $\mathbf{m}^k$, k=1...N:

$$U_{Mj} = \sum_{k=1}^{N} \frac{w^k}{\sum_{k=1}^{N} w^k} U_{Mj}^k \,, \tag{5.18}$$

where the weight

$$w^k = \frac{1}{\|\mathbf{m} - \mathbf{m}^k\|} \tag{5.19}$$

is inversely proportional to the distance of the model $\mathbf{m}$ to the known reference model $\mathbf{m}^k$. The normalization in the weights assures that the weights vary between 0 and 1 and the sum of all weights is 1. The advantage of using IDW interpolation is that it is simple to

implement and extends straightforwardly to high dimensions. Therefore, it is applicable to both 2D and 3D TTI wave-mode separation. A potential drawback is that the weights calculated using IDW might be not accurate enough for just a few scattered points in a large model space.

5.5.2 Natural neighbor interpolation

Natural neighbor interpolation is a method of spatial interpolation developed by Sibson (1981). The method is based on Voronoi tessellation of a discrete set of spatial points, and it provides a smooth approximation to the underlying "true" function.

The basic interpolation equation is

$$U_{Mj} = \sum_{k=1}^{N} w^k U_{Mj}^k , \tag{5.20}$$

where the weights are computed differently from the IDW interpolation and the subset of points used for interpolation can also be different. A schematic example of 2D natural neighbor interpolation is given in Figure 5.1. The dots surround by the shaded circles are the nodal points and the dot within the shaded polygon is a point that needs to be interpolated from the nodal points. The 2D space is divided up by the Thiessen polygons which are constructed from the Delauney triangulation of a scattered point set. The Delauney criterion ensures that no vertex lies within the interior of any of the circumcircles of the triangles in the triangulation network. The centroids of the circumcircles of the Delauney triangles are connected to make the Thiessen polygons. Each polygon encloses the area that is closer to the enclosed scatter point than any other scatter point. If a point needs to be interpolated, then this point changes the tesselation of the 2D space in the neighborhood of this point, shown by the shaded polygon in Figure 5.1. The weights for all nodal points are computed as the ratio of the area shared by the polygon defined by center point and the area of the polygon defined by each point before this point was added. Apparently, the weights computed using natural neighbor interpolation are different from the weights

computed using inverse-distance weighting, which assigns a weight of approximately $\frac{1}{7}$ to each nodal point because the point for interpolation is about the same distance to all seven nodal points.

I use natural neighbor interpolation both in 2D and 3D. For higher dimensions, the computation of the weights gets more complicated, as it is difficult to visualize high-dimensional tesselation and the question remains whether the 2D and 3D interpolation algorithm extends straightforwardly to high dimensions. The high-dimensional natural neighbor interpolation is outside the scope of this chapter. So far, I have only used natural neighbor interpolation for 2D TTI models where the model space is three dimensional: $\mathbf{m} = \{\epsilon, \delta, \nu\}$.

5.5.3 Reference model selection

In contrast to the analytic method, in numerical interpolation, the choice of reference models is critical. Since the model space is at least four-dimensional for 3D TTI models, it is difficult to visualize the model space. Therefore, I use a method for high-dimensional reference picking extended from its 1D equivalent. As depicted in Figure 5.2, a model parameter of the medium has a distribution shown by the curve. The horizontal axis is a model parameter (for instance, the P wave velocity v) of the medium, and the vertical axis is the population density of this parameter. The parameter spreads over the range $[a, b]$, the population density ranges from 0 to 1, and the area under the curve is 1. For this 1D problem, I first choose a threshold of occurrence frequency and assume that only velocities with higher occurrence frequency than this threshold are candidates for reference models. Then, I choose the reference models represented by the two peaks of the curve, which have the highest occurrence frequency over the entire model space. This crude method for picking reference velocities in 1D assumes that along the curve there is only one peak in a neighborhood. Otherwise many close references will be picked, which is wasteful for the following processing. Similarly, in high dimensions, I first compute the population density

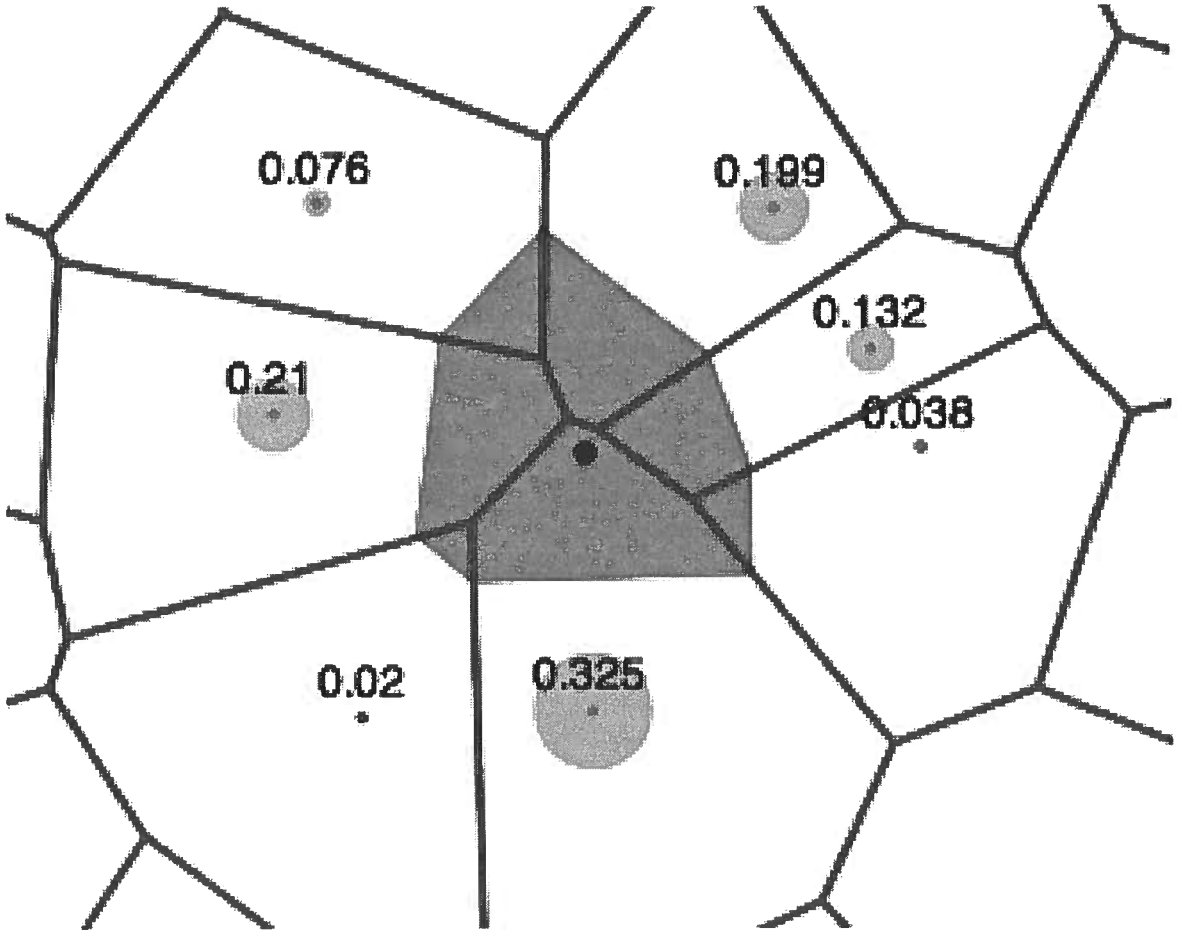

Figure 5.1. Description of natural neighbour interpolation in 2D, taken from the wikipedia website *http* : *//en.wikipedia.org/wiki/Natural_neighbor*. The area of the circles in each polygon represents the interpolation weights w^k, whose value is computed as the ratio of the overlapping shaded area and that of the the neighbor polygon.

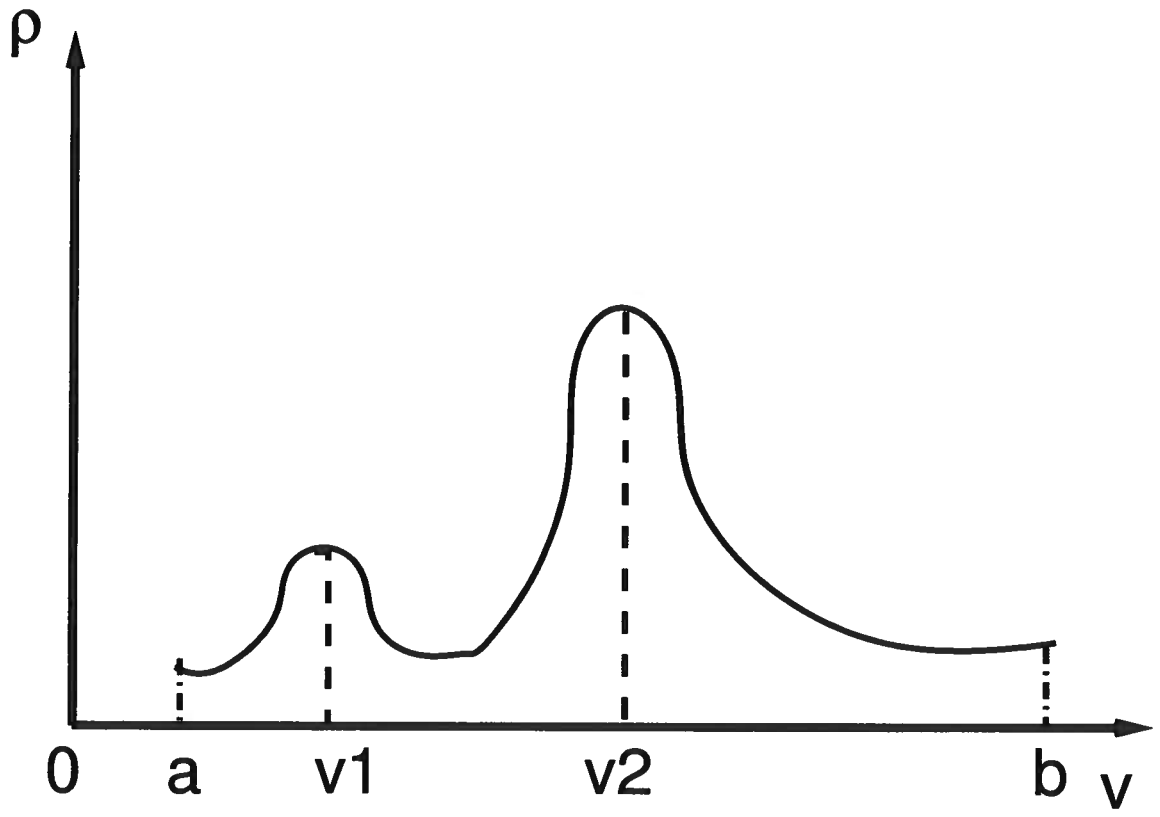

Figure 5.2. Cartoon showing the occurrence frequency of a model parameter. The parameter (P wave velocity, for example) spreads over the range $[a, b]$, and the area under the curve is 1. Velocity v_1 and v_2 are picked as references because of their high occurrence frequency.

of all model parameters, then I choose a threshold and find the local maximums as the reference models.

5.6 Examples

I illustrate the method presented in this chapter with 2D and 3D examples. The 2D example is an elastic version of Marmousi II. The 3D examples include a 3D fold model and a 3D version of the elastic Marmousi II.

5.6.1 2D Marmousi model

The first example uses a 2D Marmousi model to test the feasibility of the mixed-domain separation. Figures 5.3(a)–(d) show model parameters V_{P0}, ϵ, δ, and tilt angle ν, respectively. Figure 5.4 shows the variation of the parameters ϵ, δ, and tilt angle ν in the model space. A visual examination reveals that there are three clouds in the model space, and the reference selection algorithm based on population density chooses 15 references out of the three clouds (of course, the number of picked references changes with different choice of threshold). These 15 references are used for the numerical interpolation. Figure 5.5(a) is a snapshot of the elastic wavefields in the z and x direction. Figures 5.5(b), (c), and (d) show the wave-mode separation using the analytic procedure, IDW, and natural neighbor interpolation, respectively. A comparison of the separation results indicates that all the methods can separate P and S modes. Among them, the analytic method obtains the cleanest P separation at the top of the model. IDW and natural neighbor interpolation achieves similarly good separation results, while exhibiting some visible residual at the top of the model in the P panel, for example at $x = 11.5$ km and $z = 1.0$ km. This artifact suggests that the selected references do not represent the model parameters in that region and that a better reference selection algorithm might be necessary.

5.6.2 3D fold model

The first 3D wave-mode separation example uses a fold model with spatially varying ϵ and δ. The model has a constant V_{P0}/V_{P0} ratio equal to two and $\gamma = 0.0$. The symmetry axis is perpendicular to the layering throughout the model. Figure 5.6 shows the spatially varying ϵ, δ, tilt ν, and azimuth α. Figure 5.7(a) is a snapshot of the elastic wavefields. Figures 5.7(b) and (c) show the separation with the analytic method and IDW interpolation, respectively. A comparison shows that the analytic method obtains a better separation result for all three modes. This result suggests that more references are probably needed for the IDW interpolation.

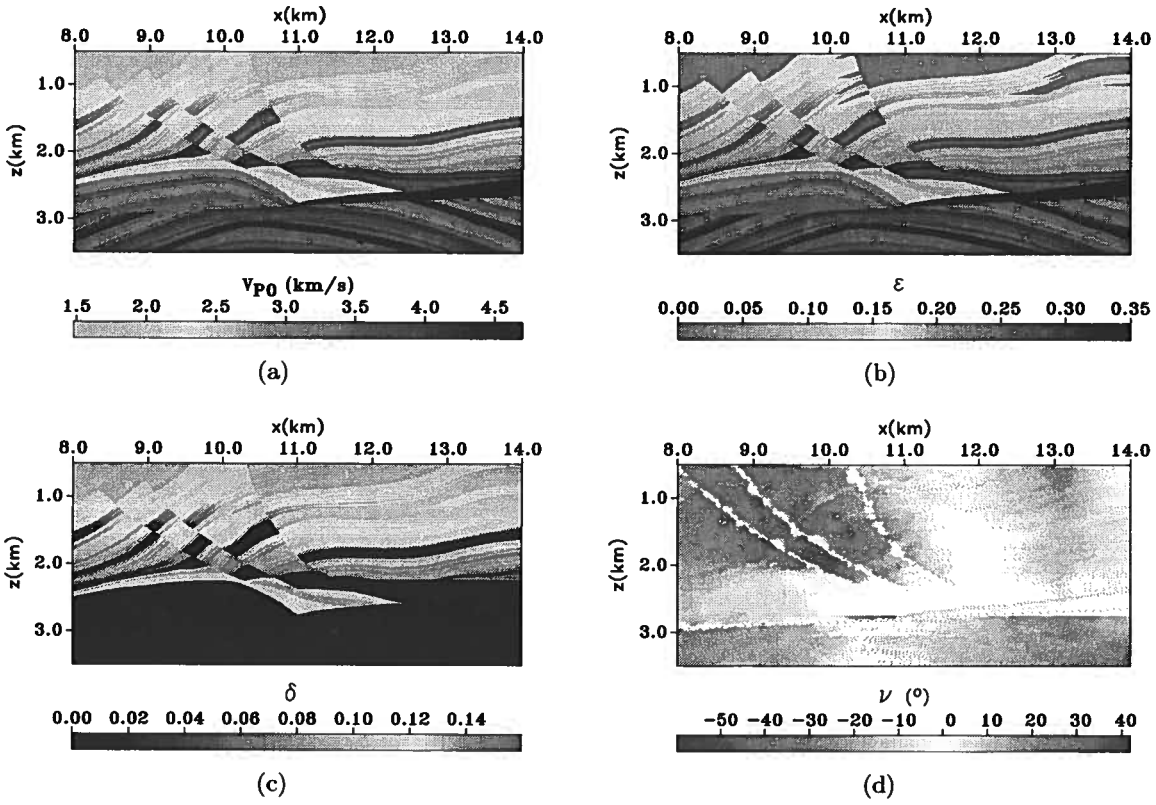

Figure 5.3. Model parameters of a 2D elastic Marmousi II model showing varying (a) V_{P0}, (b) ϵ, (c) δ, and (d) tilt angle ν.

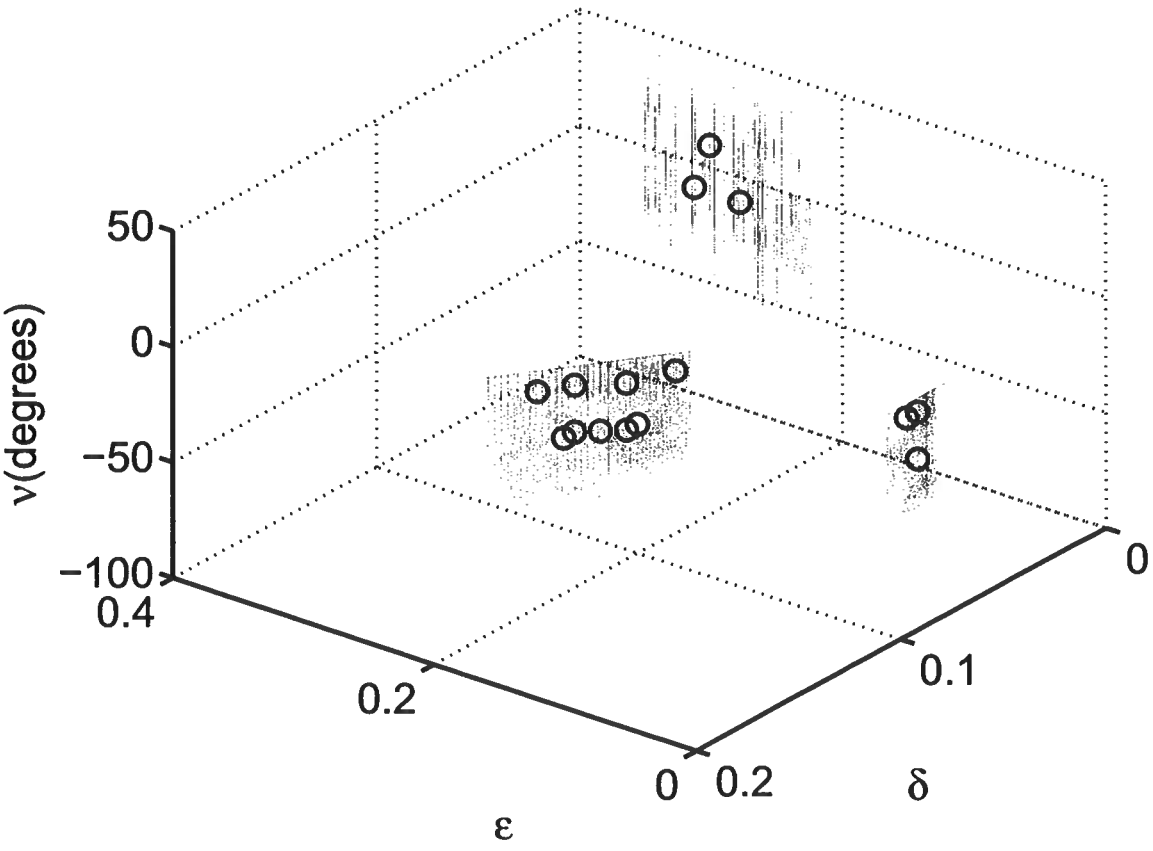

Figure 5.4. Model space showing the variation of the parameters ϵ, δ, and tilt angle ν for the model shown in Figure 5.3. Each dot represents the occurrence of one combination of (ϵ, δ, ν) in the physical model. The dots form three clouds in this space. The circles are the reference models. The reference models are selected based on a criterion depicted in Figure 5.2.

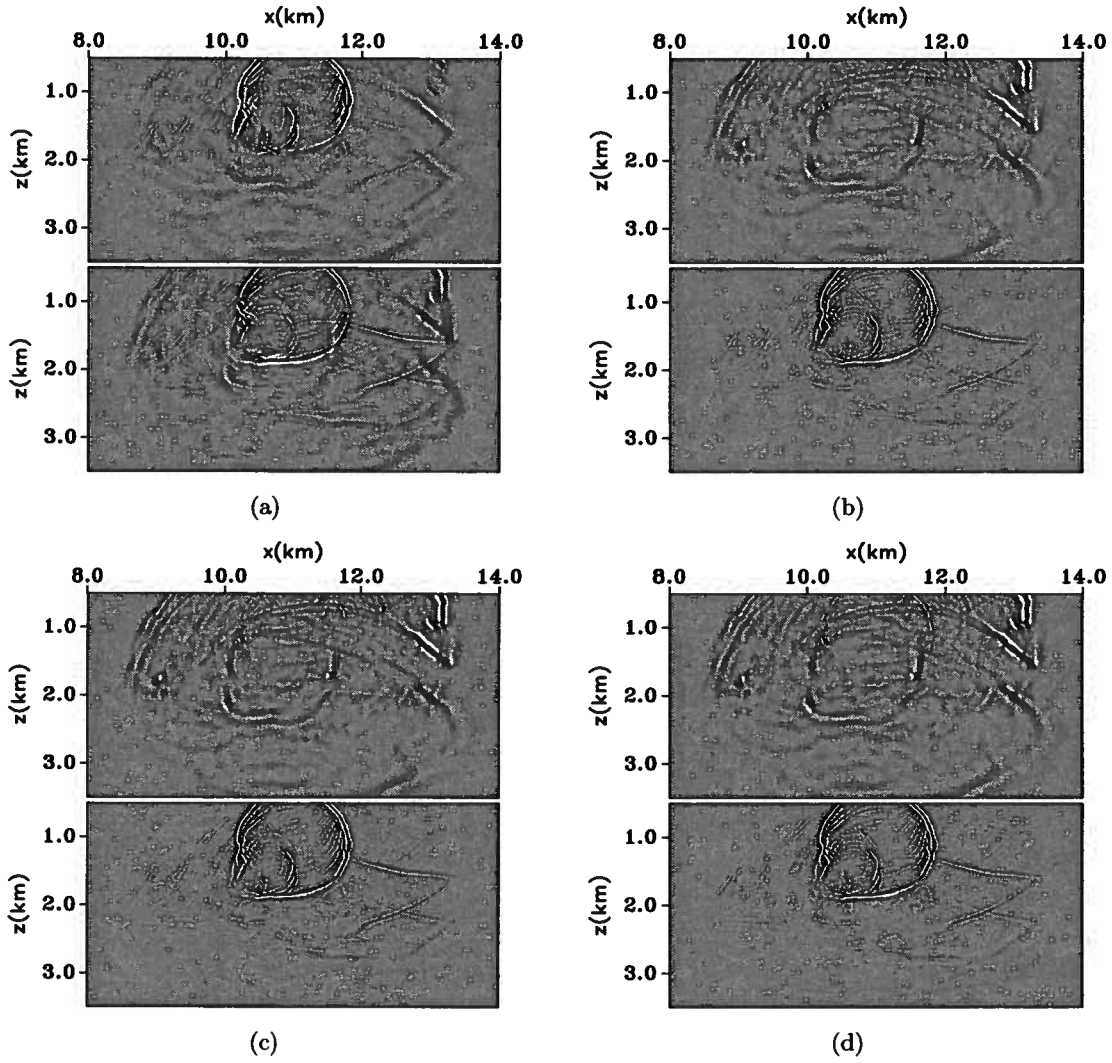

Figure 5.5. (a) A snapshot of the elastic wavefields in vertical and horizontal directions for the model shown in Figure 5.3; trial separation of P- and S-mode using (b) the analytic method, (c) natural neighbor interpolation, and (d) inverse distance weighting interpolation.

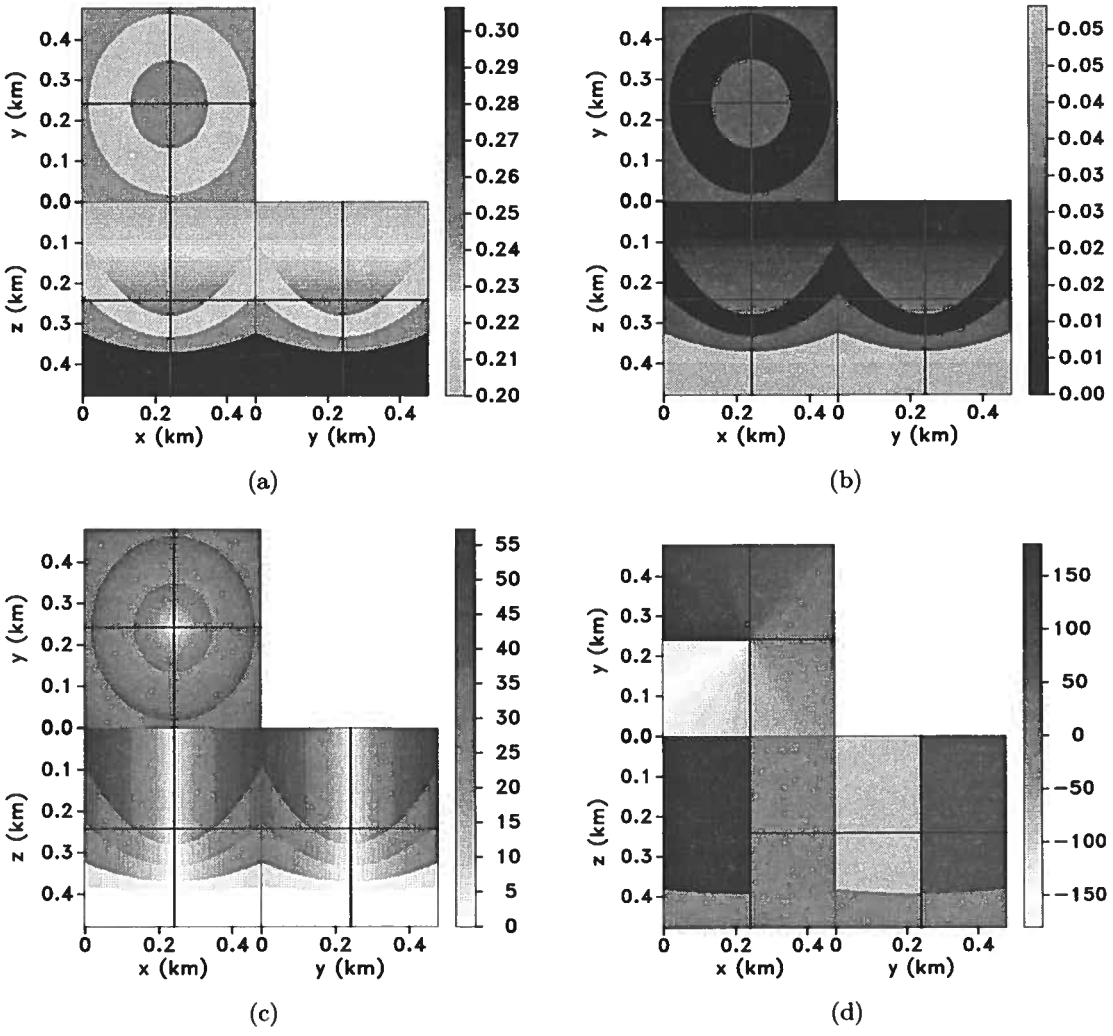

Figure 5.6. 3D TTI fold with model parameters (a) ϵ, (b) δ, (c) tilt angle ν, and (d) azimuth angle α.

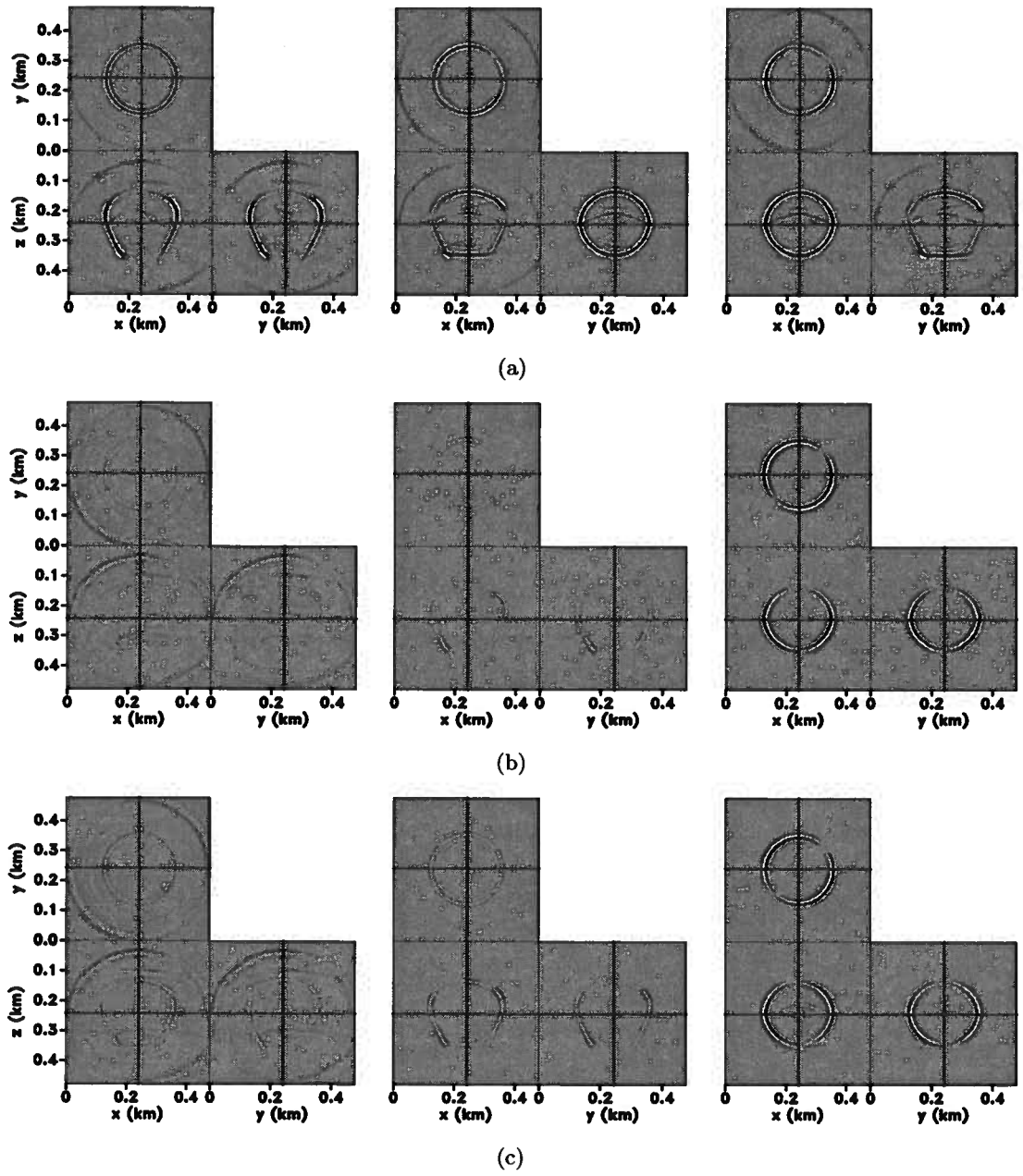

Figure 5.7. (a) A snapshot of the elastic wavefields in the z (left), x (middle), and y (right) directions for the model shown in Figure 5.6. Separated P (left), SV (middle), and SH (right) modes using (b) the analytic methods and (c) inverse-distance weighting interpolation.

5.6.3 3D Marmousi model

The last example is a 3D version of the elastic Marmousi model. The first vertical slices of V_{P0}, V_{S0}, and density are taken from the original 2D model. In the y direction, the vertical slice is shifted constantly to make the next vertical slice. This ensures that the medium has a constant azimuth angle (26°) of anisotropy symmetry axis. Thomsen parameters are derived from the velocity and density model with the relationship of $\epsilon = 0.5\rho/max(\rho)$ and $\delta = 0.25V_{P0}/max(V_{P0})$. Figures 5.8(a)–(d) show V_{P0}, ϵ, δ, and tilt angle ν of the 3D model, respectively. Figure 5.10(a) shows a snapshot of the elastic wavefields. Figures 5.10(b) and (c) show separation using analytic and IDW methods, respectively. Both methods obtain good separation results. The successfully separated modes obtained with IDW interpolation suggest that the selected models represent the entire model space well.

5.7 Discussion

As was demonstrated by the synthetic examples, the separation in the space domain by non-stationary filtering is accurate but computationally expensive; meanwhile, the separation in the mixed domain is less accurate but much cheaper. The cost of separation in the x domain is proportional to the model size times the size of the separators, which becomes prohibitive in 3D. In comparison, the cost of separation in the mixed domain is just proportional to the number of used references, which includes wavefield projection and inverse Fourier transforms of the wavefields.

In the analytic procedure, the interpolation error comes from the approximate representation of the dependence of the polarization angles on ϵ, δ, tilt ν, and azimuth α (equation 5.16). Strictly speaking, the anisotropic polarization vector is only approximately represented by equation 5.16 in 3D. However, the synthetic examples show that mode separation is effective in the mixed domain with the analytic procedure, which suggests that for weak anisotropy, the polarization vector function I used does not deviate much from the true vector directions.

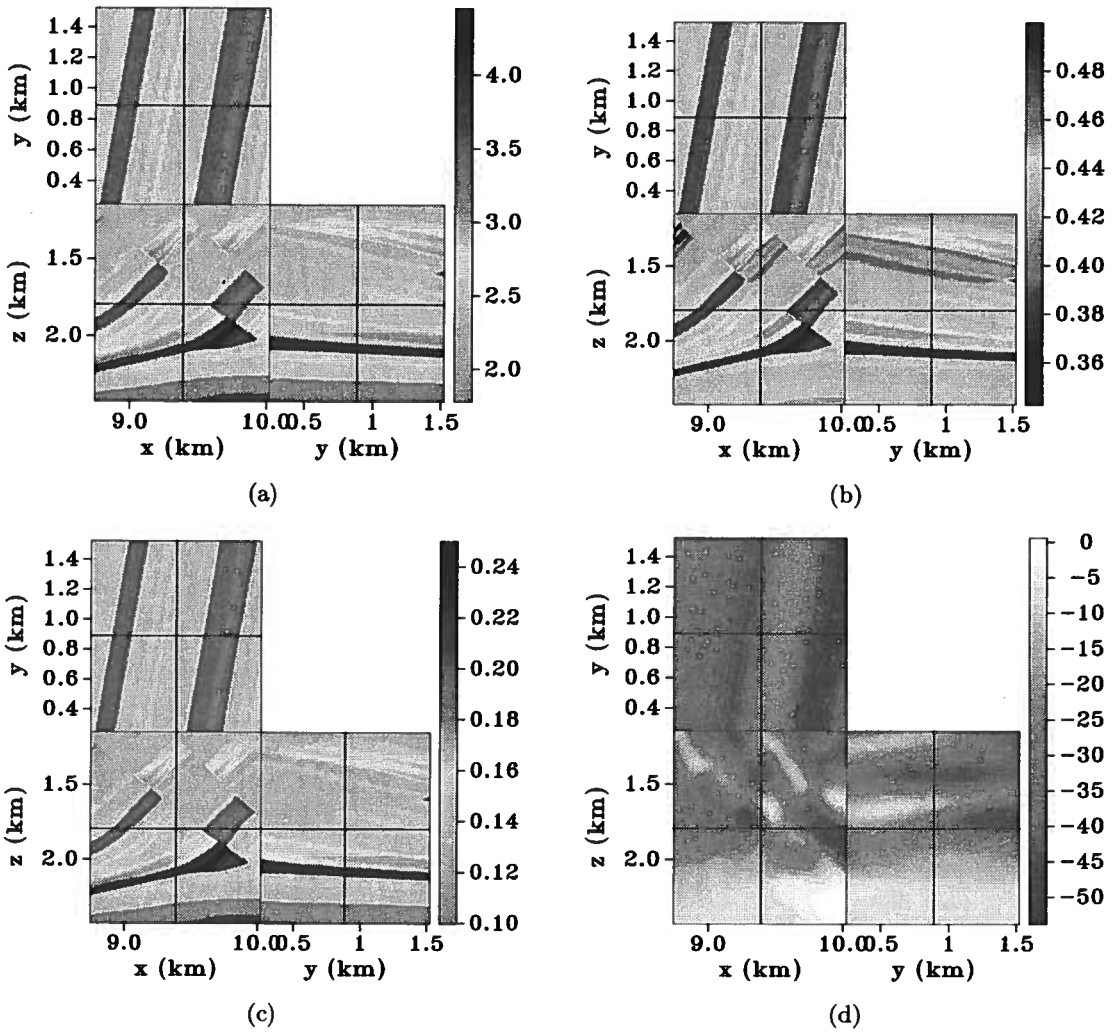

Figure 5.8. 3D Marmousi model with model parameters (a) V_{P0}, (b) ϵ, (c) δ, (d) tilt angle ν.

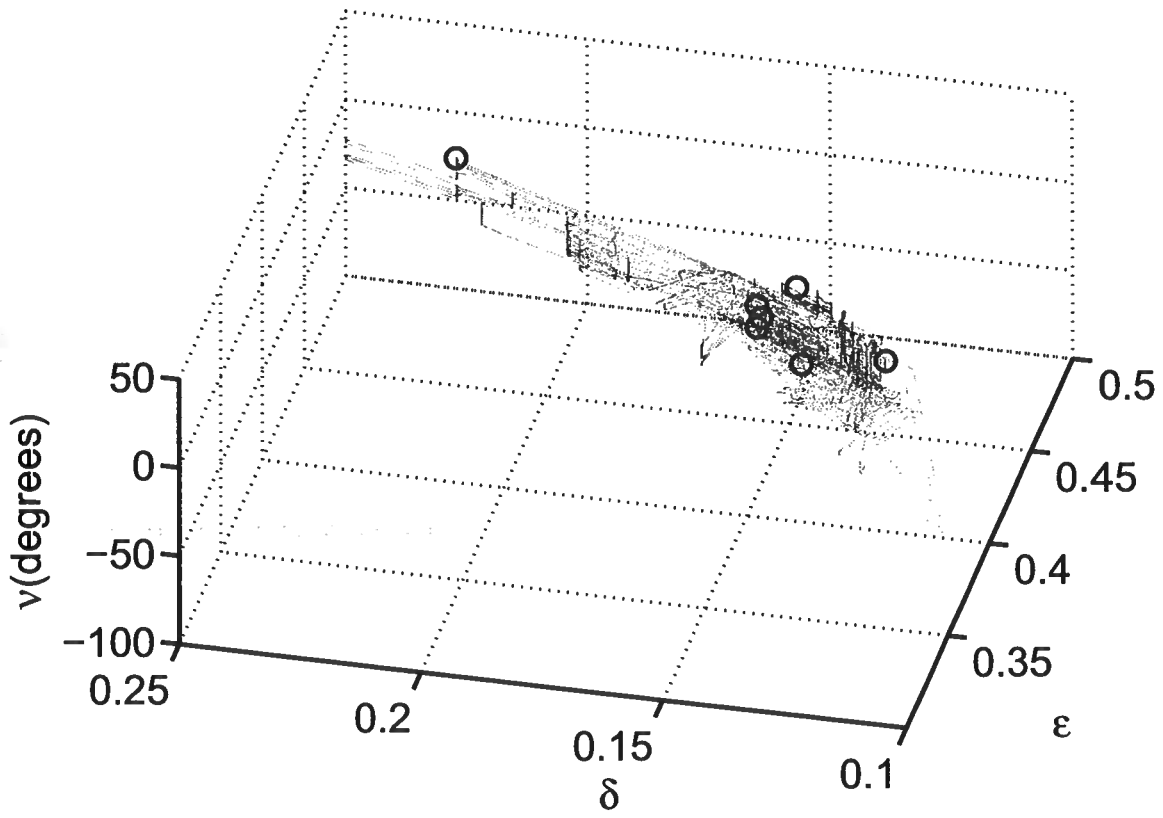

Figure 5.9. Model space showing the variation of the parameters ϵ, δ, and tilt angle ν for the model shown in Figure 5.8. Each dot represents the occurrence of one combination of (ϵ, δ, ν) in the physical model. The dots are widely spread in this space. The circles are the reference models. The reference models are selected based on a criterion depicted in Figure 5.2.

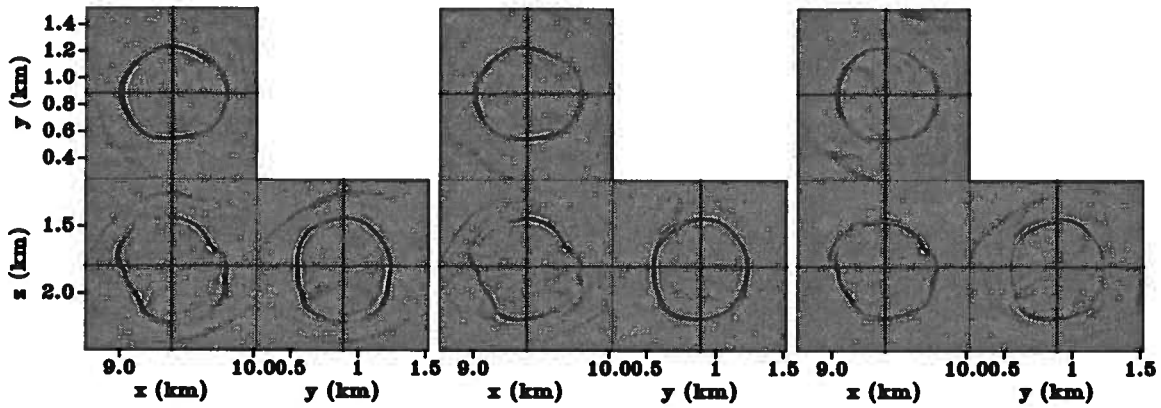

(a)

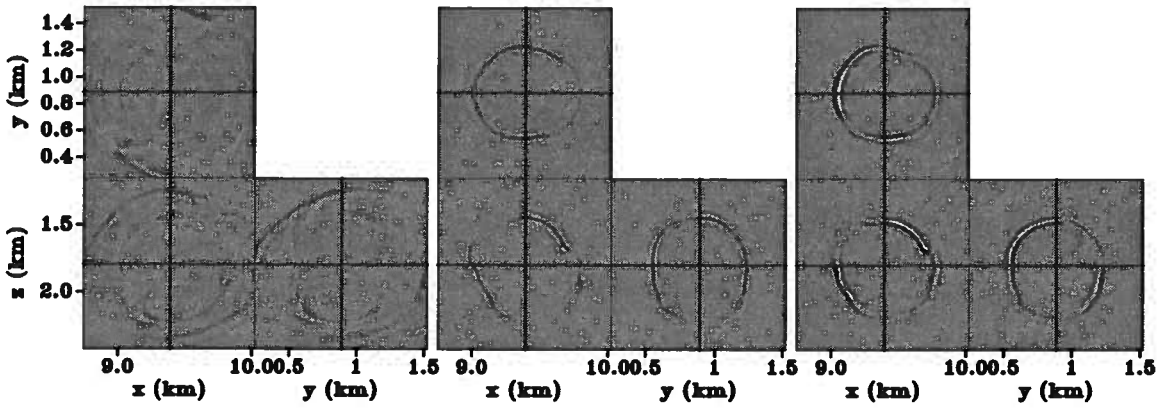

(b)

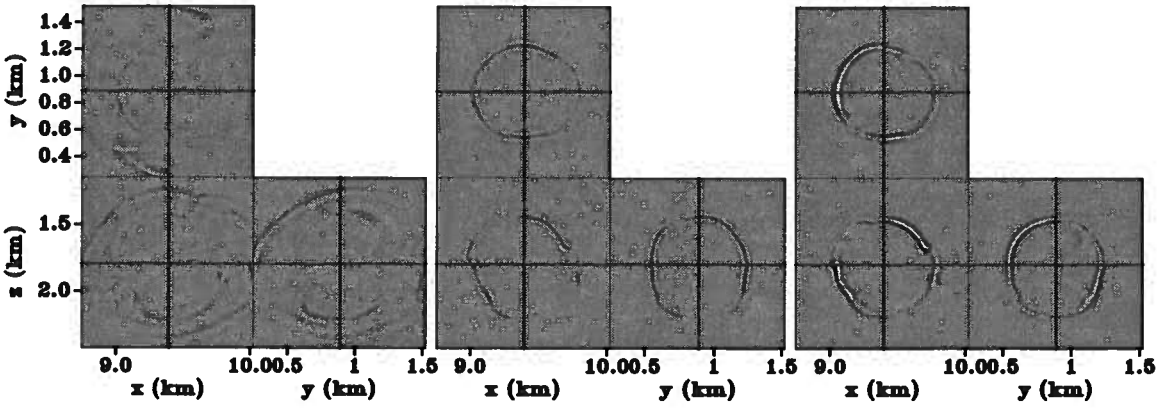

(c)

Figure 5.10. (a) A snapshot of the elastic wavefields in the z (left), x (middle), and y (right) directions for the model shown in Figure 5.8. (b) Separated P (left), SV (middle), and SH (right) modes using (b) the analytic method and (c) inverse-distance weighting interpolation.

In the numerical interpolation procedure, in order to decrease the dimensionality for interpolation, I assume that some model parameters are inter-related. For example, I draw upon the fact that the Thomsen parameter γ does not play a role in the polarization of wave modes. I also learn from equation 5.14 that it is the ratio of V_{P0} and V_{S0} that affects the polarization vectors and that they do not affect the function independently. These observations help one to decrease the dimensionality of the interpolation problem. For the numerical approach, the separation accuracy increases with the number of reference models one uses. However, to limit the cost of separation, one should try to use fewer reference models; and therefore, the separation is always inaccurate.

The reference model selection is necessary in both approaches. Since I use a function to compute the weights in the analytic procedure, the locations of the reference models are not really important. In comparison, for the numerical approach, the reference models should represent the model space of the medium for the best interpolation results. Therefore, the analytic approach is more deterministic, while the numerical approach is more stochastic. To obtain better separation results with the numerical approach, one needs to determine the reference models that best represent the model space, and the choice of the models is case dependent.

In summary, both analytic and numerical methods are subject to interpolation errors. The numerical interpolation method is easy to understand and particularly easy to implement with inverse-distance weighting interpolation. The analytic method seems to be more accurate for the synthetic examples, but the approximate equation I use as the underlying "true" function also subjects the separation to errors.

5.8 Conclusions

I present a mixed-domain wave-mode separation method applicable to complex media. First, I separate wave modes in the wavenumber domain at different reference values of the anisotropy parameters ϵ, δ, tilt angle ν, and azimuth angle α. This is followed by

interpolation in the space domain. I test two separation schemes. One of them derives a relatively simple function of the polarization vectors; I then use this function to compute the interpolation weights. The other is designed to compute the interpolation weights numerically with various interpolation methods. Although the space-domain non-stationary filtering is more accurate for heterogeneous media, it is very expensive. In comparison, the separation in the mixed domain has the advantage of being much more computationally efficient. The mixed-domain separation is especially beneficial for 3D models because the space-domain separation is prohibitively expensive. I test the mixed-domain separation method with several synthetic examples and show that both separation schemes are effective. The analytic method is more accurate but the numerical method is more straightforward to implement.

Chapter 6

Conclusions and future work

6.1 Main results

Multicomponent data have numerous advantages in structural imaging, lithology estimation, anisotropic parameter estimation, and reservoir characterization. In this thesis, I focus on the area of imaging using multicomponent data. The main results of this thesis are addressed in what follows:

- In Chapter 2, I investigate elastic imaging using multicomponent data acquired in isotropic media. If one uses elastic wave equation to reconstruct vector wavefields, he has two options for imaging condition: crosscorrelating the Cartesian components or pure-mode potentials. I compare images created using both imaging conditions and conclude that the potential-based imaging condition creates images that are more interpretable. This imaging condition endows the multicomponent images with clear physical meaning, i.e., the images represent reflection coefficients of different reflection types. Pure-mode potentials can also be used in a generalized imaging condition to generate angle gathers for velocity analysis.

- In Chapter 3, I extend an existing mode-separation method (Dellinger & Etgen, 1990) to heterogeneous media. The existing method for mode-separation in anisotropic media is not suitable for heterogeneous media because heterogeneity in the space domain cannot be represented in the wavenumber domain. The proposed non-stationary filtering in the space domain robustly separates wave modes for models with strong heterogeneity and anisotropy. This extension to heterogeneous models is especially

important because imaging complex geology remains one of the most difficult problems in geophysical exploration.

- In Chapter 4, I extend mode separation to 3D TTI media. As suggested by Dellinger (1991), P-waves can be separated from 3D anisotropic vector wavefields as a straightforward extension of P-wave separation from 2D vector wavefields. In 3D, a difficulty of shear-mode separation originates from the singularity of shear waves. The singularity makes it impossible to find polarization directions for each shear mode in the singular directions, and the shear polarization vectors computed using the plane-wave solution are discontinuous in 3D. I address the shear-wave singularity problem in 3D by taking kinematic approximations. The shear polarization vectors are constructed by utilizing the orthogonality among P, SV, and SH modes for a fixed wave vector. The singularity in the symmetry axis direction is thus ameliorated by taking a smooth variation of the shear polarization vectors, both in amplitudes and directions. A global solution like this enables one to separate shear modes and study shear-wave splitting in 3D. Nowadays, a commonly practiced imaging technique is *acoustic* RTM for TTI media. The mode separation in 3D proposed in this chapter enables *elastic* RTM for TTI media. Although the obtained shear modes do not have accurate amplitudes, the algorithm enables shear-wave splitting analysis in 3D models. Shear-wave splitting has been used extensively for fracture characterization. Conventionally, shear-wave splitting is processed by Alford rotation (Alford, 1986) to the recorded near-offset multicomponent data. In contrast, separating SV and SH modes in the space domain allows one to analyze shear-wave splitting more directly in the subsurface.

- In Chapter 5, I address the problem of computational cost that has been invoked in Chapter 4. A modern geophysical technique not only requires accuracy but also speed. Although the space-domain separation is robust and accurate for 2D models, it is unaffordable for 3D models. To separate wave modes more efficiently in 3D, I

present a mixed-domain approach. The idea is to select references to represent the entire model space and separate the wave modes in the wavenumber domain at the chosen references. The wavefields are interpolated later in the space domain. This mixed-domain separation technique makes separation for heterogeneous 3D models possible. This technique is much faster but has approximately the same accuracy as the space-domain separation. The new approach provides computational speed to wave-mode separation so that it can be applied more efficiently for RTM.

6.2 Suggested future work

In this thesis, I mainly investigate imaging with multicomponent data. I note some of future work directions in the following.

6.2.1 Anisotropic elastic RTM

The mode-separation technique can be applied to reverse time migration and angle decomposition in TTI media, as Helmholtz decomposition is applied in isotropic elastic RTM in Chapter 2. The additional mode-separation step before application of an imaging condition would yield elastic images and angle gathers that are more interpretable.

The elastic imaging technique advocated in this thesis generates four images in 2D and nine images in 3D. In contrast to generating and interpreting only a single image with acoustic migration, how can we use and interpret so many elastic images simultaneously? It is not clear yet. However, I can at least say it takes more effort for the interpretation and this might provide more information about the subsurface.

6.2.2 Anisotropic parameter estimation

In the mode separation, I use the same model parameters to reconstruct the wavefields and separate wave modes, and thus the separation is always successful. However, to reconstruct elastic wavefields in TTI media, one first needs to estimate the model parameters: V_{P0}, V_{S0}, ϵ, δ, γ, tilt angle ν, and azimuth angle α. Anisotropic model building is the most

important and time-consuming procedure in any imaging project, and a high-resolution model is the ultimate goal for reservoir characterization.

Anisotropic model building is a multi-dimensional parameter estimation problem. It is an interesting research question to set up wavefield tomography and/or inversion engines to obtain all these parameters with limited surface (and borehole) data. A possible research direction in the framework of wavefield tomography is to utilize angle gathers for anisotropic parameter estimation. Angle gathers can be used for anisotropic parameter estimation and AVA (amplitude versus angle) analysis.

It has been intensively studied how to use angle gathers for velocity estimation in isotropic media. In order to use the angle gathers for anisotropic parameter estimation, it is imperative to study quantitatively how the anisotropy parameters influence the kinematic behavior of the angle gathers. This kind of study allows for estimation of anisotropy parameters by iteratively updating these parameters to form flat angle gathers.

6.2.3 Model space representation

The synthetic examples in Chapter 5 show that the choice of reference models is important for the mixed-domain separation if numerical interpolation is used. In Chapter 5, I select the reference models for mode separation using a crude method extended from its 1D equivalent. The reference models are simply chosen as the local maxima of parameter occurrence frequency in the model space. Although the chosen combinations of model parameters have the highest occurrence frequency, the question remains whether they are the most suitable for follow-up interpolation and how many reference models are needed to represent the entire model space. An interesting research question also arises: whether a low-dimensional algorithm for sampling has a straightforward extension to higher-dimensions. The study of high-dimensional sampling in the model space has potential benefits in seismic inverse problems, where it is desirable to use as few references as possible to represent the entire model for the purpose of computational and storage-cost saving.

References

Admundsen, L., & Reitan, A. 1995. Decomposition of multicomponent sea-floor data into upgoing and downgoing P and S waves. *Geophysics*, **60**, 560–572.

Admundsen, L., Ikelle, L., & Berg, L. 2001. Multidimensional signature deconvolution and free surface multiple elimination of marine multicomponent ocean-bottom seismic data. *Geophysics*, **66**, 1594–1604.

Aki, K., & Richards, P. 2002. *Quantitative Seismology (second edition)*. University Science Books.

Alford, R. M. 1986. Shear data in the presence of azimuthal anisotropy: Dilley, Texas. *SEG Technical Program Expanded Abstracts*, **5**(1), 476–479.

Alford, R. M., Kelly, K. R., & Boore, D. M. 1974. Accuracy of finite-difference modeling of the acoustic wave equation. *Geophysics*, **39**(6), 834–842.

Alkhalifah, T. 1998. Acoustic approximations for processing in transversely isotropic media. *Geophysics*, **63**(2), 623–631.

Alkhalifah, T. 2000. An acoustic wave equation for anisotropic media. *Geophysics*, **65**(4), 1239–1250.

Alkhalifah, T., & Sava, P. 2010. A transversely isotropic medium with a tilted symmetry axis normal to the reflector. *Geophysics, in press.*

Bale, R. A., Gray, S. H., & Graziella, M. 2007. TTI wave-equation migration. *SEG Technical Program Expanded Abstracts*, **26**(1), 2295–2299.

Baysal, E., Kosloff, D. D., & Sherwood, J. W. C. 1983. Reverse time migration. *Geophysics*, **48**(11), 1514–1524.

Behera, L., & Tsvankin, I. 2009. Migration velocity analysis and imaging for tilted TI media. *Geophysical Prospecting*, **57**, 13–26.

Bolt, B. A., & Smith, W. D. 1976. Finite-element computation of seismic anomalies for bodies of arbitrary shape (short note). *Geophysics*, **41**(01), 145–151.

Bourgeois, A., Bourget, M., Lailly, P., Poulet, M., Ricarte, P., & Versteeg, R. 1991. The Marmousi experience. *Pages 5–16 of:* Versteeg, R., & Grau, G. (eds), *The Marmousi Experience, Proceedings of the 1990 EAEG workshop.* Marmousi, model and data.

Chang, W. F., & McMechan, G. A. 1986. Reverse-time migration of offset vertical seismic profiling data using the excitation-time imaging condition. *Geophysics*, **51**(1), 67–84.

Chang, W. F., & McMechan, G. A. 1994. 3-D elastic prestack, reverse-time depth migration. *Geophysics*, **59**(4), 597–609.

Charles, S., Mitchell, D. R., Holt, R. A., Lin, J., & Mathewson, J. 2008. Data-driven tomographic velocity analysis in tilted transversely isotropic media: A 3D case history from the Canadian Foothills. *Geophysics*, **73**(5), VE261–VE268.

Claerbout, J. F. 1971. Toward a unified theory of reflector mapping. *Geophysics*, **36**(03), 467–481.

Claerbout, J. F. 1985. *Imaging the Earth's Interior*. Blackwell Scientific Publications.

Clayton, R. W. 1981. *Wavefield Inversion Methods for Refraction and Reflection Data*. Ph.D. thesis, Stanford University.

Clayton, R. W., & Brown, D. 1979. The Choice of Variables for Elastic Wave Extrapolation. *SEP-Report*, **20**, 73–96.

Cunha Filho, C. 1992. *Elastic Modeling and Migration in Earth Models*. PhD thesis, Stanford University.

Dablain, M. A. 1986. The application of high-order differencing to the scalar wave equation. *Geophysics*, **51**(01), 54–66.

Dai, N., & Cheadle, S. 1996. Pseudo-spectral migration in the f-x domain. *SEG Technical Program Expanded Abstracts*, **15**(1), 427–430.

Dellinger, J. 1991 (April). *Anisotropic Seismic Wave Propagation*. Ph.D. thesis, Stanford University.

Dellinger, J., & Etgen, J. 1990. Wave-field separation in two-dimensional anisotropic media (short note). *Geophysics*, **55**(07), 914–919.

Etgen, J. T. 1988. Prestacked migration of P- and SV-waves. *SEG Technical Program Expanded Abstracts*, **7**(1), 972–975.

Fletcher, R. P., Du, X., & Fowler, P. J. 2009. Reverse time migration in tilted transversely isotropic (TTI) media. *Geophysics*, **74**(6), WCA179–WCA187.

Fomel, S. 2002. Applications of plane-wave destruction filters. *Geophysics*, **67**(06), 1946–1960.

Fomel, S, & Backus, M. M. 2003. Multicomponent seismic data registration by least squares. *SEG Technical Program Expanded Abstracts*, **22**(1), 781–784.

Fornberg, B., & Ghrist, M. 1999. Spatial finite difference approximations for wave-type equations. *Siam Journal on Numerical Analysis.*

Fowler, P. J., Du, X., & Fletcher, R. P. 2010. Coupled equations for reverse time migration in transversely isotropic media. *Geophysics*, **75**(1), S11–S22.

Gaiser, J. 1996. Multicomponent Vp/Vs correlation analysis. *Geophysics*, **61**, 1137–1149.

Gaiser, J., Moldoveanu, N., Macbeth, C., Michelena, R., & Spitz, S. 2001. Multicomponent technology: the players, problems, applications, and trends: Summary of the workshop sessions. *The Leading Edge*, **20**(9), 974–977.

Gazdag, J., & Sguazzero, P. 1984. Migration of seismic data by phase shift plus interpolation. *Geophysics*, **49**(2), 124–131.

Gazdag, J., & Sguazzero, P. 1985. Migration of seismic data by phase shift plus interpolation. *Pages 323–330 of:* Gardner, G. H. F. (ed), *Migration of seismic data.* Soc. of Expl. Geophys. Reprinted from Geophysics, 49, 124-131.

Godfrey, R. J. 1991. Imaging Canadian foothills data. *Pages 207–209 of: 61st Ann. Internat. Mtg.* Soc. of Expl. Geophys.

Gray, S. H., Etgen, J., Dellinger, J., & Whitmore, D. 2001. Seismic migration problems and solutions. *Geophysics*, **66**(5), 1622–1640.

Hokstad, K. 2000. Multicomponent Kirchhoff migration. *Geophysics*, **65**(3), 861–873.

Hokstad, K., Mittet, R., & Landro, M. 1998. Elastic reverse time migration of marine walkaway vertical seismic profiling data. *Geophysics*, **63**(05), 1685–1695.

Hou, A., & Marfurt, K. 2002. Multicomponent prestack depth migration by scalar wavefield extrapolation. *Geophysics*, **67**, 1886–1894.

Isaac, J. H., & Lawyer, L. C. 1999. Image mispositioning due to dipping TI media: A physical seismic modeling study. *Geophysics*, **64**(4), 1230–1238.

Jones, I. F., Goodwin, M. C., Berranger, I. D., Zhou, H., & Farmer, P. A. 2007. Application of anisotropic 3D reverse time migration to complex North Sea imaging. *SEG Technical Program Expanded Abstracts*, **26**(1), 2140–2144.

Kieslev, A. P., & Tsvankin, Ilya. 1989. A method of comparison of exact and asymptotic wave field computations. *Geophysical Journal International*, **96**, 253–258.

Knapp, S., Payne, N., & Johns, T. 2001. Imaging through gas clouds: A case history from the Gulf of Mexico. *SEG Technical Program Expanded Abstracts*, **20**(1), 776–779.

Kuo, J. T., & Dai, T. F. 1984. Kirchhoff elastic wave migration for the case of noncoincident source and receiver. *Geophysics*, **49**(8), 1223–1238.

Levin, S. A. 1984. Principle of reverse-time migration. *Geophysics*, **49**(5), 581–583.

Li, X. Y. 1998. Fracture detection using P-P and P-S waves in multicomponent sea-floor data. *SEG Technical Program Expanded Abstracts*, **17**(1), 2056–2059.

Martin, G. S., Marfurt, K. J., & Larsen, S. 2002. Marmousi-2: An updated model for the investigation of AVO in structurally complex areas. *SEG Technical Program Expanded Abstracts*, **21**(1), 1979–1982.

McMechan, G. A. 1982. Determination of source parameters by wavefield extrapolation. *Geophysical Journal International*, **71**(3), 613–628.

McMechan, G. A. 1983. Migration by extrapolation of time-dependent boundary values. *Geophysical Prospecting*, **31**(3), 413–420.

Mora, P. 1988. Elastic wave-field inversion of reflection and transmission data. *Geophysics*, **53**(06), 750–759.

Mora, P. R. 1987. Nonlinear two-dimensional elastic inversion of multioffset seismic data. *Geophysics*, **52**(09), 1211–1228.

Nickel, M., & Sonneland, L. 2004. Automated PS to PP event registration and estimation of a high-resolution Vp-Vs ratio volume. *SEG Technical Program Expanded Abstracts*, **23**(1), 869–872.

Paffenholz, Josef, McLain, Bill, Zaske, Joerg, & Keliher, P. Joseph. 2002. Subsalt multiple attenuation and imaging: Observations from the Sigsbee2B synthetic dataset. *SEG Technical Program Expanded Abstracts*, **21**(1), 2122–2125.

Pestana, R. C., da Mota, F. M. Roxo, Ulrych, T. J., Freire, S., & da Silva, F. Barbosa. 1989. Deterministic and stochastic separation of P and SV-waves: A comparison. *SEG Technical Program Expanded Abstracts*, **8**(1), 1308–1311.

Sava, P., & Fomel, S. 2003. Angle-domain common image gathers by wavefield continuation methods. *Geophysics*, **68**(3), 1065–1074.

Sava, P., & Fomel, S. 2005. Wave-equation common-angle gathers for converted waves. *SEG Technical Program Expanded Abstracts*, **24**(1), 947–950.

Sava, P., & Fomel, S. 2006a. Time-shift imaging condition for converted waves. *SEG Technical Program Expanded Abstracts*, **25**(1), 2460–2464.

Sava, P., & Fomel, S. 2006b. Time-shift imaging condition in seismic migration. *Geophysics*, **71**(6), S209–S217.

Sava, P., & Guitton, A. 2005. Multiple attenuation in the image space. *Geophysics*, **70**, V10–V20.

Seriani, G., & Priolo, E. 1991. High-order spectral element method for acoustic wave modeling. *SEG Technical Program Expanded Abstracts*, **10**(1), 1561–1564.

Seriani, G., Priolo, E., Carcione, J., & Padovani, E. 1992. High-order spectral element method for elastic wave modeling. *SEG Technical Program Expanded Abstracts*, **11**(1), 1285–1288.

Shan, G. 2006. Optimized implicit finite-difference migration for VTI media. *SEG Technical Program Expanded Abstracts*, **25**(1), 2367–2371.

Shan, G., & Biondi, B. 2005. 3D wavefield extrapolation in laterally-varying tilted TI media. *SEG Technical Program Expanded Abstracts*, **24**(1), 104–107.

Shepard, D. 1968. A two-dimensional interpolation function for irregularly-spaced data. *Pages 517–524 of: ACM '68: Proceedings of the 1968 23rd ACM national conference.* New York, NY, USA: ACM.

Sibson, R. 1981. *Interpreting Multivariate Data: A brief description of natural neighbor interpolation.* Chichester: John Wiley. Chap. Chapter 2.

Simmons, J., & Backus, M. 2003. An introduction—Multicomponent. *The Leading Edge*, **22**(12), 1227–1262.

Stewart, R. R., Gaiser, J. E., Brown, R. J., & Lawton, D. C. 2003a. Converted-wave seismic exploration: Applications. *Geophysics*, **68**(1), 40–57.

Stewart, R. R., Gaiser, J., Brown, R. J., & Lawton, D. C. 2003b. Converted-wave seismic exploration: Applications. *Geophysics*, **68**(1), 40–57.

Sun, R., McMechan, G. A., Lee, C S, Chow, J, & Chen, C H. 2006. Prestack scalar reverse-time depth migration of 3D elastic seismic data. *Geophysics*, **71**(5), S199–S207.

Thomsen, L. 1986. Weak elastic anisotropy. *Geophysics*, **51**(10), 1954–1966.

Tsvankin, I. 2005. *Seismic signatures and analysis of reflection data in anisotropic media: 2nd edition.* Elsevier Science Publ. Co., Inc.

Ursenbach, C., & Bale, R. 2009. TTI wave-equation migration for Canadian Foothills depth imaging. *The Leading Edge*, **28**(11), 1344–1351.

Vavryčuk, V. 2002. Properties of S waves near a kiss singularity: a comparison of exact and ray solutions. *Geophysical Journal International*, **138**(2), 581–589.

Vestrum, R. W., Lawyer, L. C., & Schmid, R. 1999. Imaging structures below dipping TI media. *Geophysics*, **64**(4), 1239–1246.

Virieux, J. P-SV wave propagation in heterogeneous media: Velocity-stress finite-difference method. *Geophysics*, 889–901.

Virieux, J. 1984. SH-wave propagation in heterogeneous media: Velocity-stress finite-difference method. *Geophysics*, **49**(11), 1933–1942.

Wapenaar, C. P. A., & Haimé, G. C. 1990. Elastic extrapolation of seismic P- and S-waves. *Geophysical Prospecting*, **38**(1), 23–60.

Wapenaar, C. P. A., Kinneging, N. A., & Berkhout, A. J. 1987. Principle of prestack migration based on the full elastic two-way wave equation. *Geophysics*, **52**, 151–173.

Wapenaar, C. P. A., Herrmann, P., Verschuur, D. J., & Berkhout, A. J. 1990. Decomposition of Multicomponent Seismic Data into primary P- and S-Wave Responses. *Geophysical Prospecting*, **38**(6), 633–661.

Whitmore, N. D. 1983. Iterative depth migration by backward time propagation. *SEG Technical Program Expanded Abstracts*, **2**(1), 382–385.

Whitmore, N. D. 1995. *An Imaging Hierarchy for Common-Angle Seismograms.* Ph.D. thesis, The University of Tulsa.

Yan, J., & Sava, P. 2008. Isotropic angle-domain elastic reverse-time migration. *Geophysics*, **73**(6), S229–S239.

Yan, J., & Sava, P. 2009. Elastic wave-mode separation for VTI media. *Geophysics*, **74**(5), WB19–WB32.

Zhang, Q., & McMechan, G. A. 2010. 2D and 3D elastic wavefield vector decomposition in the wavenumber domain for VTI media. *Geophysics*, **75**(3), D13–D26.

Zhe, J., & Greenhalgh, S. A. 1997. Prestack multicomponent migration. *Geophysics*, **62**(02), 598–613.

Zhu, X., Altan, S., & Li, J. 1999. Recent advances in multicomponent processing. *The Leading Edge*, **18**(11), 1283–1288.

Appendix A

Finite difference approximations to different orders of accuracy

This appendix summarizes the wavenumber-domain weighting of the ideal derivative function ik_j, $j = 1,2,3$ for operators of various degrees of accuracy. Starting from the coefficients of a derivative stencil in the space-domain, one can use conventional Z transforms to construct a wavenumber-domain weighting function representing the same order of accuracy. I apply the same weighting functions to both the isotropic and anisotropic projections of the polarization vectors in order to obtain space-domain derivative operators of similar order of accuracy.

For the case of 2^{nd} order centered derivatives, the stencil has the following Z-transform representation:

$$D_2(Z) = -\frac{1}{2}\left(Z^1 - Z^{-1}\right) . \tag{A.1}$$

Transforming from the Z to the wavenumber domain, we obtain

$$D_2(k) = -\frac{1}{2}\left(e^{ik} - e^{-ik}\right) , \tag{A.2}$$

which enables one to define the second order weight

$$W_2(k) = \frac{\sin(k)}{k} . \tag{A.3}$$

Similarly, one can construct weights for 4^{th}, 6^{th} and 8^{th} order operators from Z-

transform representations:

$$D_4(Z) = -\frac{2}{3}\left(Z^1 - Z^{-1}\right) + \frac{1}{12}\left(Z^2 - Z^{-2}\right), \tag{A.4}$$

$$D_6(Z) = -\frac{3}{4}\left(Z^1 - Z^{-1}\right) + \frac{3}{20}\left(Z^2 - Z^{-2}\right) - \frac{1}{60}\left(Z^3 - Z^{-3}\right), \tag{A.5}$$

$$D_8(Z) = -\frac{8}{5}\left(Z^1 - Z^{-1}\right) + \frac{1}{5}\left(Z^2 - Z^{-2}\right) - \frac{4}{105}\left(Z^3 - Z^{-3}\right) + \frac{1}{140}\left(Z^4 - Z^{-4}\right), \tag{A.6}$$

which transform to the wavenumber-domain weights:

$$D_4(k) = -\frac{2}{3}\left(e^{ik} - e^{-ik}\right) + \frac{1}{12}\left(e^{2ik} - e^{-2ik}\right), \tag{A.7}$$

$$D_6(k) = -\frac{3}{4}\left(e^{ik} - e^{-ik}\right) + \frac{3}{20}\left(e^{2ik} - e^{-2ik}\right) - \frac{1}{60}\left(e^{3ik} - e^{-3ik}\right), \tag{A.8}$$

$$D_8(k) = -\frac{4}{5}\left(e^{ik} - e^{-ik}\right) + \frac{1}{5}\left(e^{2ik} - e^{-2ik}\right) - \frac{4}{105}\left(e^{3ik} - e^{-3ik}\right) + \frac{1}{280}\left(e^{4ik} - e^{-4ik}\right), \tag{A.9}$$

which lead to the following weighting functions:

$$W_4(k) = -\frac{4\sin(k)}{3k} + \frac{\sin(2k)}{6k}, \tag{A.10}$$

$$W_6(k) = -\frac{3\sin(k)}{2k} + \frac{3\sin(2k)}{10k} - \frac{\sin(3k)}{30k}, \tag{A.11}$$

$$W_8(k) = -\frac{8\sin(k)}{5k} + \frac{2\sin(2k)}{5k} - \frac{8\sin(3k)}{105k} + \frac{\sin(4k)}{140k}. \tag{A.12}$$

These derivatives are shown in Figures 3.2(a) and (b) in the space and wavenumber domains, respectively. Comparing these weights and their corresponding frequency responses, we see that one needs to use higher order difference operators to have better approximations to high frequencies. For comparison, the weight used in Dellinger & Etgen (1990) is $\frac{1}{2}\left[1 + cos(k)\right]$. The cosine taper attenuates middle frequencies compared to high order finite difference operators.

Appendix B

Linear Approximation for polarization vectors

B.1 The polarization vectors for 2D TTI media

For VTI media, the P-wave polarization angle can be approximately represented by the expression (Tsvankin, 2005)

$$\nu_P = \theta + B\left[\delta + 2\left(\epsilon - \delta\right)\sin^2\theta\right]\sin 2\theta\,, \tag{B.1}$$

with

$$B = \frac{1}{2\left(1 - V_{S0}^2/V_{P0}^2\right)}.$$

Here, V_{P0} and V_{S0} are the P- and S-wave velocities along the symmetry axis; and the angle θ is the angle between the phase vector $\mathbf{k}$ and the symmetry axis $\mathbf{n}$ (Figure 4.6).

For a TTI medium with a nonzero tilt angle, equation B.1 takes the form

$$\nu_P = \theta + B\left[\delta + 2\left(\epsilon - \delta\right)\sin^2(\theta - \nu)\right]\sin 2(\theta - \nu)\,. \tag{B.2}$$

Here, the angle θ is the angle between the vector $\mathbf{k}$ and the vertical axis k_z. The angle $\theta - \nu$ gives the polar angle for the TTI medium. The anisotropic P-wave polarization vector ($\mathbf{U}$) deviates from the isotropic polarization vector ($\mathbf{k}$) by an angle Δ:

$$\nu_P = \theta + \Delta\left(\theta, B, \epsilon, \delta, \nu\right)\,. \tag{B.3}$$

The magnitude of the angle Δ is small. This is verified by Figures B.1(a) and (b), and Figure B.2(a), which show that with moderate anisotropy ($\epsilon = 0.4$, $\delta = 0.2$ and V_{P0}/V_{S0}=2), and various tilt angles ν, the angle Δ is no more than 0.25 radians($\ll 1$). The magnitude

of the angle, of course, also depends on the V_{P0}/V_{S0} ratio, which usually ranges from 1.4 to 7. This gives a range $[0.5, 1]$ to the variable B. Even for the largest V_{P0}/V_{S0} ratio 7, the angle Δ does not exceed 0.4 radians. Because the V_{P0}/V_{S0} ratio can be grouped with the anisotropy parameters to make new variables $B\epsilon$ and $B\delta$, the entire interpolation can be implemented in the same way. For simplicity, I now assume that the V_{P0}/V_{S0} ratio is a constant.

Assuming small Δ, one can expand the P-wave polarization components into

$$U_{Px} = \sin(\theta+\Delta) = \sin\theta\cos\Delta + \cos\theta\sin\Delta \approx \sin\theta + \cos\theta\Delta = k_x + k_z\Delta\,, \quad \text{(B.4)}$$

$$U_{Pz} = \cos(\theta+\Delta) = \cos\theta\cos\Delta - \sin\theta\sin\Delta \approx \cos\theta + \sin\theta\Delta = k_z + k_x\Delta\,. \quad \text{(B.5)}$$

Figures B.1(a) and (b) and equation 5.14 show that the deviation angle is approximately linearly dependent on the anisotropy parameters ϵ and δ.

Figure B.2(a) shows that Δ does not linearly depend on ν for fix ϵ and δ; however, one can try to fit the curves of Δ at different ν with a scaled function of $\sin 2(\theta-\nu)$, shown by Figure B.2(b). The fit is not exact due to the second term in the square bracket in equation B.2, which depends on θ. Thus, Δ is only approximately proportional to

$$\sin 2(\theta-\nu) = \sin(2\theta)\cos(2\nu) - \cos(2\theta)\sin(2\nu). \quad \text{(B.6)}$$

We can now write the second terms of equations B.4 and B.5 for 2D TI media in the form

$$\Delta U_{Mj} \approx (a\,\epsilon + b\,\delta)(c\cos 2\nu + d\sin 2\nu)\,, \quad \text{(B.7)}$$

where a, b, c, and d are functions of k_x and k_z (or functions of θ). Equation B.7 indicates that one needs a minimum number of four points, $\mathbf{m}^1 = \{\epsilon^1, \delta^1, \nu^1\}$, $\mathbf{m}^2 = \{\epsilon^1, \delta^1, \nu^2\}$, $\mathbf{m}^3 = \{\epsilon^2, \delta^2, \nu^1\}$, and $\mathbf{m}^4 = \{\epsilon^2, \delta^2, \nu^2\}$, to determine the model given in equation B.7. The way to interpolate (extrapolate) between the four reference models is similar to bilinear interpolation shown in Figure B.3 and Appendix B.3. At any model parameter

$\mathbf{m} = \{\epsilon, \delta, \nu\}$, we have the polarization vector

$$U_{Mj} = U^0_{Mj} + \Delta U_{Mj} = U^0_{Mj} + \sum_{k=1}^{4} w^k \Delta U^k_{Mj} \,. \tag{B.8}$$

For P mode, $M = P$, $U_{Px} = k_x$, and $U_{Pz} = k_z$. For SV mode, $M = SV$, $U_{SVx} = -k_z$, and $U_{SVz} = k_x$. The P or SV wave is obtained with

$$\begin{aligned}
M &= \mathcal{F}^{-1}\left\{\sum_{j=1}^{2} iU_{Mj}\widetilde{W}_j\right\} \\
&= \mathcal{F}^{-1}\left\{\sum_{j=1}^{2}\left[i\widetilde{W}_j(U^0_{Mj} + \sum_{k=1}^{4} w^k \Delta^k)\right]\right\} \\
&= M^0 + \sum_{j=1}^{2}\sum_{k=1}^{4} w^k \mathcal{F}^{-1}\left\{i\widetilde{W}_j(U^k_{Mj} - U^0_{Mj})\right\} \\
&= M^0 + \sum_{k=1}^{4}(w^k M^k - w^k M^0) \\
&= (1 - \sum_{k=1}^{4} w^k)M^0 + \sum_{k=1}^{4}(w^k M^k) \\
&= \sum_{k=0}^{4} w^k M^k \,,
\end{aligned} \tag{B.9}$$

where $M^0 = \mathcal{F}^{-1}\left\{\sum_{j=1}^{2} i\widetilde{W}_j U^0_{Mj}\right\}$ is the separation with $\epsilon = 0$ and $\delta = 0$ and $M^k = \mathcal{F}^{-1}\left\{\sum_{j=1}^{2} i\widetilde{W}_j U^k_{Mj}\right\}$ is the separation with reference model at reference model $\mathbf{m}^k = \{\epsilon^k, \delta^k, \nu^k\}$. The formulas to calculate the weights w^k are given in Appendix B.3.

B.2 The polarization vectors for 3D TTI media

The P-mode polarization vector $\mathbf{U}_P = \{U_{Px}, U_{Py}, U_{Pz}\}$ is always polarized in symmetry-axis planes, the planes formed by symmetry axis vector $\mathbf{n}$ and wave vector $\mathbf{k}$ at different directions. The P-mode polarization $\mathbf{U}_P$ can be obtained by rotating from $\mathbf{k}$ by a small deviation angle Δ (which is defined earlier for 2D) in the symmetry-axis plane (Figure 4.6):

$$\mathbf{U}_P = \mathbf{R}(\mathbf{u})\,\mathbf{k}\,, \tag{B.10}$$

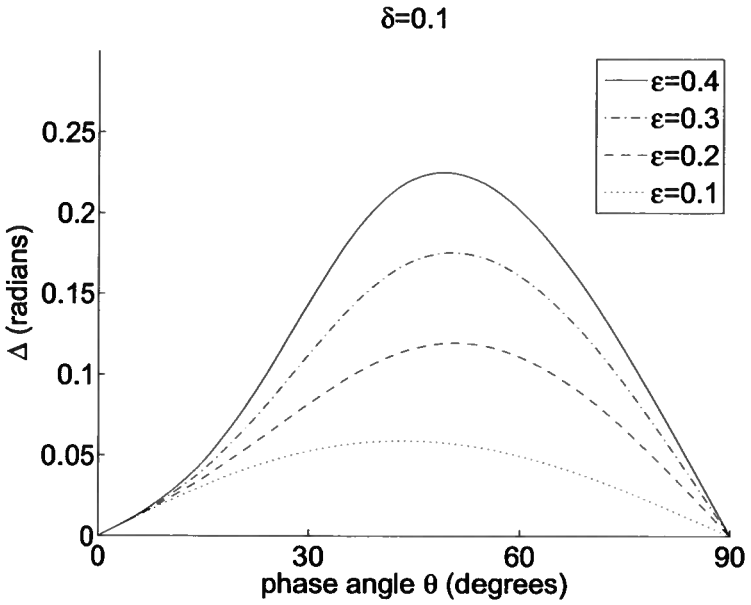

(a)

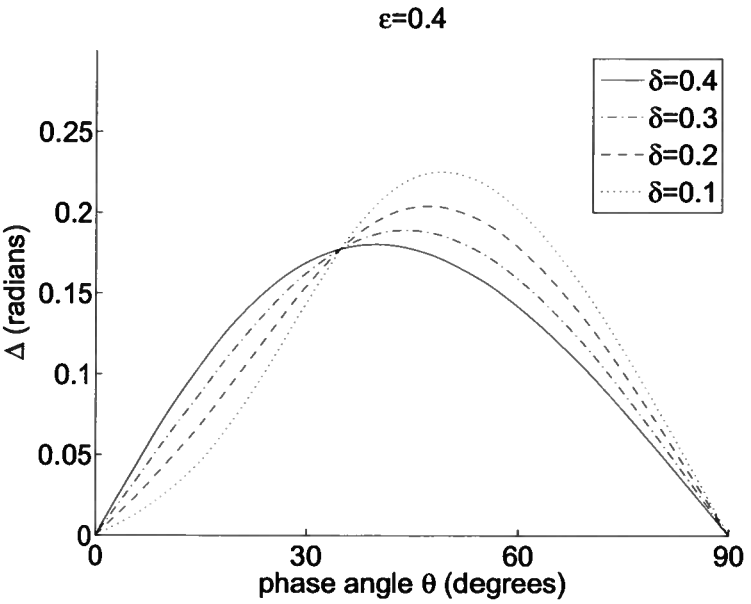

(b)

Figure B.1. Deviation angle of P-mode polarization from the wave vector **k** for VTI media with different combinations of ϵ and δ. (a) The deviation angle for parameter ϵ ranging from 0.1 to 0.4 and a fixed $\epsilon = 0.1$; (b) The deviation angle for parameter δ ranging from 0.1 to 0.4 and a fixed $\epsilon = 0.4$. The deviation angles are approximately linearly dependent on ϵ and δ, which is consistent with the linearized equation B.1.

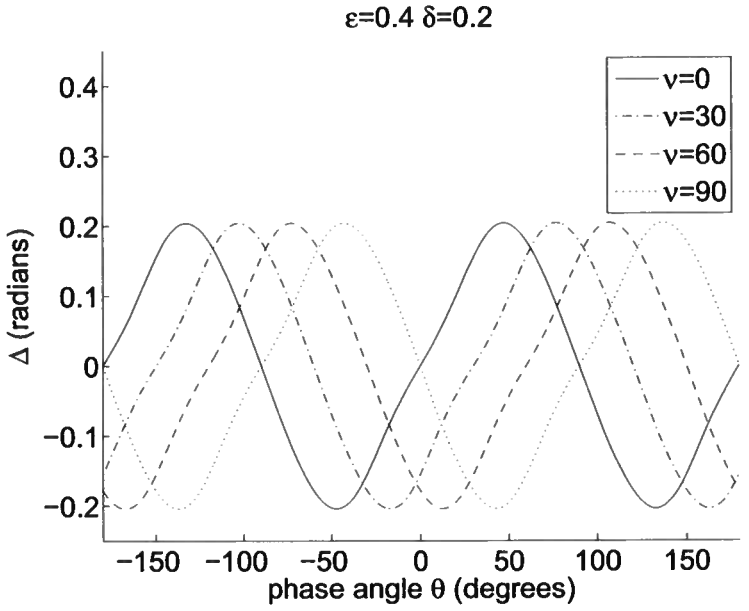

(a)

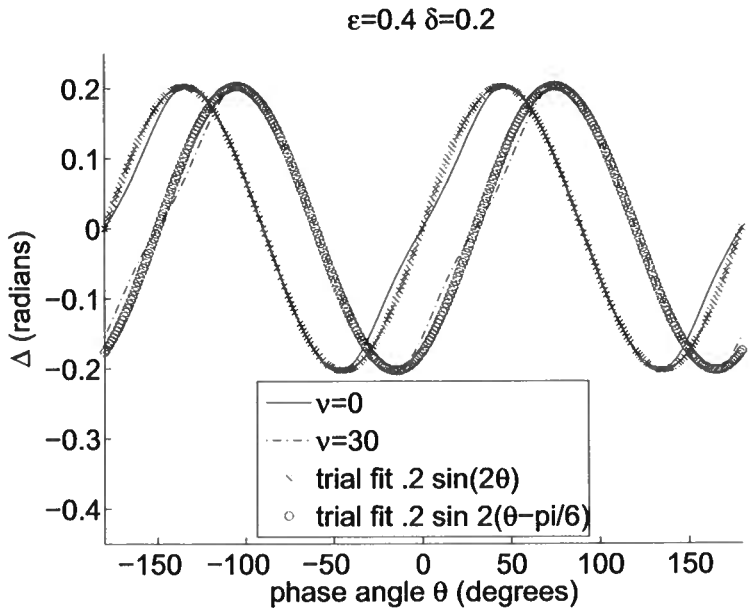

(b)

Figure B.2. Deviation angle of P-mode polarization from the wave vector $\mathbf{k}$ for TTI media ($\epsilon = 0.4$, $\delta = 0.2$) with varying tilt angle ν . (a) is the deviation angles for tilt angles 0, 30°, 60°, and 90°. The curves for these angles are a simple shift from each other by the angle ν. (b) The deviation angle Δ can be approximated fit by a scaled function of $\sin 2(\theta - \nu)$.

where $\mathbf{R}(\mathbf{u})$ is the rotation matrix with a rotation axis $\mathbf{u} = \frac{\mathbf{n}\times\mathbf{k}}{|\mathbf{n}\times\mathbf{k}|}$ and rotation angle Δ. Letting $\mathbf{u} = \frac{\mathbf{n}\times\mathbf{k}}{|\mathbf{n}\times\mathbf{k}|} = \{x, y, z\}$ and assuming small Δ, one can express the rotation matrix as

$$\begin{aligned}
\mathbf{R} &= \begin{pmatrix} 0 & -z & y \\ z & 0 & -x \\ -y & x & 0 \end{pmatrix} \sin\Delta + (\mathbf{I} - \mathbf{u}\mathbf{u}^T)\cos\Delta + \mathbf{u}\mathbf{u}^T \\
&\approx \begin{pmatrix} 0 & -z & y \\ z & 0 & -x \\ -y & x & 0 \end{pmatrix} \Delta + \mathbf{I} \\
&= \begin{pmatrix} 1 & -z\Delta & y\Delta \\ z\Delta & 1 & -x\Delta \\ -y\Delta & x\Delta & 1 \end{pmatrix}, \qquad \text{(B.11)}
\end{aligned}$$

with $\cos\Delta \approx 1$ and $\sin\Delta \approx \Delta$. Substitution of equation B.11 into equation B.10 yields

$$\begin{aligned}
U_{Px} &= k_x - zk_y\Delta + yk_z\Delta\,, \\
U_{Py} &= k_y - xk_z\Delta + zk_x\Delta\,, \\
U_{Pz} &= k_z - yk_x\Delta + xk_y\Delta\,. \qquad \text{(B.12)}
\end{aligned}$$

I use U_{Px} as an example to expand equation B.12:

$$\begin{aligned}
U_{Px} &= k_x - zk_y\Delta + yk_z\Delta \\
&= k_x - \frac{(\mathbf{n}\times\mathbf{k})_z}{|\mathbf{n}\times\mathbf{k}|}k_y\Delta + \frac{(\mathbf{n}\times\mathbf{k})_y}{|\mathbf{n}\times\mathbf{k}|}k_z\Delta\,. \qquad \text{(B.13)}
\end{aligned}$$

The angle Δ has the same physical meaning as in 2D—it is an angle in the symmetry-axis planes between the vector $\mathbf{n}$ and $\mathbf{k}$. Therefore, as in 2D, the angle Δ is linearly dependent on ϵ and δ.

From the analogy to 2D (equation B.6), one knows that the angle Δ is approximately

proportional to

$$\sin(2\theta_{\mathbf{n},\mathbf{k}}) = 2\sin(\theta_{\mathbf{n},\mathbf{k}})\cos(\theta_{\mathbf{n},\mathbf{k}}) = 2(\mathbf{n}\cdot\mathbf{k})\,|\mathbf{n}\times\mathbf{k}|\,, \tag{B.14}$$

with $\theta_{\mathbf{n},\mathbf{k}}$ being the angle between vectors $\mathbf{n}$ and $\mathbf{k}$. Here, the wave vector $\mathbf{k} = \{k_x, k_y, k_z\}$ and the symmetry axis vector $\mathbf{n} = \{n_x, n_y, n_z\} = \{\sin\nu\cos\alpha, \sin\nu\sin\alpha, \cos\nu\}$. One can then express the sum of the second and third terms in equation B.12 as

$$\begin{aligned}
\Delta U_{Px} &= -\frac{(\mathbf{n}\times\mathbf{k})_z}{|\mathbf{n}\times\mathbf{k}|}k_y\Delta + \frac{(\mathbf{n}\times\mathbf{k})_y}{|\mathbf{n}\times\mathbf{k}|}k_z\Delta \\
&= \frac{\Delta}{|\mathbf{n}\times\mathbf{k}|}\left[-(\mathbf{n}\times\mathbf{k})_z k_y + (\mathbf{n}\times\mathbf{k})_y k_z\right] \\
&= (a\epsilon + b\delta)(\mathbf{n}\cdot\mathbf{k})\left[-(\mathbf{n}\times\mathbf{k})_z k_y + (\mathbf{n}\times\mathbf{k})_y k_z\right] \\
&= (a\epsilon + b\delta)(n_x k_x + n_y k_y + n_z k_z)\left[-(k_y n_x - k_x n_y)k_y + (k_x n_z - k_z n_x)k_z\right] \\
&= (a\epsilon + b\delta)\sum_{i\le j}\sum_{j=1}^{3} d_{ij} n_i n_j\,,
\end{aligned} \tag{B.15}$$

where a, b, d_{ij} are functions of the vector $\mathbf{k}$. All components of $\Delta\mathbf{U}_P$ can be represented in this form. One can verify that this equation reduces to the 2D equation B.7 by setting $k_y = 0$ and $\alpha = 0$. With this equation, one can interpolate the P mode in 3D similar to 2D as shown in Figure B.3.

The SV-mode can be interpolated in a way similar to the P-mode. Assuming that $\mathbf{U}^{\mathbf{0}}_{\mathbf{SV}}(\mathbf{k})$ is the SV-mode polarization vector of an isotropic medium for a given wave vector $\mathbf{k}$, the TI polarization vector for SV-mode $\mathbf{U_{SV}}$ is a rotation from $\mathbf{U}^{\mathbf{0}}_{\mathbf{SV}}$, represented by a rotation matrix $\mathbf{R_{SV}}$. Fortunately, because P- and SV-modes are mutually orthogonal and both are polarized in the same symmetry-axis plane for a given wave vector $\mathbf{k}$, the rotation matrix from $\mathbf{k}$ to $\mathbf{U_P}$ and from $\mathbf{U}^{\mathbf{0}}_{\mathbf{SV}}(\mathbf{k})$ to $\mathbf{U_{SV}}$ are the same. By analogy, we have

$$\mathbf{U}_{SV} = \mathbf{R}(\mathbf{u})\,\mathbf{U}^{\mathbf{0}}_{\mathbf{SV}}(\mathbf{k})\,, \tag{B.16}$$

and therefore

$$\begin{aligned} U_{SVx} &= U^0_{SVx} - zk_y\Delta + yk_z\Delta \\ U_{SVy} &= U^0_{SVy} - xk_z\Delta + zk_x\Delta \\ U_{SVz} &= U^0_{SVz} - yk_x\Delta + xk_y\Delta\,. \end{aligned} \tag{B.17}$$

Therefore, the SV-mode can be obtained by interpolation in the same way as for the P-mode.

From equation B.15, one needs two references for ϵ and δ and six references for tilt axis $\mathbf{n} = \{n_x, n_y, n_z\}$, and therefore one needs a total number of 12 anisotropy references:

$$\begin{aligned} M &= (1 - \sum_{k=1}^{12} w^k)M^0 + \sum_{k=1}^{12}(w^k M^k) \\ &= \sum_{k=0}^{12} w^k M^k\,, \end{aligned} \tag{B.18}$$

where $M^0 = \mathcal{F}^{-1}\left\{\sum_{j=1}^{2} i\widetilde{W}_j U^0_{Mj}\right\}$ is the separation with $\epsilon = 0$ and $\delta = 0$ and $M^k = \mathcal{F}^{-1}\left\{\sum_{j=1}^{2} i\widetilde{W}_j U^k_{Mj}\right\}$ is the separation with reference model at reference model $\mathbf{m}^k = \{\epsilon^k, \delta^k, \nu^k, \alpha^k\}$. The formulas to calculate the weights w^k are given in Appendix B.3.

B.3 Cascaded linear interpolation

We consider a function in the form

$$f = \sum_{i=1}^{m} a_i x_i \sum_{j=1}^{n} b_j y_j\,. \tag{B.19}$$

Similar to bi-linear interpolation, we can interpolate to obtain the function value at any point in the panel, first in the direction of x's, then in the direction of y's. This idea is shown in Figure B.3.

For linear interpolation either in the x direction or in the y direction, the problem becomes a question of how to interpolate for a function in the form

$$g = \sum_{i=1}^{m} a_i x_i\,. \tag{B.20}$$

For such a function, one needs at least m known points to interpolate. This gives a system of linear equations in the coefficients a_i:

$$\begin{pmatrix} x_1^1 & x_2^1 & \cdots & a_m^1 \\ x_1^2 & x_2^2 & \cdots & a_m^2 \\ \vdots & \vdots & \ddots & \vdots \\ x_1^m & x_2^m & \cdots & a_m^m \end{pmatrix} \begin{pmatrix} a_1 \\ a_2 \\ \vdots \\ a_m \end{pmatrix} = \begin{pmatrix} g^1 \\ g^2 \\ \vdots \\ g^m \end{pmatrix} . \tag{B.21}$$

Here, the subscripts mean numbering of the variables, while the superscripts mean the numbering of the data points. In a short form, the above equation can be written as

$$Xa = g . \tag{B.22}$$

When the square matrix is not large, meaning the number m is not large, this system for a_i can be solved using Cramer's rule:

$$a_i = \frac{det(X_i)}{det(X)}, i = 1, 2, \cdots, m , \tag{B.23}$$

where X_i is the matrix formed by replacing the i^{th} column of the matrix X by the column g. After the coefficients a_i are determined, we can find the function value g for any combination of $(x_1, x_2, \cdots, x_m)$:

$$g = \sum_{i=1}^{m} a_i x_i = \sum_{i=1}^{m} w^m g^m . \tag{B.24}$$

The original function f can be linear interpolated by cascading two linear interpolations in x's and y's in the following way:

$$f = \sum_{i=1}^{m} \sum_{i=1}^{n} w^{ij} f^{ij} , \tag{B.25}$$

where

$$w^{ij} = w^i w^j . \tag{B.26}$$

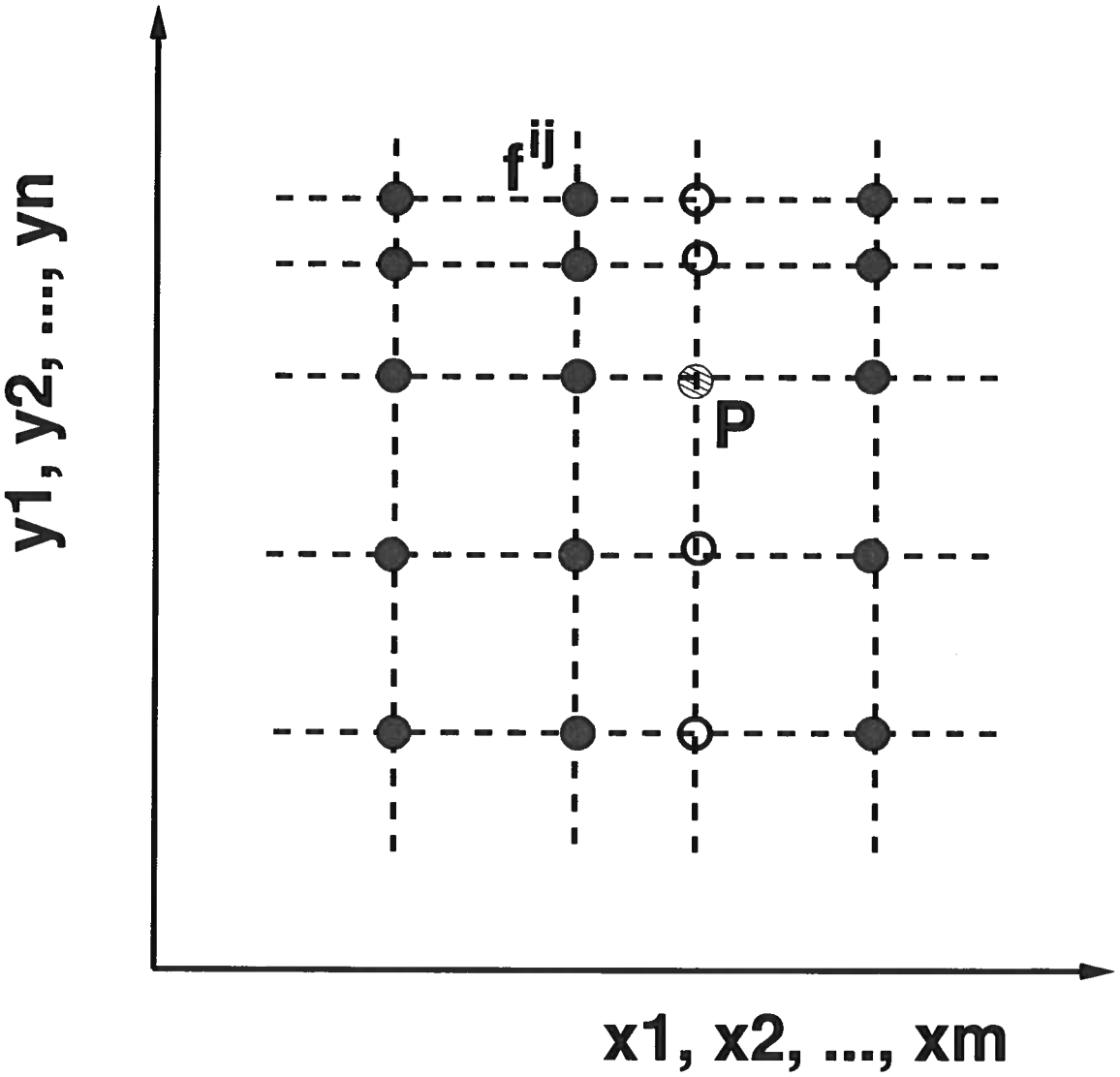

Figure B.3. Function $\sum_{i=1}^{m} a_i x_i \sum_{j=1}^{n} b_j y_j$ can be interpolated by cascaded linear interpolation in the directions of x's and y's. The solid circles, f^{ij}, represent nodal points in the interpolation. The open circles represent intermediate interpolated points by linear interpolation in the x's direction. The shaded circle P represents an arbitrary point in the panel that obtains its value by linearly interpolation between the open circles.